Studies in Laser Photo-cathode RF Guns

A Dissertation Presented

by

Xiangyun Chang

to

The Graduate School

in Partial fulfillment of the

Requirements

for the Degree of

Doctor of Philosophy

in

Physics

Stony Brook University

December, 2005

Abstract of the Dissertation

Studies in Laser Photo-cathode RF Guns

by

Xiangyun Chang

Doctor of Philosophy

in

Physics

Stony Brook University

2005

The emittance compensation mechanics of a "non-magnetized" (the magnetic field on cathode is zero) beam in a compact RF gun with a solenoid, a drift space and a booster linac system is presented. The chromaticity effect is included. The recipe of designing and optimizing the system is given.

A "magnetized" (the magnetic field on cathode is not zero) beam is used for some particular applications such as electron cooling of the ion beams. The emittance compensation of a magnetized beam is studied.

For the RHIC electron-cooling project, the charge per bunch (20nC) and the magnetization (380mm.mr) are very high. Following the rules of designing and optimizing the system, the beam dynamics of the RHIC e-cooling injector is simulated using PARMELA code. With the requirement of merging the low energy beam with the high energy beam, the transverse emittance ε_M is as small as 35mm.mr, while the longitudinal emittance is as small as 100deg.keV. These results fulfill the RHIC e-cooling requirements

The mechanism, physical properties and the electron beam qualities of the secondary emission enhanced photoinjector (SEEP) are presented. The studies indicate that the SEEP can generate high quality electron beam with many advantages:

1. Reduction of the number of primary electrons by the large SEY, i.e. a very low laser power requirement in the photocathode producing the primaries.
2. Protection of the cathode from possible contamination from the gun, allowing the use of large quantum efficiency but sensitive cathodes.
3. Protection of the gun from possible contamination by the cathode, allowing the use of superconducting gun cavities.
4. Production of high average currents, up to ampere class.
5. Expected long lifetime.

The RF field penetration through a thin metal film is studied and verified experimentally.

We measured the charge carrier (electron or hole) transmission in diamond samples. The experiments of the natural diamond provide a lot of information and most of the data are consistent with theory and previous measurements. With better quality diamond, we expect that the electron transmission through diamond will be appropriate for SEEP

Contents

LIST OF SYMBOLS

α :	Dimensionless amplitude of the accelerating field
b:	Impact parameter
$\beta, \beta_0, \gamma, \gamma_0$:	Relativistic parameters
β_{IP} :	Beta function at the interaction point
B_s :	Solenoid field on cathode
c:	Speed of light
δ :	Momentum spread of the beam (primary electron gain in chapter 6)
δ_{Al} :	Skin depth for aluminum
ζ :	Longitudinal bunch position relative to the bunch center
E_0:	Peak field of the RF field
ε:	Emittance of the bunches
ε_M :	Emittance for a magnetized beam
f_b :	Bunch repetition frequency
$F(v_i, v_e)$:	Cooling force
I_0 :	Alfvén current
k_B :	Boltzmann constant
λ_D:	Debye length
λ_{RF} :	RF wavelength
L_{STP}:	Average stopping distance

K_r:	Effects of an external linear focusing channel
K_s:	Perveance
$m_{i,e}$:	Ion or electron mass
M :	Magnetization of an electron
N_i:	Number of particles in the bunch
NEA:	Negative Electron Affinity
$\nu(z)$:	Generalized beam size
ω_p:	Electron transverse plasma frequency
p_θ:	rms canonical momentum on the cathode
P :	Normalized, relativistic perveance
Q:	Charge of the bunch
r_0:	Beam radius
r_L:	Larmor radius
r_s:	Beam radii on the cathode
R_{CSDA}:	Continuous Slowing Down Approximation parameter
σ:	rms beam size (electrical conductivity in chapter 6)
$\hat{\sigma}$:	Invariant envelope
σ_z:	rms bunch length
σ_W, ν_W:	Beam waist size
T:	Temperature
θ :	Angle in phase space
θ_D:	Debye temperature

$\tau(v_i, v_e)$:	Cooling time
v:	Velocity
x:	Horizontal position of a particle
x':	Horizontal angle of a particle
y:	Vertical position of a particle
y':	Vertical angle of a particle
z:	Longitudinal position
Z:	The atomic number
Z_W, z_W:	Position of the beam waist

LIST OF FIGURES

LIST OF TABLES

ACKNOWLEGMENTS

I would like to express my gratitude to my advisor, Prof. Ilan Ben-Zvi, for introducing me to the RHIC electron-cooling project and for his encouragement and guidance. I'm thankful to Dr. Alexei Fedotov, Dr. Jörg Kewisch, Prof. Vladimir N. Litvinenko, and Prof. Stephen Peggs for many valuable discussions on accelerator physics and electron cooling physics. I want to thank Prof. YongXiang Zhao, who gave me many suggestions and help on the RF experiments. Many people also contribute on the design and construction of the experimental set up. Among them are Prof. Peter Johnson, Francis Loeb, Andrew Burrill, David Pate, T. Srinivasan-Rao, John Smedley, M. Montemagno, J. Walsh, R. Dinardo, and W. Chen. I would like to thank Dr. Zvi Segalov, who has participated in the design, construction and measurement of the Secondary Emission Enhanced Photoinjector experiment. I want to thank my committee members Prof. Ilan Ben-Zvi, Prof. Stephen Peggs, Prof. Jacobus Verbaarschot, Dr. Jörg Kewisch and Prof. Thomas Hemmick.

Financial support came from the US Department of Energy and the US NAVY.

CHAPTER 1. INTRODUCTION

1.1. The Relativistic Heavy Ion Collider (RHIC) electron cooling project

The development of nuclear physics experimental research resulted in a sharp increase in the requirements for particle-beam quality. It is especially important to obtain beams of high luminosity. The luminosity of a collider is given by:

$$L = \frac{N_i^2 f_b}{4\pi\varepsilon\beta_{IP}} \qquad (1.1.1)$$

where ε is the emittance of the bunches, N_i is the number of particles in the bunch, β_{IP} is the beta function at the interaction point and f_b is the bunch repetition frequency.

The average luminosity of RHIC over 10 hours is many times smaller than its initial peak luminosity because of the increase in transverse and longitudinal-emittances due to Intra Beam Scattering (IBS), beam-beam effects, and external noise.

Electron cooling may be the most effective way to suppress or reverse the growth of the beam's emittance, and may even increase peak luminosity.

Electron cooling was first proposed by Prof. G. Budker in the late sixties as a method of improving the properties of stored ion beams. It was experimentally confirmed at Novosibirsk and later at CERN and many other places. All existing coolers are designed for low energy ion rings where the cooling is more efficient and the typical cooling time is about 1 second. The implementation of electron cooling in RHIC is more difficult due to the high energy of the ion beam. We will give introduce electron cooling theory in chapter 2.

For efficient cooling of the RHIC ion beam the electron beam must have about $1.2 \cdot 10^{11}$ particles per bunch (~20nC) at an energy of 55 MeV (γ =107). The energy spread must be less than $2 \cdot 10^{-4}$ and the transverse temperature must be less than 1000 eV in the electron bunches' co-moving frame. The beam radius in the cooling section is ~1mm. The bunch frequency is 9.4 MHz for 120 ion bunches in RHIC. This makes it necessary to use the super-conducting Energy Recovery Linac (ERL). A strong cooling solenoid (1~5Tesla) is necessary to aid the cooling process.

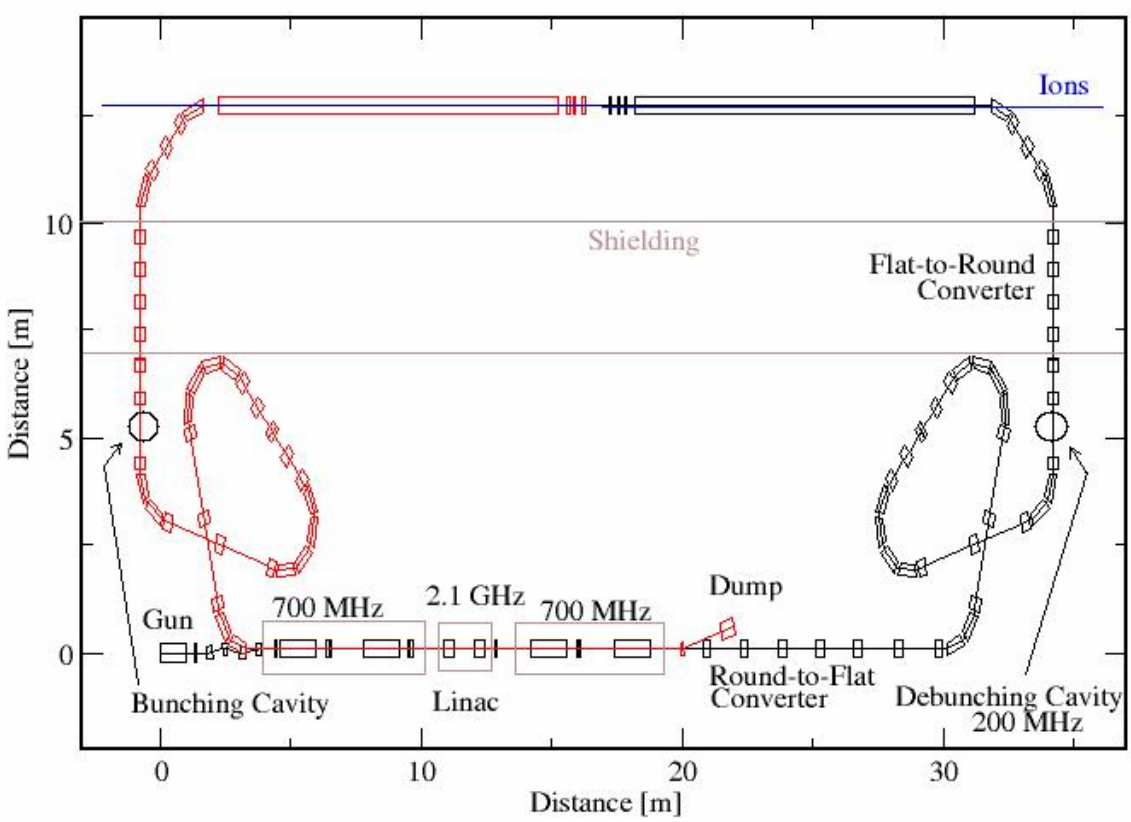

Figure1.1: Layout of the RHIC's electron-cooling facility

Fig.1 illustrates the layout of the proposed electron cooling system for the RHIC. Electron bunches are produced in the gun and accelerated in a superconducting linac. A

beam-transport loop stretches the bunch length and a debunching cavity reduces the energy spread before the electrons are merged with the ion beams. A strong solenoid must be installed in the cooling section to enhance the cooling effect. The electron bunches are then shortened by a combination of a second cavity transport loop, and then decelerated in the linac before they are dumped.

1.2. Emittance compensation for a "magnetized" beam.

As mentioned above, the cooling section has a strong solenoid to enhance the cooling. When the beam enters or leaves a longitudinal magnetic field (such as the cooling solenoid) its angular momentum changes. To ensure zero angular momentum inside the cooling solenoid, an equivalent longitudinal magnetic field must be applied at the cathode according to Busch's theorem. The beam emerging from the cathode is described as being "magnetized".

For strongly magnetized beam the angular momentum significantly changes the dynamics of the electron beam, which can lead to a significant growth of the emittance. We will first review the emittance compensation mechanics for non-magnetized beam and then find an optical solution that minimizes the beam emittance growth in the presence of strong space-charge forces and angular momentum.

1.3. Beam dynamics simulation for RHIC e-cooling.

The computer code PARMELA [1] has been used to investigate the beam dynamics of various configurations of the RHIC e-cooling system. PARMELA is arguably the most commonly used code for linear accelerator systems in the presence of space charge. In

particular, it has been found in reasonably good agreement with experiments when simulating laser photocathode RF guns.

1.4. Diamond Amplified Photocathode R&D

One of the key problems in RHIC e-cooling project is the required high current and large bunch charge, 100mA~200mA average electron current with a charge of 20nC per bunch. We found that the large bunch charge calls for RF fields that are practical only with superconducting RF guns. Using the available photo-cathode materials requires a very large average laser power, leading to a complicated laser system which is also expensive. In addition, the contamination of the superconducting cavity with the cathode materials (that usually contain cesium for best quantum efficiency) may pose a significant contamination problem to the cavity. We will study a promising way to solve these problems: the diamond amplified photocathode.

CHAPTER 2. ELECTRON COOLING

The mechanics of electron cooling can be explained as heat flow from the ions to the electrons, mediated through Rutherford scattering in the mixture of hot (ions) and cold (electrons) gas.

2.1. Liouville's theorem and emittance

Emittance is closely related to the temperature of ion or electron beams. A particle is represented by a point in a conceptual Euclidean space of six dimensions, combining configuration space (q_i) and canonical momentum space (p_i). All particles of a beam will occupy a volume in this six-dimensional hyperspace which is called phase space.

Lets define a particle density n(p,q,t) and velocity vector $\mathrm{v} = \{\dot{q}_i, \dot{p}_i\}$ in phase space. The particle motion in phase space must obey the continuity equation:

$$\nabla \cdot (n\mathrm{v}) + \frac{\partial n}{\partial t} = n\nabla \cdot \mathrm{v} + \mathrm{v} \cdot \nabla n + \frac{\partial n}{\partial t} = 0 . \tag{2.1.1}$$

If a Hamiltonian $H(q_i,p_i,t)$ can be defined for the system, then Hamilton's equations

$$\dot{q}_i = \frac{\partial H}{\partial p_i}, \dot{p}_i = -\frac{\partial H}{\partial \dot{q}_i} \tag{2.1.2}$$

are valid. As a result

$$\nabla \cdot \mathrm{v} = \sum_{i=1}^{3} \left(\frac{\partial^2 H}{\partial p_i \partial q_i} - \frac{\partial^2 H}{\partial q_i \partial p_i} \right) = 0 \tag{2.1.3}$$

$$\frac{dn}{dt} = \frac{\partial n}{\partial t} + \mathrm{v} \cdot \nabla n = 0 \tag{2.1.4}$$

That means that the density of points in phase space is constant, or alternatively, the phase space volume is constant:

$$\iint d^3 q_i d^3 p_i = const. \tag{2.1.5}$$

It is more convenient to use the variables (q_i,P_i) where P_i is the mechanical momentum

$$P_i = p_i - qA_i \tag{2.1.6}$$

where q is the charge of the particle and A_i is the vector potential. By transforming (q_i,p_i) to (q_i,P_i) we have

$$\iint D d^3 q d^3 p = \iint d^3 q d^3 P \tag{2.1.7}$$

where

$$D = \frac{\partial(q_1, q_2, q_3, p_1, p_2, p_3)}{\partial(q_1, q_2, q_3, P_1, P_2, P_3)} = 1 \tag{2.1.8}$$

is the Jacobian of the transformation. As D=1, Liouville's theorem also applies to (q_i,P_i). As long as there is no coupling between longitudinal motion and transverse motion, the longitudinal phase space (2-d) area and transverse phase space volume (4-d) are conserved separately. Furthermore, if there is no coupling between horizontal motion (x direction) and vertical motion (y direction), the phase space area in both directions remains constant.

It is convenient to use the variables (x,y) and the angles $(x',y'=v_{x,y}/v_z)$ in transverse dimensions, i.e., trace space. The emittance is defined as the area in the 2-d trace space (x, x' and y, y'). The difference between the phase space and trace space is a constant $mc\beta_0\gamma_0$ (where m is the mass of particle, β_0 and γ_0 are relativistic constants). Hence, the normalized emittance (product of emittance and $\beta_0\gamma_0$) is a constant.

Both in the literature and in experiments, the most often used measure is the rms emittance. The 1-σ rms emittance ε_x in (x, x') trace space which includes ~40% of the particles for a Gaussian distribution, is defined as:

$$\varepsilon_x = \sqrt{\langle x^2 \rangle \langle x'^2 \rangle - \langle xx' \rangle^2} \tag{2.1.9}$$

where the brackets (< >) represent averages in trace space. The normalized emittance (in x-direction) is $\varepsilon_n = \beta_0 \gamma_0 \varepsilon_x$. Once the trace space is upright, i.e., the beam is at the waist or the crest where $\langle xx' \rangle = 0$, then

$$\varepsilon_n = \beta_0 \gamma_0 \sigma_x \sigma_{x'} \tag{2.1.10}$$

where σ means the rms value.

2.2. The temperature of ion and electron beams

In the frame $\mathcal{R}_0$ moving with the average velocity $\vec{v}_0$ of ions or electrons, the rms ($\sqrt{\langle v^2 \rangle}$) velocities can be compared to the definition of the temperature T of a dilute gas in thermodynamics using the classical relation

$$\frac{3}{2} k_B T = \frac{1}{2} m_{i,e} \langle v_{i,e}^2 \rangle = \frac{1}{2} m_{i,e} \langle v_x^2 + v_y^2 + v_z^2 \rangle \tag{2.2.1}$$

where k_B is the Boltzmann constant and $m_{i,e}$ the ion or electron mass. v_x is the horizontal velocity, v_y is the vertical velocity and v_z is the longitudinal velocity. We can associate for each individual rms velocity component a temperature

$$k_B T_x = m_{i,e} \langle v_x^2 \rangle,\ k_B T_y = m_{i,e} \langle v_y^2 \rangle,$$

$$k_B T_z = k_B T_{//} = m_{i,e} \langle v_z^2 \rangle,\ k_B T_{\perp} = m_{i,e} \langle v_{\perp}^2 \rangle \tag{2.2.2}$$

where the symbol // means parallel to $\vec{v}_0$ and $\perp$ perpendicular to $\vec{v}_0$, $v_\perp^2 = v_x^2 + v_y^2$.

Assuming the beam is upright in trace space, the transverse temperature $T_\perp$ in the frame $\mathcal{R}_0$ is related to ε_n as:

$$k_B T_\perp = m_{i,e} c^2 \beta_0 \gamma_0 \frac{\varepsilon_n}{\beta_\perp} \qquad (2.2.3)$$

where $\beta_\perp$ is the betatron function of the beam. Assuming the temperature in the laboratory frame $\mathcal{R}_L$ is defined as $k_B T_{\perp L} = \gamma_0 m_{i,e} v_{\perp L}^2$ where $v_{\perp L}$ is the transverse velocity in $\mathcal{R}_L$, then $T_{\perp L} = T_\perp / \gamma_0$. A reduction of ε_n can reduce $T_\perp$. Assuming the beta function of RHIC Gold ion at cooling section is 60m, the ion transverse temperature $k_B T_{i\perp}$ at cooling section is ~10^5eV.

The longitudinal temperature $T_{//}$ is related to the longitudinal momentum spread in the laboratory frame through:

$$k_B T_{//} = m_{i,e} c^2 \beta_0^2 \delta^2 \qquad (2.2.4)$$

where $\delta = \frac{\Delta p}{p_0}$ is the momentum spread measured in the laboratory frame $\mathcal{R}_L$. A reduction of δ reduces $T_{//}$. Generally δ is a small number after acceleration (10^{-3}~10^{-4}). As a result, $T_{//} << T_\perp$. For RHIC Gold ion beam, δ is typically less than 5×10^{-4} so that the longitudinal ion temperature is less than $0.13\text{eV}/k_B$.

2.3. Cooling force

2.3.1 Heating sources of the ion beam.

There are 3 main heating sources of ion beam and, without cooling, these lead to an emittance growth so that the luminosity is reduced with time. the heat sources are: the effect of residual gas, intrabeam scattering (IBS), and the beam-beam effect at intersection points (IP). IBS is the dominated heating source in RHIC.

2.3.2 Relation between cooling force and cooling time.

The cooling time τ in frame $\mathcal{R}_0$ is actually a function of relative velocity between ions and electrons.

$$\frac{1}{\tau(v_i, v_e)} = -\frac{F(v_i, v_e)}{p_i} \tag{2.3.1}$$

where $F(v_i, v_e)$ is the cooling force which is a function of ion velocity v_i, electron velocity v_e and the ion momentum p_i so that the calculation of the cooling time is not straightforward.

In the lab frame $\mathcal{R}_L$, the cooling time is longer, $\tau_{Lab} = \gamma_0 \tau$.

2.3.3 Cooling force without magnetic field

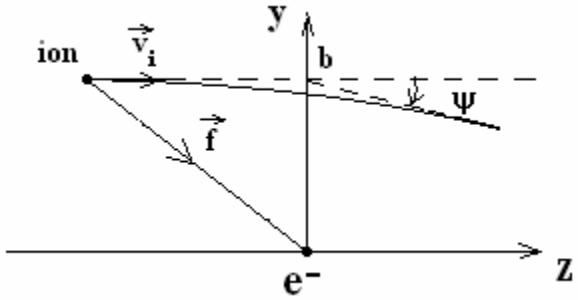

Figure 2.1: Geometry of the single electron-ion interaction

Let us start with the single electron-ion interaction represented by fig.2.1. The ion initially at position (-∞, b) with velocity v_i interacts with an electron at rest at (0,0). b is the impact parameter. Due to the Coulomb force exerted between the two particles, the ion trajectory will deviate by an angle, which is small for most impact parameters. The deviation ψ is given by:

$$ctg\left(\frac{\psi}{2}\right) = -\frac{bm_e v_i^2}{Z\phi^2} \tag{2.3.2}$$

where Z is the atomic number of ion and $\phi^2 = \frac{e^2}{4\pi\varepsilon_0}$. The energy loss by the ion which is that gained by the electron is approximately:

$$\Delta E(b) = \frac{2Z^2\phi^4}{m_e v_i^2 b^2} \tag{2.3.3}$$

The effective collision length is actually on the scale of b. So the effective collision time is:

$$\Delta t \approx \frac{b}{v_i} \tag{2.3.4}$$

Now consider the multiple collisions with electron density n_e with all possible impact parameters b. The energy lost by the ion per unit of length is:

$$\frac{dE}{dz} = \frac{4\pi Z^2\phi^4}{m_e v_i^2} n_e \ln\left(\frac{b_{\max}}{b_{\min}}\right) \tag{2.3.5}$$

where $b_{\min} = \frac{Z\not{e}^2}{m_e v_i^2}$ is the impact parameter of maximum momentum transfer, i.e., head-on collision.

We take $b_{\max} = \min(\lambda_D, r_0, v_i \Delta T)$ where λ_D is the Debye length caused by electric field shielding of a plasma, r_0 is the electron beam radius and ΔT is the transit time in cooling section. For RHIC cooling the maximum impact parameter is given by $b_{\max} = v_i \Delta T$.

Assume the electrons have a density distribution as a function of velocity $f(v_e)$, which generally can be expressed in a Gaussian form. The friction force is then obtained by integrating over the distribution in velocity:

$$\vec{F} = -\frac{4\pi Z^2 \not{e}^4 n_e}{m_e} L_c \int \frac{\vec{v}_i - \vec{v}_e}{\left|\vec{v}_i - \vec{v}_e\right|^3} f(v_e) d^3 v_e \qquad (2.3.6)$$

where $L_c = \ln\left(\frac{b_{\max}}{b_{\min}}\right)$ which can be assumed to be a constant.

In the case of a Maxwellian distribution of the electron velocities, for which $\Delta_{e//} << \Delta_{e\perp}$,. the following asymptotic expressions of the force have been derived [2]:

$$\textit{Longitudinal } (v_{i\perp} = 0): F_{//}(v_{i//}) = -\frac{4\pi Z^2 \not{e}^4}{m_e} n_e L_c \begin{cases} \frac{1}{v_{i//}^2}; & |v_{i//}| >> \Delta_{e\perp} \\ \frac{1}{\Delta_{e\perp}^2}; & \Delta_{e\perp} >> |v_{i//}| >> \Delta_{e//} \\ \frac{v_{i//}}{(2\pi)^{3/2} \Delta_{e\perp}^2 \Delta_{e//}}; & |v_{i//}| << \Delta_{e//} \end{cases} \qquad (2.3.7)$$

$$\textit{Transverse } (v_{i//} = 0): \quad F_{\perp}(v_{i\perp}) = -\frac{4\pi Z^2 \not{e}^4}{m_e} n_e L_c \begin{cases} \frac{1}{v_{i\perp}^2}; & |v_{i\perp}| >> \Delta_{e\perp} \\ \frac{\sqrt{\pi}}{8} \frac{v_{i\perp}}{\Delta_{e\perp}^3}; & |v_{i\perp}| << \Delta_{e\perp} \end{cases}$$

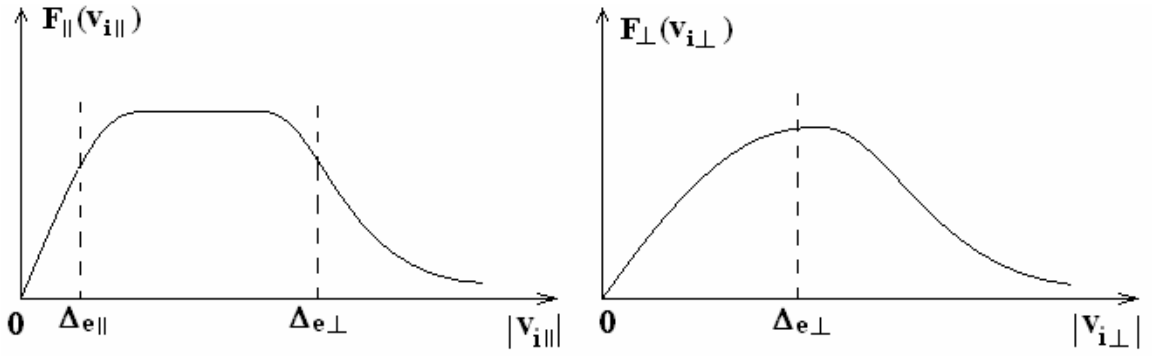

Figure 2.2: Non-magnetized cooling force

Fig.2.2 Schematic curves show the longitudinal and transverse friction force as a function of ion velocity and electron velocity. We observe that the forces are dependent on ion velocities, for large ion velocities the forces scale as $1/v_i^2$ and for small velocities the forces are proportional to v_i.

2.3.4 Cooling force with magnetic field

When an electron beam is in a longitudinal magnetic field the transverse motion appears to be frozen. The electrons rotate around their axis at the cyclotron frequency ω_c with the Larmor radius r_L and Larmor period L_L.

$$\omega_c = \frac{eB}{m_e}, \quad r_L = \frac{m_e v_{e\perp}}{eB}, \quad L_L = 2\pi\gamma_0 \frac{mc}{eB} \tag{2.3.8}$$

If the impact parameter b is much larger than r_L and if the collision time $\Delta t = b/v_i$ is much larger than $2\pi/\omega_c$, then the electron transverse motion is "frozen" and thus the cooling efficiency is determined by the electron longitudinal temperature $T_{e//}$, which is

much smaller than transverse temperature $T_{e\perp}$. Cooling is highly improved. This type of collision is often called adiabatic collision ($b >> r_L$).

The case where $b_{\min} < b < r_L$ is called a fast collision and it looks like the case without magnetization. If we increase the magnetization, then the Larmor radius r_L reduces, therefore the adiabatic region increases and cooling improves.

An analytic formula for the friction force of magnetized cooling [3] [4] uses the approximation of an infinite magnetic field. The following semi-empirical formula (V-P) [5] for the cooling force was introduced by V. V. Parkhomchuk:

$$\vec{F} = -\frac{4Z^2 \not{e}^4 n_e}{m_e} \frac{\vec{v}_i}{\left(v_i^2 + v_{eff}^2\right)^{3/2}} \ln\left(\frac{b_{\max} + b_{\min} + r_L}{b_{\min} + r_L}\right) \qquad (2.3.9)$$

where $v_{eff} = \sqrt{v_{e//}^2 + \Delta v_{e\perp}^2}$ and $\Delta v_{e\perp}$ is the transverse velocity due to transverse magnetic and electric fields (imperfection of cooling solenoid). For RHIC e-cooling $b_{\min}$ is negligible.

2.3.5 Matching of electron beam with cooling solenoid

When the electron beam optics consists of non-dissipative axial invariant elements, such as drifts, solenoids, round electrostatic lenses or axisymmetric RF fields, the canonical angular momentum (CAM) of any particle $M = xp_y - yp_x$ is preserved. This statement is also known as Busch's theorem.

Since we have a strong solenoid field in the cooling section we need, according to Busch's theorem, to apply equivalent solenoid field on cathode:

$$B_s r_s^2 = Br^2 \qquad (2.3.10)$$

where B_s, r_s, B and r are the solenoid field and beam radii on the cathode and in the cooling solenoid, respectively. The electron beam size in the cooling solenoid is determined by the ion beam size, which is about 1mm rms in radius and about 20cm rms in bunch length in RHIC. The use of a cooling solenoid requires a strong solenoid field on the cathode according to equation (2.3.10). This introduces an effective emittance $\mathcal{M}$ to electron beam envelope equation (see below). For the case of electron-cooling of RHIC, with a solenoid field of 5 T and beam rms diameter of 2 mm in the cooling solenoid, we get $\mathcal{M}$=380mm.mr.

When the beam enters the cooling solenoid the beam should have the right beam size (rms 1mm) and is in the beam's waist so that equation (2.3.10) applies. Without the space charge effect the electron in the cooling solenoid rotates along the straight solenoid field line with constant Larmor radius r_L. If we take the space charge effect into account the beam should be slightly converging at cooling solenoid entrance so that the beam waist is at the middle of cooling solenoid. For RHIC electron-cooling conditions the space charge effect (F_{Sch}) is dramatically reduced not only by its high γ_0 ($F_{Sch} \propto 1/\beta_0^3\gamma_0^3$) but also through ion beam neutralization. Thus the space charge effect can be neglected in the cooling section.

From (2.3.9) one can see that cooling force is dependent on Larmor radius r_L. Ideally we should optimize the distribution of the electron Larmor radii to maximum the friction force averaged over all ions using (2.3.9). Approximately one uses the rms value of r_L to evaluate the cooling force.

CHAPTER 3. EMITTANCE COMPENSATION FOR NON-MAGNETIZED BEAM

3.1. The emittance of a bunched beam

We start from the general paraxial envelope equation for a coasting beam:

$$\sigma'' + \sigma' \frac{\gamma'}{\beta^2 \gamma} + K_r \sigma - \left(\frac{p_\theta}{mc\beta\gamma} \right)^2 \frac{1}{\sigma^3} - \left(\frac{\varepsilon_n}{\beta\gamma} \right)^2 \frac{1}{\sigma^3} - \frac{K_s}{\beta^3 \gamma^3 \sigma} = 0 \qquad (3.1.1)$$

where σ indicates the rms beam spot size, the prime indicates differentiation with respect to longitudinal position z, ε_n is the normalized thermal emittance, $K_s = I/2I_0$ is the perveance and $I_0 = 17000A$ is the Alfvén current. $K_r \equiv -F_r / r\beta^2 \gamma mc^2$ indicates the effects of an external linear focusing channel.

Although the real accelerating gradient in a RF cavity is varying along z, one may calculate the motion using a constant (average) acceleration [6]. The small oscillation of the envelope about the constant acceleration envelope can be ignored. As discussed in Ref. [6] K_r for a RF accelerating system can be expressed as:

$$K_r = \left(\frac{\eta}{8} + b^2 \right) \left(\frac{\gamma'}{\gamma \sin(\phi)} \right)^2 \qquad (3.1.2)$$

where $b = cB_z / E_0$ is the external solenoid field superposed on the RF cavity field (E_0 is the peak field on axis of the cavity).

$$\gamma' = \alpha k \sin(\phi) \qquad (3.1.3)$$

is the accelerating gradient where $\alpha = eE_0 / 2kmc^2$ represents the dimensionless amplitude of the accelerating field associated with the RF frequency ν_{RF} ($k = 2\pi\nu_{RF} / c$),

$\phi = \omega t - kz + \phi_0$ is the particle phase with respect to RF field wave, and ϕ_0 is the RF phase at which the beam has maximum acceleration. The quantity η in (3.1.2) is a measure of the higher spatial harmonic amplitudes of the RF wave and is generally very close to unity in practical RF structures. In case $\gamma' = 0$ (no acceleration) K_r becomes to $K_r = \left(\frac{qB_z}{2mc\beta\gamma} \right)^2$ which is the focusing strength of a solenoid.

Equation (3.1.1) is Lawson's expression for the evolution of the rms envelope in the paraxial limit [7] with an extra defocusing term induced by p_θ which is the rms canonical momentum on the cathode:

$$p_\theta = \gamma m \sigma_s^2 \dot{\theta}_s + qA_\theta \sigma_s \approx qA_\theta \sigma_s = qB_s \sigma_s^2 / 2 \qquad (3.1.4)$$

where B_s and σ_s are the longitudinal magnetic field and the rms beam size on the cathode respectively. We define $\mathcal{M} = \frac{p_\theta}{mc} = \frac{qB_s \sigma_s^2}{2mc}$ as the magnetization of an electron. $\mathcal{M}$ is equivalent to the thermal emittance ε_n in the envelope evolution. In the ideal case $\mathcal{M}$ can be removed by applying a longitudinal magnetic field (the cooling solenoid). The beam is "un-rotated" in lab frame. Because of the difference of slice motions, the beam can only be matched to the cooling solenoid on some average, and part of the magnetization emittance $\mathcal{M}$ ends up as an increase of the rms Larmor radius.

The RF accelerating system requires the beam be bunched. For a bunched beam the thermal emittance ε_n is generally very small (~1eV in momentum) when compared to the emittance due to the slices' relative motion. Therefore the thermal emittance ε_n is ignored in the following calculations. For a non-magnetized beam the emittance for the entire beam is dominated by the correlation between the transverse phase space angle

(σ/σ') and the longitudinal bunch position coordinate $\zeta = z - z_0$, where z_0 is the center of the bunch. This correlation is caused by the time dependent RF acceleration and the local space-charge field, which is described by the geometrical factor [8] $g(\zeta)$. $g(\zeta)$ is given by

$$g(\zeta) = e^{-\zeta^2/2\sigma_z^2}\left(1+\frac{A^2}{\gamma^2}\left\{\left(1-\frac{\zeta^2}{\sigma_z^2}\right)\left[\frac{1}{2}+\ln\left(\frac{A}{\gamma}\right)\right]-1\right\}\right) \approx e^{-\zeta^2/2\sigma_z^2} \qquad (3.1.5a)$$

for a Gaussian distribution of aspect ratio $A = \sigma_r/\sigma_z$ with $A/\gamma << 1$ and

$$g(\zeta) = 1-\frac{2A^2}{\gamma^2}\left[1+12\left(\frac{\zeta}{L}\right)^2+80\left(\frac{\zeta}{L}\right)^4\right] \approx 1 \qquad (3.1.5b)$$

for a uniform distribution of aspect ratio $A = R/L$ with $A/\gamma << 1$, where R is the beam radius and L is the beam length. If $A/\gamma >> 1$ then $g(\zeta) \approx 1$ in both cases.

The space-charge force dependence on ζ is then expressed as:

$$K_s(\zeta) = Ig(\zeta)/2I_0 \qquad (3.1.6)$$

The envelope equation for a slice of the bunch can be expressed as:

$$\sigma''(\zeta)+\sigma'(\zeta)\frac{\gamma'}{\beta^2\gamma}+K_r\sigma(\zeta)-\left(\frac{p_\theta}{mc\beta\gamma}\right)^2\frac{1}{\sigma^3(\zeta)}-\frac{K_s(\zeta)}{\beta^3\gamma^3\sigma(\zeta)} = 0 \qquad (3.1.7)$$

This equation is valid under the following assumptions:

1. The problem can be treated in the paraxial approximation, i.e., σ and σ' are very small enough to consider the transverse field linear over the beam.
2. We assume that all the particles have the same β and γ.
3. The motion of the particles is laminar, i.e., the trajectories do not cross each other.

We assume the beam transverse charge density is uniform for any slice, so that the transverse space-charge force is linear in r and the laminar condition is always met.

When the beam is near the cathode, the aspect ratio $A/\gamma >> 1$, as discussed above, $g(\zeta) \approx 1 = const.$, so that the relative motion of the slices is small, i.e., the slopes of slices ($\sigma(\zeta)/\sigma'(\zeta)$) are essentially independent of ζ. The ratio decreases quickly (in the range of a fraction of RF wave length) under practical RF gun applications. Equation (3.1.5) and equation (3.1.6) immediately become valid and then the motions of slices become dependent on their position on the bunch, thus a transverse – longitudinal correlation is imposed on the bunch. Such a correlation is equivalent to a growth in the projected emittance. The time dependent RF kick and the energy spread of the beam are also the sources of position dependent motion.

The removal of the correlation through appropriate beam envelope manipulation is called emittance compensation [8] [9] [10], and is an important technique to reduce the projected emittance of a bunched beam. This analysis (section 3.2.1), originally performed by Serafini and Rosenzweig [8], introduces the space-charge dominated beam equilibrium in accelerating systems which is termed the invariant envelope and proposes that a beam which follows an invariant envelope has an optimized emittance compensation.

There is a self-consistent distribution of a beam bunch where $K(\zeta)/\sigma^2(\zeta) = f(t)$ is independent of position ζ. Such bunch has a uniform charge density inside a volume which is an ellipsoid of revolution in ζ-r. For this distribution, the potential within the ellipsoid in Cartesian coordinates is given by [11]:

$U(x,y,z) = -A(x^2 + y^2) - Bz^2 + C$, where A, B, and C are constants. (3.1.8)

Then, for both non-magnetized and magnetized beam, (3.1.7) can be expressed as

$$\sigma''(t) + D(t)\sigma(t) = 0 \qquad (3.1.9)$$

for all the slices in the bunch. Here D(t) is the sum of all the factors of focusing or defocusing terms in (3.1.7) and is the same for all slices.

Accordingly, emittance compensation is not required for an ellipsoid distribution. If we could create a laser pulse, which generates such a distribution, the emittance will be small compared to any other distribution. However, such a laser distribution is difficult to produce and even if we had this kind of laser, the complicated emission process on the cathode in which the self-field of the bunch varies as the bunch is generated, the chromaticity effect and the time-dependent RF force, all of which conspire to make the slice motion dependent on its position ζ.

3.2. Emittance compensation for a regular non-magnetized beam

Although the chromaticity effect is correlated with space charge effect one can treat them separately to simplify the analysis. We will first study the space charge effect only, i.e., the particles in the beam have the same β and γ.

3.2.1 Matching of a beam to a π-mode linac

The purpose of this sub-section is to restate the analytical theory of emittance compensation developed by S-R in ref. [3] which is the starting point for the emittance compensation mechanism.

For a non-magnetized beam $\mathcal{M}$ is zero. In a π mode cavity without external field, the envelope equation becomes:

$$\sigma''(\zeta)+\sigma'(\zeta)\frac{\gamma'}{\beta^2\gamma}+K_r\sigma(\zeta)-\frac{K_s(\zeta)}{\beta^3\gamma^3\sigma(\zeta)}=0 \qquad (3.2.1)$$

where $K_r=\eta/8+b^2=\eta/8\approx 1/8$.

Let: $y \equiv \ln(\gamma/\gamma_0)$, $S(\zeta) \equiv I(\zeta)/2I_0\gamma_0\gamma'^2 = K_s(\zeta)/\gamma_0\gamma'^2$ and $\tau(\zeta) \equiv \sigma(\zeta)/\sqrt{S(\zeta)}$

where γ_0 is the energy at cavity entrance, then equation (3.2.1) becomes:

$$\frac{d^2\tau}{dy^2} + \Omega^2\tau = \frac{e^{-y}}{\tau} \tag{3.2.2}$$

where $\Omega^2 = K_r$ which is 1/8 in this case.

Equation (3.2.2) has a general perturbative solution [8],

$$\tau = \left(\tau_0 - \frac{e^{-y_0}}{\tau_0\Xi}\right)\cos[\Omega(y-y_0)] + \frac{e^{-y+(y_0-y)\dot{\tau}_0/\tau_0}}{\tau_0\Xi} + \left[\dot{\tau}_0 + \frac{e^{-y_0}(1+\dot{\tau}_0/\tau_0)}{\tau_0\Xi}\right]\sin[\Omega(y-y_0)]/\Omega \tag{3.2.3}$$

with $\Xi = 1/8 + [1+\dot{\tau}_0/\tau_0]^2$ and the dot represents the differentiation respect to y. There is a special solution,

$$\hat{\tau} = \sqrt{8/3}e^{-y/2},\ (\hat{\sigma} = (2/\gamma')\sqrt{I/3I_0\gamma},\ \hat{\sigma}' = -\sqrt{I/3I_0\gamma^3}) \tag{3.2.4}$$

corresponding to $\hat{\tau}_0 = \sqrt{8/3}e^{-y_0/2}$, $\dot{\hat{\tau}}_0 = -\sqrt{2/3}e^{-y_0/2}$ and $\Xi = 3/8$. This solution has the property that the angle $\theta \equiv \gamma\hat{\sigma}'/\hat{\sigma}$ in the $(\sigma, \gamma\sigma')$ phase space,

$$\theta \equiv \gamma\hat{\sigma}'/\hat{\sigma} = -\gamma'/2 \tag{3.2.5}$$

is constant. The solution $\hat{\sigma}$ (or the equivalent $\hat{\tau}$) is called the invariant envelope. It is the equilibrium state between the focusing force of the average RF acceleration and the defocusing space charge force.

The phase space angle of the invariant envelope in the configuration space (σ, z) $\hat{\delta}_{\sigma,z} \equiv \hat{\sigma}'/\hat{\sigma}$ is:

$$\hat{\delta}_{\sigma,z} = \hat{\sigma}'/\hat{\sigma} = (\gamma'/\gamma)\dot{\hat{\sigma}}/\hat{\sigma} = -\gamma'/2\gamma \tag{3.2.6}$$

If the beam deviates from its invariant envelope by the small-amplitude motion around $\hat{\tau}$ then the perturbation obeys

$$\delta\ddot{\tau} + \Omega^2 \delta\tau = \frac{e^{-y}\delta\tau}{\hat{\tau}^2} \tag{3.2.7}$$

and thus has the general solution

$$\delta\tau = \delta\tau_0 \cos[\omega(y - y_0)] + \frac{\delta\dot{\tau}_0}{\omega}\sin[\omega(y - y_0)], \text{ with} \tag{3.2.8a}$$

$$\delta\dot{\tau} = -\frac{\delta\tau_0}{\omega}\sin[\omega(y - y_0)] + \delta\dot{\tau}_0 \cos[\omega(y - y_0)]. \tag{3.2.8b}$$

where $\delta\tau = \tau - \hat{\tau}$, $\delta\dot{\tau} = \dot{\tau} - \dot{\hat{\tau}}$ and the frequency is $\omega = \sqrt{2\Omega^2 + 1/4} = 1/\sqrt{2}$.

In trace space the solution is:

$$\delta\sigma = \delta\sigma_0 \cos\left[\frac{1}{\sqrt{2}}\ln\left(\frac{\gamma}{\gamma_0}\right)\right] + \sqrt{2}\frac{\gamma_0}{\gamma'}\delta\sigma'_0 \sin\left[\frac{1}{\sqrt{2}}\ln\left(\frac{\gamma}{\gamma_0}\right)\right], \text{ with} \tag{3.2.9a}$$

$$\delta\sigma' = -\frac{1}{\sqrt{2}}\frac{\gamma'}{\gamma}\delta\sigma_0 \sin\left[\frac{1}{\sqrt{2}}\ln\left(\frac{\gamma}{\gamma_0}\right)\right] + \delta\sigma'_0 \frac{\gamma_0}{\gamma}\cos\left[\frac{1}{\sqrt{2}}\ln\left(\frac{\gamma}{\gamma_0}\right)\right] \tag{3.2.9b}$$

where $\delta\sigma = \sigma - \hat{\sigma}$, $\delta\sigma' = \sigma' - \hat{\sigma}'$ and the frequency in the trace space ω_T can be expressed as:

$$\omega_T = \frac{1}{\sqrt{2}}\frac{dy}{dt} = \frac{1}{\sqrt{2}}\frac{c\gamma'}{\gamma} = \frac{2\omega_p}{\sqrt{3}} \tag{3.2.10}$$

with $\omega_p = \sqrt{n_e e^2/\varepsilon_0 \gamma^3 m_e} = (c/\sigma)\sqrt{I/2I_0\gamma^3}$ is the electron transverse plasma frequency.

Fig.3.1 illustrates the physical mechanism of the matching of the beam to the invariant envelope.

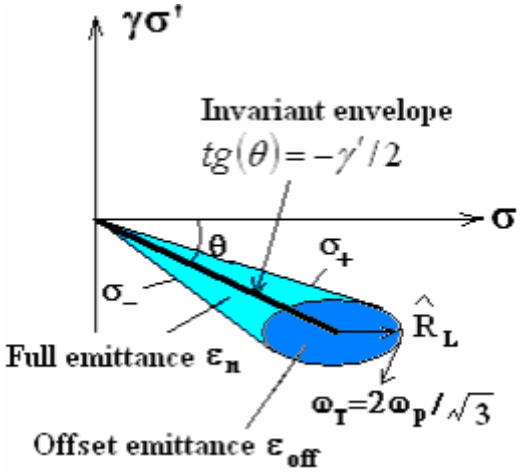

Figure3.1: Mechanism of the matching of the beam to the invariant envelope

The phase space of each slice of the beam is a line from the origin to one point of the ellipse. The colored area in Fig 1.1 is therefore the total emittance of the beam (the area that all particles occupy). According to equation 3.2.6, the invariant envelope lies on a line with an angle -γ'/2. The dark ellipse area is called the offset emittance ε_{off}. It is induced by the spread of the mismatch of the slices and it oscillate about the invariant envelope line at a frequency ω_T. It is a constant of the motion.

$$\varepsilon_{off} \cong \gamma\sqrt{\left\langle(\delta\sigma)^2\right\rangle\left\langle(\delta\sigma')^2\right\rangle - \left\langle\delta\sigma\delta\sigma'\right\rangle^2} \qquad (3.2.11)$$

The emittance of the whole beam can be characterized as:

$$\varepsilon_n \cong \frac{\gamma}{2}\sqrt{\left(\sigma_+^2+\sigma_-^2\right)\left(\sigma_+'^2+\sigma_-'^2\right) - \left(\sigma_+'\sigma_+ + \sigma_-'\sigma_-\right)^2} = \frac{\gamma}{2}\left|\sigma_+\sigma_-' - \sigma_-\sigma_+'\right|. \qquad (3.2.12)$$

This is the normalized emittance for the two extreme slices (σ_+ & σ_- slice). Assuming small deviations of σ_+ & σ_- from the invariant envelope, equation (3.2.12) can be expressed as:

$$\varepsilon_n \cong \frac{\hat{\sigma}}{2}\left|\left(\delta\sigma_0\gamma' + 2\delta\sigma_0'\gamma_0\right)\cos(\psi) + \left(\delta\sigma_0'\gamma_0 - 2\delta\sigma_0\gamma'\right)\sqrt{2}\sin(\psi)\right| \qquad (3.2.13)$$

where $\psi = \left(1/\sqrt{2}\right)\ln\left(\gamma/\gamma_0\right)$ represents the angular change of the orientation of the ellipse during the acceleration.

From (3.2.13) one can see that the total emittance ε_n is proportional to $\hat{\sigma}$, which is proportional to $\gamma^{-1/2}$. This is the adiabatic damping of the emittance. ε_n is also proportional to the value of the absolute term, which is oscillating.

If the ellipse is not round, i.e., a distribution with rms of $\delta\sigma_0$ not equals to rms of $\sqrt{2}\frac{\gamma_0}{\gamma'}\delta\sigma_0'$, the local emittance minima occurs when the orientation of the long axis of the ellipse ($\hat{R}_L$) is aligned with the invariant envelope line. The periodicity of the emittance minima ω_{em} is half of the period of the perturbations about the invariant envelope:

$$\omega_{em} = 2\omega_T = 4\omega_p/\sqrt{3}\,. \qquad (3.2.14)$$

From the above analysis one can find the minimum emittance at some position (experiment position z_{exp}) by first creating a beam that matches the invariant envelope as close as possible so that ε_{off} and the nonlinearity induced ε_{off} increase is small. Second, $\hat{R}_L$ should be parallel to the invariant envelope axis at z_{exp}.

When ε_n is comparable to ε_{off} the emittance compensation is halted by nonlaminar (crossover) processes.

To match the invariant envelope of an actual limited length linac working at π-mode (as shown in fig.3.2 one must include the effect of the focusing at linac entrance and the

defocusing effect at the exit.

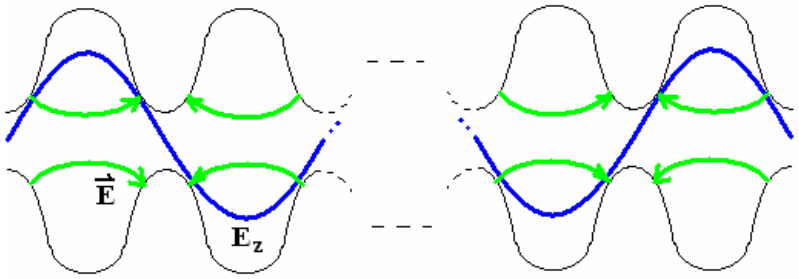

Figure 3.2: Schematic plot of an n-cell π-mode linac. The green lines represent the field lines while the blue line represents the field strength on axis

The effect of the entrance and exit shown in fig.3.2 can be described as [6] that the beam experiences a kick with $\theta = \sigma'/\sigma = -\gamma'/2\gamma$ (negative means converging) in phase space at entrance while the kick at exit is $\theta = \sigma'/\sigma = \gamma'/2\gamma$. This requires that the beam has initial beam size given by

$$\sigma_i = (2/\gamma')\sqrt{I/3I_0\gamma_i} \tag{3.2.15}$$

with vanishing divergence and as a result the beam has beam size

$$\sigma_f = (2/\gamma')\sqrt{I/3I_0\gamma_f} \tag{3.2.16}$$

at linac exit with vanishing divergence.

One must also consider the rotation of the ellipse. Assume that we want to use the beam at a point $z_{\exp}$, which is located at the linac exit. Let the angle between $\hat{R}_L$ and the σ axis be θ_0 at the linac's entrance z_0. Then $\hat{R}_L$ should be parallel to the σ axis at $z_{\exp}$ in order to obtain minimum emittance at $z_{\exp}$, i.e. $\psi = (1/\sqrt{2})\ln(\gamma/\gamma_0) = \theta_0$. Given that the acceleration gradient is γ' then the linac length should be given by:

$$z_{\exp} - z_0 = \frac{\gamma_0}{\gamma'}\left(e^{\sqrt{2}\theta_0} - 1\right) \tag{3.2.17}$$

3.2.2. Matching of RF gun

Consider a multi-cell RF gun structure showing in fig.3.3.

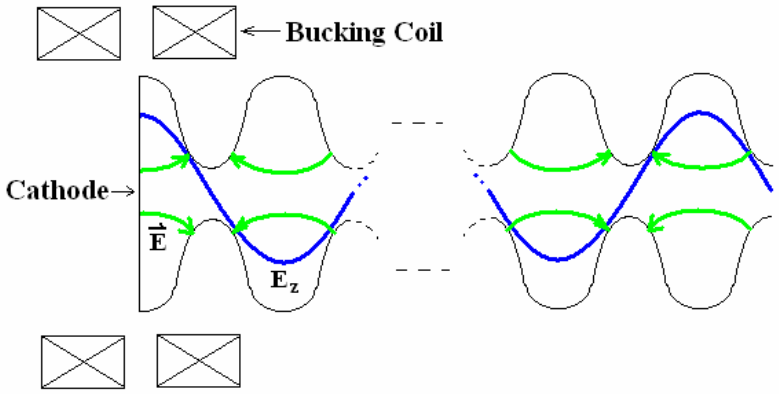

Figure 3.3 A multi-cell RF gun. The bucking coil makes the longitudinal magnetic filed on cathode 0. Green lines: electric filed lines. Blue line: field strength on axis

Assuming the simplification that the beam is relativistic on cathode, the RF kick in the first half cell is given by [12]:

$$\theta_0 = \sigma'/\sigma = \gamma'/\gamma \tag{3.2.18}$$

In order to match its invariant envelope the beam should have an initial convergence angle of $\theta_0 \approx -\gamma'/\gamma$ and a beam size according to equation (3.2.15) on cathode. If the beam is not relativistic, the RF defocusing strength is even larger and the required initial converging angle which is even larger. When the beam leaves a flat cathode the electrons

move out parallel to the axis. A strong focusing solenoid field (bucking coil) close to cathode is necessary to avoid too much deviation from the invariant envelope.

One can also make the first half cell longer to reduce the RF defocusing strength in the first half cell so that the initial mismatch is reduced. An alternate, more effective way to reduce the initial mismatch is to recess the cathode, so that the effective RF defocusing in the first half cell is reduced. The recess is accompanied by the reduction of the required solenoid strength and the sacrifice of electric field on cathode.

It is impossible to apply external solenoid focusing inside a super-conducting gun. Therefore the recess of the cathode is the only way to have small deviation from the invariant envelope. As mentioned in section 3.2.1 a parallel beam at the exit from acceleration region is necessary to match the invariant envelope. Thus, ideally the recess should make the beam at the gun exit parallel.

Given the gun's average accelerating gradient γ'_G and the laser bunch length, one can easily find the current I_{GF} (depends on the bunch length) and the energy (γ_{GF}) of the beam at gun exit from PARMELA or similar codes. These 2 parameters are less sensitive to the beam spot size on cathode σ_c. Therefore the invariant envelope $\hat{\sigma}_{GF}$ at gun exit can be estimated from equation (3.2.15): $\hat{\sigma}_{GF} = (2/\gamma'_G)\sqrt{I_{GF}/3I_0\gamma_{GF}}$. The invariant envelope $\hat{\sigma}_G$ before the gun exit is roughly proportional to $1/\sqrt{\gamma_G}$, where $\gamma_G = 1+\gamma'_G z$ is the beam energy in the gun. From here one can estimate the average invariant envelope of the beam $\bar{\hat{\sigma}}_G$ in the gun:

$$\frac{\bar{\hat{\sigma}}_G}{\hat{\sigma}_{GF}} = \frac{1}{Z_{GF}}\int_0^{Z_{GF}} \sqrt{\frac{1+\gamma'_G Z_{GF}}{1+\gamma'_G z}}\,dz \qquad (3.2.19)$$

where Z_{GF} is the gun length. The ratio $\bar{\hat{\sigma}}_G / \hat{\sigma}_{GF}$ is about 1.5 for the practical applications. For example, assume $\gamma'_G = 30/\mathrm{m}$ and Z_{GF}=0.3m, then $\bar{\hat{\sigma}}_G / \hat{\sigma}_{GF} = 1.52$. In fact, $\bar{\hat{\sigma}}_G$ should be larger than derived from equation (3.2.19) because near the cathode $\bar{\hat{\sigma}}_G$ is higher due to the higher current which is inverse proportional to the bunch length. Assuming the spot size doesn't change very much in the short RF gun, one can roughly estimate σ_c to be $\bar{\hat{\sigma}}_G$, i.e.:

$$\sigma_c \geq 1.5\hat{\sigma}_{GF} = (3/\gamma'_G)\sqrt{I_{GF}/3I_0\gamma_{GF}} \qquad (3.2.20)$$

3.2.3. Matching of the beam for a compact RF gun and booster linacs

For a superconducting RF gun the number of cells must match the available RF power. It is common to employ a compact RF gun (½ cell to 3½ cell), if necessary followed by a drift space and a booster cavity. In this configuration the beam is focused near the cathode or end of the gun by a strong solenoid to compensate the initial mismatch of the beam. Furthermore, the solenoid must be strong enough to make the beam convergent. The beam emittance is minimized near the beam waist by the rotation of $\hat{R}_L$ and the beam forms a space-charge-dominated beam waist. The booster cavity entrance is placed at this point for further emittance compensation. The waist size should match the invariant envelope associated with the beam current and the cavity accelerating gradient.

3.2.4. Beam dynamics in a drift space

In a drift space, the generalized envelope equation is:

$$\nu''(z) - 1/\nu(z) = 0 . \tag{3.2.21}$$

$\nu(z) \equiv \sigma(z)/\sqrt{P}$ is the generalized beam size. In this section, "beam size" refers to this generalized beam size. $P = I/2I_0\gamma^3 = Qc/2\sqrt{2\pi}I_0\gamma^3\sigma_z$ is the normalized, relativistic perveance where σ_z and Q are the rms bunch length and charge of the bunch, respectively. The longitudinal charge distribution is assumed to be Gaussian.

The integral form of equation (3.2.21) is:

$$\int_1^{\nu/\nu_i} \frac{dx}{\sqrt{\nu_i'^2 + 2\ln x}} = \frac{z - z_i}{\nu_i} \tag{3.2.22}$$

where the subscript i stands for the initial position, which is the beginning of the drift space.

Although there is no analytical solution of equation (3.2.22), the envelope can be approximated near the beam waist by a quadratic function if the beam is converging ($\nu' < 0$):

$$\nu = \nu_W + \frac{(z - z_W)^2}{\nu_W} \tag{3.2.23}$$

in the range $|z - z_W| \le \nu_W$ where z_W is the position of the beam waist and ν_W is the beam waist size. The divergence of a beam near the beam waist is then

$$\nu' = \frac{d\nu}{dz} = \frac{2(z - z_W)}{\nu_W} . \tag{3.2.24}$$

The relative position of the beam waist $Z_W \equiv z_W - z_i$ can be expressed as:

$$Z_W(\nu_i, \nu_i') = \nu_i \int_{e^{-\nu_i'^2/2}}^1 \frac{dx}{\sqrt{\nu_i'^2 + 2\ln x}} \tag{3.2.25}$$

The integral can be approximated (within a 1% error) by a function:

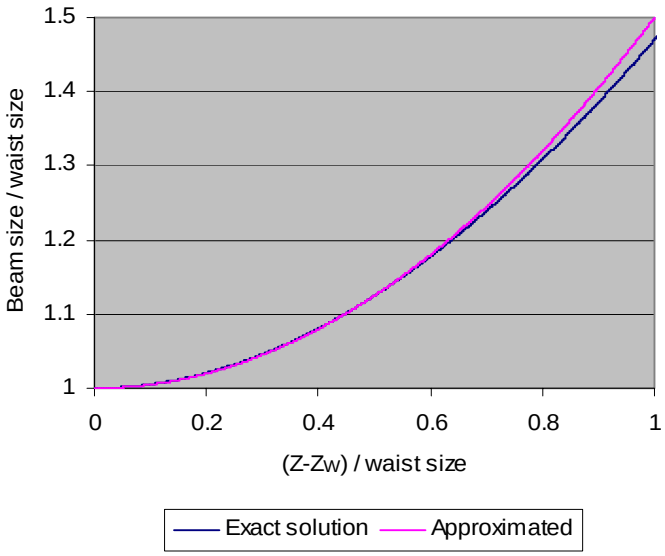

Figure 3.4 Comparison of the exact solution (red line) of the beam size (normalized by the waist size) in drift space as a function of the normalized distance from the waist position (3.2.22) and its approximation (blue dot line, 3.2.23).

$$g(\nu_i') \equiv \int_{e^{-\nu_i'^2/2}}^{1} \frac{dx}{\sqrt{\nu_i'^2 + 2\ln x}} \approx 0.0049487\nu_i'^6 - 0.069182\nu_i'^5 + 0.35548\nu_i'^4 - 0.74171\nu_i'^3 + 0.21824\nu_i'^2 + 0.95449\nu_i' + 0.0019165 \tag{3.2.26}$$

in the range $\nu_i' \le 4$. The beam spot size is:

$$\nu_W = \nu_i e^{-\nu_i'^2/2} \tag{3.2.27}$$

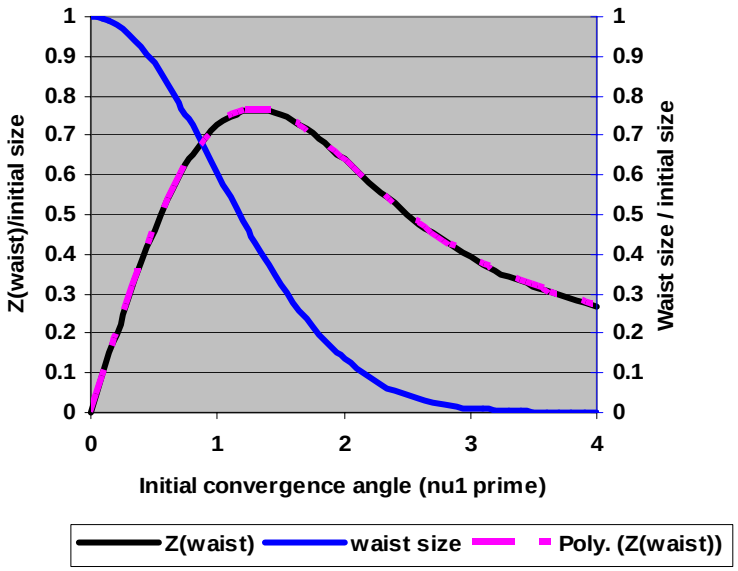

Figure 3.5 Beam waist position (black line), its approximation (red line) and waist spot size (blue line) as a function of initial convergence angle

In general, when the beam enters the drift space from a compact RF gun and solenoid the n-slice phase space can be schematically shown in fig.3.6 with the orientation of the end point line (line A) perpendicular to ν axis.

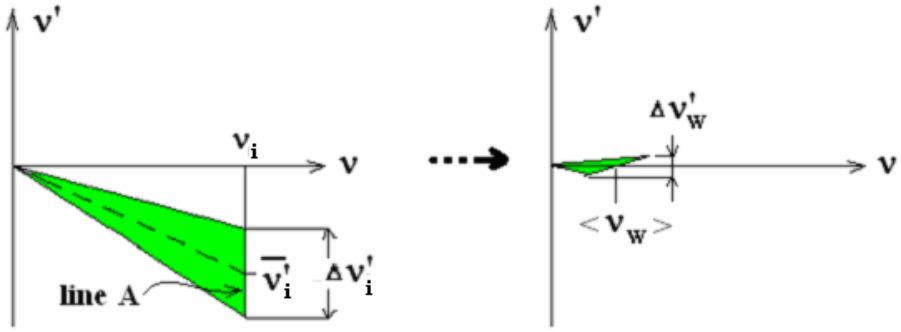

Figure 3.6 Left: The phase space right after the solenoid, the end points of the slice emittances are oriented perpendicular to the ν axis (line A). Right: The phase space near the beam waist.

From equation (3.2.26) one can estimate the spread of z_W caused by a small initial convergence angle spread $\Delta\nu_i'$

$$\begin{aligned}\Delta z_W = \Delta Z_W &\approx \frac{dZ_W}{d\nu_i'}\Delta\nu_i' \\ &\approx \nu_i\left(0.0294\nu_i'^5 - 0.346\nu_i'^4 + 1.422\nu_i'^3 - 2.225\nu_i'^2 + 0.4364\nu_i' + 0.9545\right)\Delta\nu_i'\end{aligned} \tag{3.2.28}$$

The angle spread near the beam waist $\Delta\nu_W'$ can be estimated from equation (3.2.24):

$$\Delta\nu_W' \approx \frac{2\Delta z_W}{\langle \nu_W \rangle} \tag{3.2.29}$$

The emittance at the average beam waist ε_W in (ν, ν') phase space is then:

$$\varepsilon_W \approx \frac{1}{2}\Delta\nu_W'\langle \nu_W \rangle \approx \Delta z_W \tag{3.2.30}$$

Figure 3.7 is the plot of the relative emittance at the beam waist as a function of average initial convergence angle $\overline{\nu_i'}$.

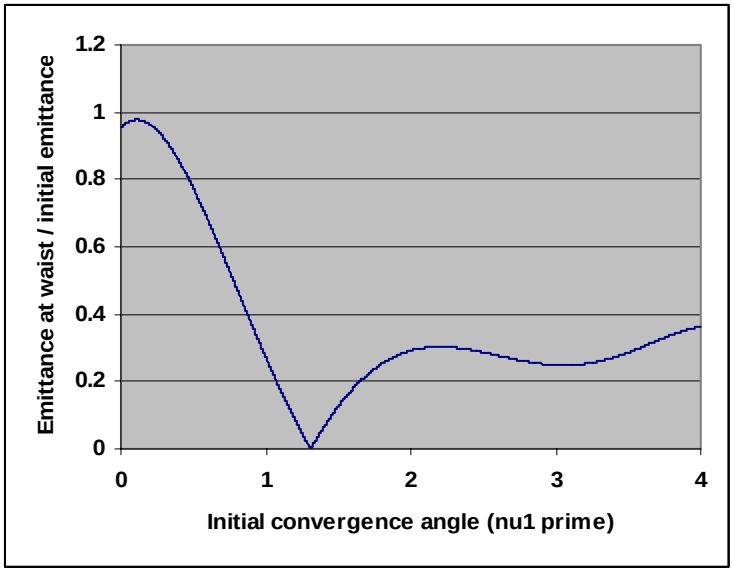

Figure 3.7 The relative emittance at beam waist ($\varepsilon_W / \nu_i \Delta\nu_i'$) as a function of initial convergence angle. Because of the approximation of the waist position spread in equation (3.2.28) the emittance goes to zero. In reality the emittance will not go to zero, but the minimum would be the same position.

One can see that the optimized average initial convergence angle is $\left|\overline{\nu_i'}\right| \approx 1.3$ to have the minimum emittance at the beam waist. In the configuration space the corresponding initial angle, beam waist position and beam waist spot size are

$$\left|\sigma_0'\right| = 1.3\sqrt{P} \approx 0.0244 \frac{\sqrt{Q[nC]}}{\sqrt{\sigma_z[cm]}\gamma^{3/2}} \tag{3.2.31a}$$

$$Z_W[cm] = 0.765\nu_0 \approx 40.6 \frac{\sigma_0[cm]\sqrt{\sigma_z[cm]}\gamma^{3/2}}{\sqrt{Q[nC]}} \tag{3.2.31b}$$

$$\sigma_W = \sigma_0 e^{-\nu_0^2/2} \approx 0.43\sigma_0 \tag{3.2.31c}$$

As an example we assume a Gaussian distributed bunch with a charge of 20nC, a length of σ_z=0.6cm, a radius of σ_0=0.5cm and an energy of 5MeV. From (3.2.31) follows $\left|\sigma_0'\right| \approx 4.0 \times 10^{-3}$, $Z_W \approx 110cm$ and $\sigma_W \approx 0.22cm$.

The condition ($\left|\overline{\nu_i'}\right| \approx 1.3$) is the particular condition where the spread in phase advance is minimized for the initial condition shown in fig.3.6.

One can find the optimized average accelerating gradient γ_L' of the linac by equating the beam size in the waist (3.2.31c) to invariant envelope of the linac entrance (3.2.15):

$$\gamma_L' \approx \frac{2}{0.43}\sqrt{\frac{I}{3I_0\sigma_i^2\gamma}} \approx 7.1\sqrt{\frac{Q[nC]}{\sigma_i^2[cm^2]\sigma_z[cm]\gamma}}[MV/m] \tag{3.2.32}$$

If the orientation of line A is not perpendicular to ν axis (fig.3.8), the solution would be different from equation (3.2.31).

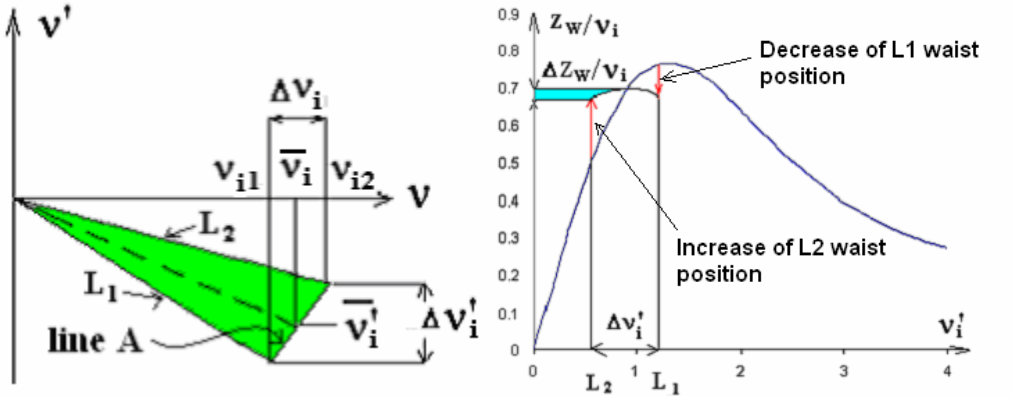

Figure 3.8 Left: The phase space right after the solenoid, the end points of the slice emittances are oriented perpendicular to the ν axis (line A). Right: The phase space near the beam waist.

As shown above the initial coordinates of line elements L_1 and L_2 in phase space are (ν_{i1}, ν'_{i1}) and (ν_{i2}, ν'_{i2}) with $\nu_{i1} < \bar{\nu}_i < \nu_{i2}$ and $\nu'_{i1} > \bar{\nu}'_i > \nu'_{i2}$. Thus we have to minimize the spread in the location of the beam waist resulting from both a beam size and convergence angle spread. From equation (3.2.25) it follows that the waist position is proportional to the initial beam size, i.e., $Z_W \propto \nu_i$. The waist position of line L_1 is in this case is $Z_{W1} = (\nu_{i1} / \bar{\nu}_i) Z^{(0)}_{W1}$ while the waist position of line L_2 is $Z_{W2} = (\nu_{i2} / \bar{\nu}_i) Z^{(0)}_{W2}$ where the superscript (0) represents the value corresponding to the case where the line A is perpendicular to the ν axis (left of fig.3.8). To compensate the variation of Z_w the initial convergence angle $\bar{\nu}'_i$ should be adjusted to the left side of the crest point (right hand plot of fig.3.8) for the case of the initial phase space shown in the left hand plot of fig.3.8.

The change of the waist position induced by the initial beam size difference ($\approx \frac{\Delta\nu_i}{\bar{\nu}_i} Z_W(\bar{\nu}_i, \bar{\nu}_i')$) should be equated to the change caused by the slope difference $\frac{dZ_W(\bar{\nu}_i, \bar{\nu}_i')}{d\bar{\nu}_i'}\Delta\nu_i'$. Therefore

$$\frac{\Delta\nu_0}{\nu_0\Delta\nu_0'} = \frac{d\ln(g(\bar{\nu}_0'))}{d\bar{\nu}_0'}. \qquad (3.2.33)$$

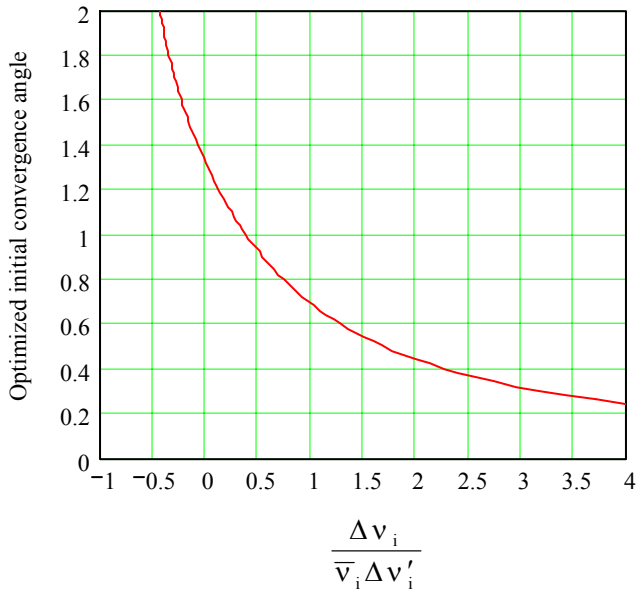

Figure 3.9 Optimized initial average convergence angle ($\bar{\nu}_i'$) as a function of $\frac{\Delta\nu_i}{\bar{\nu}_i\Delta\nu_i'}$ of line A in the left hand plot of fig.3.5.

Fig.3.9 shows the numerical solution of equation 3.2.33. We see that if the slope of line A ($\frac{\Delta\nu_i'}{\Delta\nu_i}$) is positive, then $\frac{\Delta\nu_i}{\bar{\nu}_i\Delta\nu_i'}$ is positive, therefore $\bar{\nu}_0'$ should be smaller than 1.3; if the slope is negative, then $\frac{\Delta\nu_i}{\bar{\nu}_i\Delta\nu_i'}$ is negative and $\bar{\nu}_i'$ will be larger than 1.3. The

solution of equation (3.2.31) is the particular solution of $\Delta\nu_i = 0$. Once $\overline{\nu_i'}$ is found the drift distance and the waist size are obtained from equations (3.2.25) and (3.2.27).

An emittance compensation system for a non-magnetized beam (ignoring chromaticity effects) is schematically shown in fig.3.10. The recipe of designing and optimizing the system is as following:

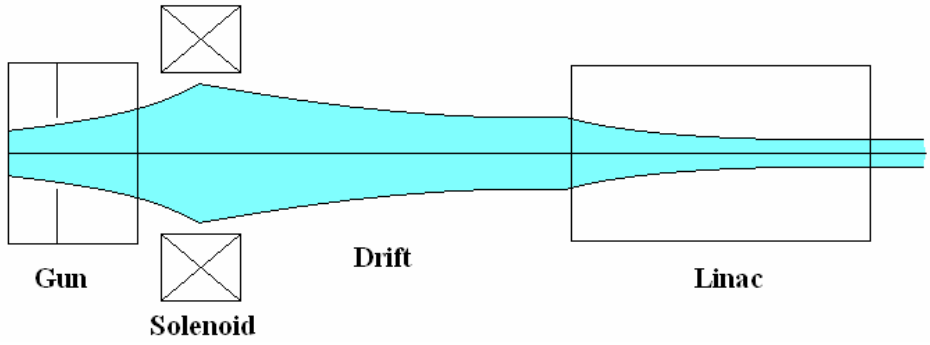

Figure 3.10 Schematic of emittance compensation for a compact RF gun + solenoid + drift + linac system.

- Given the gun's average accelerating gradient γ_G' and the laser pulse bunch length, one can find the current I_{GF} and the energy (γ_{GF}) of the beam at gun exit. Therefore the invariant envelope $\hat{\sigma}_{GF}$ at gun exit can be found from equation (3.2.15): $\hat{\sigma}_{GF} = (2/\gamma_G')\sqrt{I_{GF}/3I_0\gamma_{GF}}$. The spot size on the cathode is roughly $\sigma_c \geq 1.5\hat{\sigma}_{GF}$.
- The cathode has to have a certain degree of recess to compensate the RF defocusing of the 1st half cell gun and the strong space charge kick near the cathode. But it can never completely compensate it and so the beam is always diverging without any external focusing. The recess should as much as is possible without too much loss of field on cathode.

- The solenoid has to be close to the cathode to make the deviation from the invariant envelope of the gun cavity small. Once the above are determined one can easily find out the beam conditions at the location of the solenoid ($\overline{\sigma}_i, \overline{\sigma_i'}, \sigma_z, \overline{\gamma}$) by simulation.
- The length of the drift space from the solenoid to the entrance of the linac can be found from (3.2.31b: $Z_W[\mathrm{cm}] = 0.765\nu_i \approx 40.6\frac{\sigma_i[\mathrm{cm}]\sqrt{\sigma_z[\mathrm{cm}]}\gamma^{3/2}}{\sqrt{Q[\mathrm{nC}]}}$). The initial convergence angle and beam waist spot size can be generally determined by (3.2.31a: $|\sigma_i'| = 1.3\sqrt{P} \approx 0.0244\frac{\sqrt{Q[\mathrm{nC}]}}{\sqrt{\sigma_z[\mathrm{cm}]}\gamma^{3/2}}$) and (3.2.31c: $\sigma_W = \sigma_i e^{-\nu_i'^2/2} \approx 0.43\sigma_i$). If the initial phase space condition is different from the case shown in the left plot of fig.3.6, the initial convergence angle needs to be adjusted according to the curve in fig.3.9, and therefore the drift length and the waist size are determined.
- The linac entrance is at the location of the beam waist. The linac gradient can be adjusted according to equation (3.2.32):

  $$\gamma_L' \approx \frac{2}{0.43}\sqrt{\frac{I}{3I_0\sigma_i^2\gamma}} \approx 7.1\sqrt{\frac{Q[\mathrm{nC}]}{\sigma_i^2[\mathrm{cm}^2]\sigma_z[\mathrm{cm}]\gamma}}[\mathrm{MV/m}])$$

  to match condition (3.2.15) which is the invariant envelope of the linac. The beam at linac exit would be a parallel beam with beam size expressed in equation (3.2.16):

  $$\sigma_f = (2/\gamma')\sqrt{I/3I_0\gamma_f}$$
- With these parameters the emittance is calculated with a tracking code. Since the spot size on cathode was found by an educated guess the emittance is then optimized by varying the spot size and repeating the procedures.

3.3. Chromaticity effect

3.3.1. RF effects on longitudinal phase space distribution

The electron energy at gun exit W_G as a function of initial phase ϕ_0 can be solved numerically. Fig3.10 shows the general characteristics of this function. The crest point (ϕ_M, W_{Max}) on the curve corresponds to the initial phase of maximum acceleration. The curve has the following properties:

- ϕ_M is always less than 90deg. If $\phi_0 > \phi_M$ then W_G decreases faster than if $\phi_0 < \phi_M$.
- Increasing the peak field E_0 in the gun moves the crest point towards higher W_{Max} and higher ϕ_M.
- Reducing the cell length of the gun cavity moves the crest point towards higher value of ϕ_M. A cathode recess moves the point to a lower value of ϕ_M.

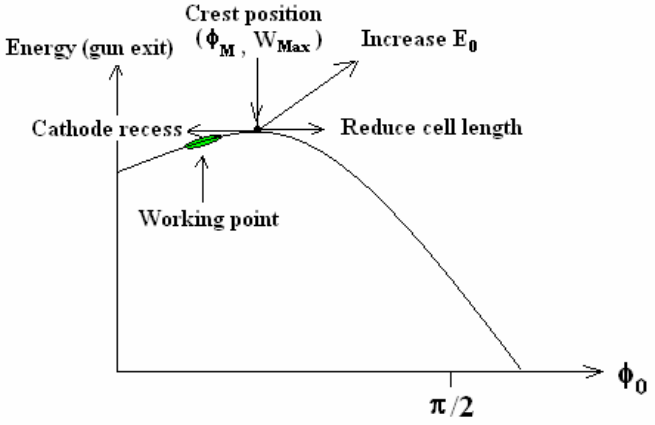

Figure 3.10 Schematic plot of the energy at gun exit as a function of initial phase

The energy spread introduced by space charge increases the energy of the head of the bunch relative to the tail. Thus launching a bunch to the left of ϕ_M minimizes the

resulting energy spread. For a high gradient RF gun (such as a pulsed normal-conducting gun) ϕ_M is relatively high. It is easy to make the launch phase ϕ_0 of the beam smaller than ϕ_M so that the energy spread is minimized. It is typical for such guns, operating at cathode fields of 100 MV/m or more and at low charges of the order of one nanoCoulomb that the energy spread is much less than 1%, and then chromaticity effects can be ignored. However, in a CW gun, even if it is super-conducting, the field gradient is limited so that ϕ_M is low while ϕ_0 must be high to compensate for the lower peak field on the cathode. When these considerations combine with a high bunch charge, we face a situation where the energy spread of the bunch at the CW gun exit is significant. Under these conditions, space charge forces dominate, and the particles in the front of the bunch have higher energy than those in the rear.

As discussed before, it is desired to have some cathode recess to have better emittance compensation. Since, as mentioned above, the field gradient is limited and thus the only way to move ϕ_M to a higher value is to reduce the cell length.

Fig.3.11 shows the longitudinal phase space of a 703.5MHz 1½ cell super-conducting RF gun at gun exit with $\phi_0 = 30\,\mathrm{deg}.$ and $\phi_0 = 60\,\mathrm{deg}.$. The gun shape and field distribution are shown in details in section 5. The charge/bunch is 5nC, the laser on cathode has a transverse uniform distribution with 5mm maximum radius and a longitudinal Gaussian distribution with sigma of 15.8ps bunch length, the peak field on axis is 28MV/m. The energy spread at $\phi_0 = 30\,\mathrm{deg}.$ is much less (rms of 0.42%) than that of $\phi_0 = 60\,\mathrm{deg}.$ (rms of 2.86%).

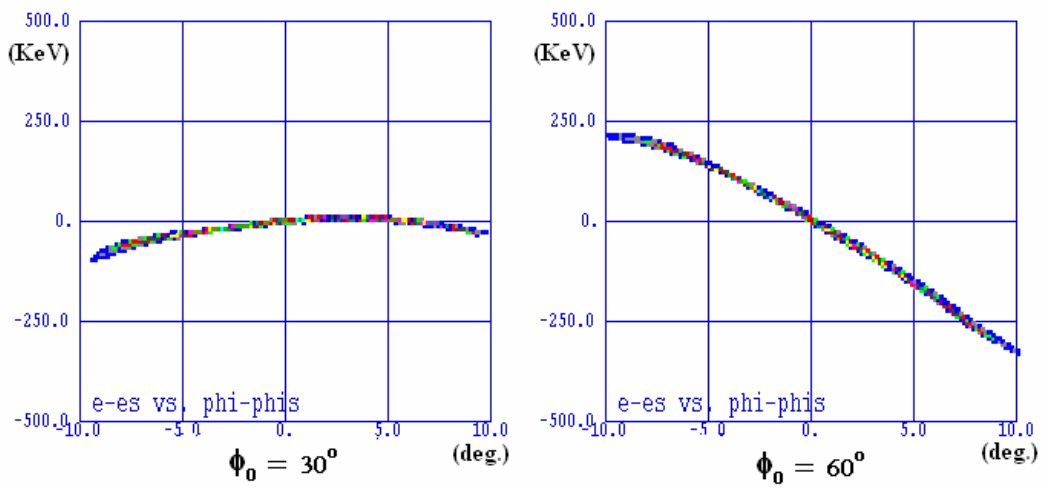

Figure 3.11 Longitudinal phase space at gun exit for $\phi_0 = 30\,\text{deg.}$ (left) and $\phi_0 = 60\,\text{deg.}$ (right)

3.3.2. RF effects on transverse phase space distribution

The phase space angle of a slice (σ'/σ) at the exit of the gun cavity is given approximately by [12]:

$$\theta \approx \alpha k \sin\phi \qquad (3.3.1)$$

where ϕ is the RF phase at the exit of the cavity, α and k are defined in section 1. ϕ is generally close to 90° and the bunch length $\Delta\phi$ is usually small, therefore we may ignore the time dependent RF defocusing. This can be seen in the following simulation result.

Fig.3.12 shows the phase spaces of 9 slices at the exit of the cavity for the launch phase $\phi_0 = 60\,\text{deg.}$ case. Slice #1 (front) and slice #9 (rear) have similar space charge forces. Despite of their large energy difference, their phase space angles are quite close. The large phase space angle difference between the edge slices (#1, #9) and middle slices (#4, #5 and #6) is due to the difference in space charge. Thus, as we observed above, the

slice emittance at this gun's exit is dominated by the dependence of space charge on the slice position and not on the time dependent RF force.

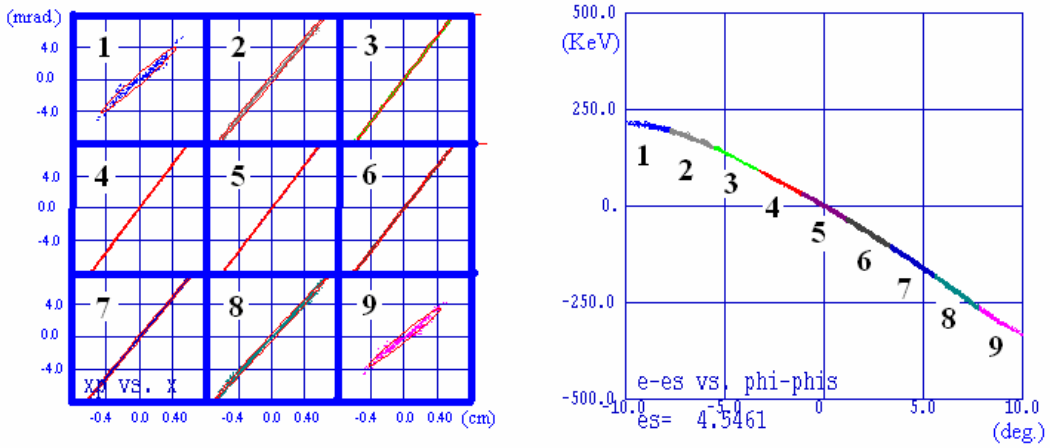

Figure 3.12 Transverse slice phase spaces (left) and longitudinal slice phase space (right) at the gun exit of the example in section 5 with $\phi_0 = 60\,\text{deg}$.. Slice #1 is the front slice and slice #9 is the rear slice.

3.3.3. The chromaticity in the solenoid and drift space

The solenoid focusing kick ($F_S = \left(\frac{qB}{2mc\beta\gamma}\right)^2$) is proportional to $1/\gamma^2$. As the beam is strongly converging at solenoid's exit, the solenoid's contribution to the chromaticity is significant as long as the energy spread at the solenoid is not negligible. The particles with higher energy (front particles) experience less focusing than those with lower energy (rear particles)

Fig.3.13 is the phase space after the solenoid exit of the previous example. One can see that the solenoid chromaticity can not be neglected in this case. In fact, the emittance at the solenoid exit increases from 21.6mm.mr to 28.3mm.mr in the $\phi_0 = 60\,\text{deg}$ example

due to the solenoid chromaticity while the increase for the $\phi_0 = 30\,\mathrm{deg}$ is only from 12.3mm.mr to 12.4mm.mr.

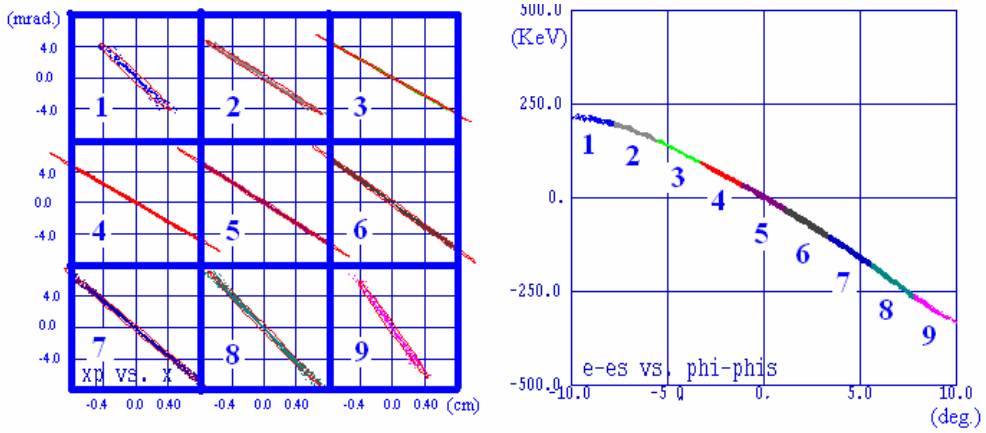

Figure 3.13 Phase space at the solenoid exit

In the drift space, $\nu(z) \equiv \sigma(z)/\sqrt{P} \propto \gamma^{3/2}$, so the ν_0 is larger for higher energy particles and vice versa for lower energy particles. This spreading effect is similar to the case presented above and shown in fig. 3.8. Therefore, as discussed above, $\overline{\nu_0'}$ has to be smaller than 1.3 for an optimized emittance compensation.

It should be noted that the space charge induced energy spread, acting through the chromaticity, adds to the transverse effects of the space charge to make the difference between slices larger. This increases the spread of the slice waist positions and therefore degrades the emittance compensation. This explains why in the previous simulations [13] and experiments [14] the optimized initial phase is always smaller than in theory when the theory ignored the chromaticity.

3.3.4. The linac entrance chromaticity

One must also consider the chromaticity of the focusing of the linac entrance. The RF focusing kick is $\theta = \sigma' / \sigma = -\gamma'_L / 2\gamma$ where γ'_L is the linac average accelerating gradient. Lower energy particles get a larger kick angle than the higher energy particles. The matching condition for a linac is that the beam must be parallel at the linac entrance. In order to compensate this chromaticity, one can require that the medium energy particles be parallel while the lower energy particles have a divergence angle (over focused) and the higher energy particles have a convergence angle (less focused) just before the linac entrance (fig.3.14). This will lead to the location of the beam waist of the whole beam envelope, which is determined by the location of the earliest beam waist, to be in front of the linac entrance.

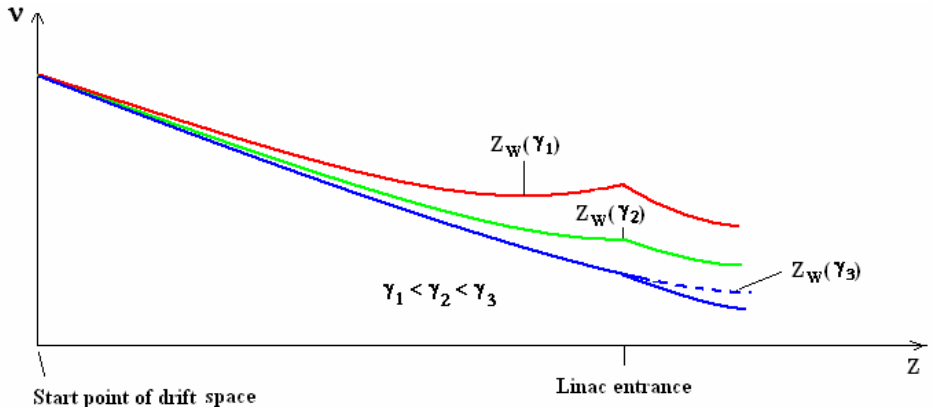

Figure 3.14 Schematic plot of the chromaticity in drift space. The smaller energy slice has earlier waist position and larger beam size. The higher energy slice has later waist position and smaller beam size

The phase space just before linac entrance and after linac entrance is schematically shown in fig.3.15.

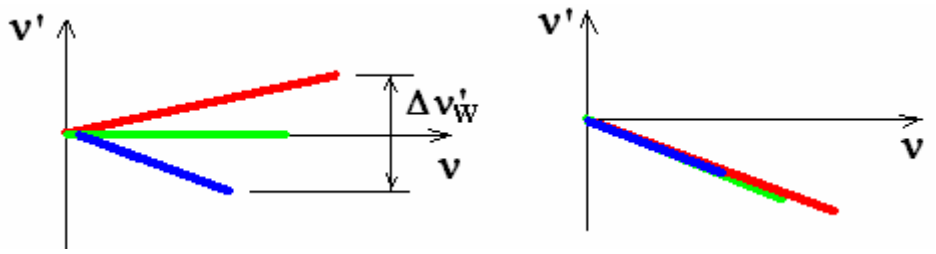

Figure 3.15 The phase spaces just before (left) and after (right) linac entrance. The lines with different colors represent the slices with the same colors shown in fig.3.14

For an estimation of the of $\Delta\nu'_{WD}$ in the drift space induced by the chromaticity we use the simplification that the slices have the same ν_i and the same ν'_i. From equation (3.2.29) we get:

$$\Delta\nu'_{WD} \approx \frac{2\Delta z_W}{\bar{\nu}_W} \approx \frac{2g(\nu')}{\bar{\nu}_W}\frac{d\nu_i(\gamma)}{d\gamma}\Delta\gamma = \frac{5.3\Delta\gamma}{\gamma} \tag{3.3.2}$$

The linac entrance gives the variation $\Delta\nu'_{WL}$ caused by the chromaticity:

$$\Delta\nu'_{WL} \approx \frac{d(-\gamma'_L/2\gamma)}{d\gamma}\Delta\gamma\bar{\nu}_W = \frac{\gamma'_L}{2\gamma}\frac{\Delta\gamma}{\gamma}\bar{\nu}_W \tag{3.3.3}$$

$\Delta\nu'_{WD}$ should be made equal to $\Delta\nu'_{WL}$ to obtain the minimum chromatic effect. Therefore:

$$\gamma'_L = \frac{10.6\gamma}{\bar{\nu}_W} \approx \frac{10.6\gamma}{0.43\nu_i} = \frac{10.6}{0.43}\sqrt{\frac{I}{2I_0\sigma_i^2\gamma}} \approx 46.3\sqrt{\frac{Q}{\sigma_i^2\sigma_z\gamma}} \tag{3.3.4}$$

where Q is the charge of the bunch in nC, σ_i and σ_z are the beam size and bunch length in cm.

The equations (3.2.32) and (3.3.4) can not be fulfilled simultaneously. The applied solution must be a compromise between the two. A higher energy spread will require a larger γ'_L.

CHAPTER 4. EMITTANCE COMPENSATION FOR A MAGNETIZATION AND THE SPACE-CHARGE-DOMINATED BEAM

4.1. Emittance of a magnetized beam

The magnetization term $\mathcal{M}$ introduces not only the beam's radial motion but also its angular motion. As mentioned in section 3.1, $\mathcal{M}$ is equivalent to the normalized emittance term ε_n in the envelope equation (3.1.1). In a field free region $\mathcal{M}$ behaves like ε_n and can be converted to beam's temperature in lab frame (T_{Lab}). When the beam enters a solenoid field with

$$B\sigma^2 = B_S\sigma_S^2, \qquad (4.1.1)$$

and if all slices match the condition (4.1.1) the contribution of $\mathcal{M}$ to T_{Lab} disappears. B is the solenoid longitudinal field and σ is the beam size at the solenoid entrance. If equation (4.1.1) is only valid for the average over all slices then part of $\mathcal{M}$ contributes to T_{Lab}. For the electron-cooling application T_{Lab} in the cooling solenoid is what we are really interested in. We define the emittance for a magnetized beam (ε_M) as the emittance measured in the frame rotating with an average rotation speed (the <ω> frame). ε_M is actually the emittance (or velocity spread) in lab frame with solenoid field given by equation (4.1.1). ε_M is determined by the radial motion emittance ε_R and the angular motion emittance ε_θ:

$$\varepsilon_M = \sqrt{\varepsilon_{R'}^2 + \varepsilon_\theta^2} = \sqrt{\varepsilon_{MX}^2 + \varepsilon_{MY}^2} \qquad (4.1.2)$$

where ε_{MX} and ε_{MY} are the horizontal and vertical emittance in lab frame under the rms matching of the condition (4.1.1).

To illustrate the meaning of ε_M, we consider a beam which has the ζ-r rectangular profile (beer can shape) on the cathode shown in fig.4.1.(a) and its distribution evolves to a shape that is shown in fig.4.1.(b) due to space charge and time dependent fields. Each slice has the same magnetization, or the same canonical angular momentum. Thus, as discussed above, the slices will have some relative angular rotation in the <ω> frame shown in fig.4.1.(c). Since a rotating beam is an ellipse in phase space, ignoring the radial motion, the phase-space distribution of the whole beam has the shape shown in fig.4.1.(d) in the <ω> frame. The total area becomes quite large. We call this emittance the slice angular emittance ε_θ and it is dependent on the relative radii difference.

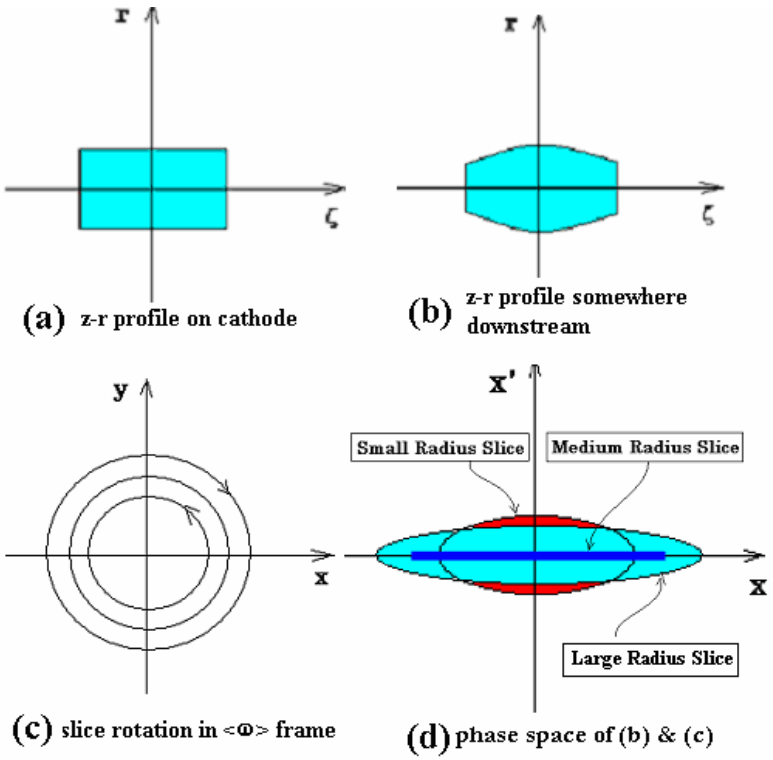

Figure 4.1 (a): ζ-r profile on cathode. The transverse and longitudinal distributions are assumed to be uniform; (b): ζ-r profile following some transport. The change in shape is caused by time dependent RF force on the slices. (c): Configuration space plot showing the relative rotation between slices in the <ω> frame. The beam rotates counterclockwise in a field-free region. (d): Phase space in the <ω> frame ignoring r direction motion. The rotation of a beam with a small or large radius is elliptical in phase space. The RMS area of this phase space is the emittance, ε_θ

To show the dependence of ε_θ as a function of relative radius change consider the beam ζ-r shape to be distorted to a shape characterized by following: r linearly increases from $r_{\min} = (1-\Delta_R)\bar{r}$ to $r_{\max} = (1+\Delta_R)\bar{r}$, where $\bar{r}$ is the average radius and $0 \le \Delta_R \le 1$ indicates the degree of relative radii difference. It can be shown that the angular emittance, ε_θ, as a function of Δ_R is

$$\varepsilon_{\theta N} = \beta\gamma\sqrt{\langle x'^2\rangle\langle x^2\rangle - \langle xx'\rangle^2} = \frac{\mathcal{M}}{2}\sqrt{\Delta_R^4/9 - 1 + (1+\Delta_R^2/3)/(1-\Delta_R^2)} \qquad (4.1.3)$$

where $\varepsilon_{\theta N}$ is the normalized angular emittance. Fig.8. shows $\varepsilon_{\theta N}/\mathcal{M}$ as a function of Δ_R. $\varepsilon_{\theta N}$ is about 34% of the magnetization M when Δ_R is 0.5.

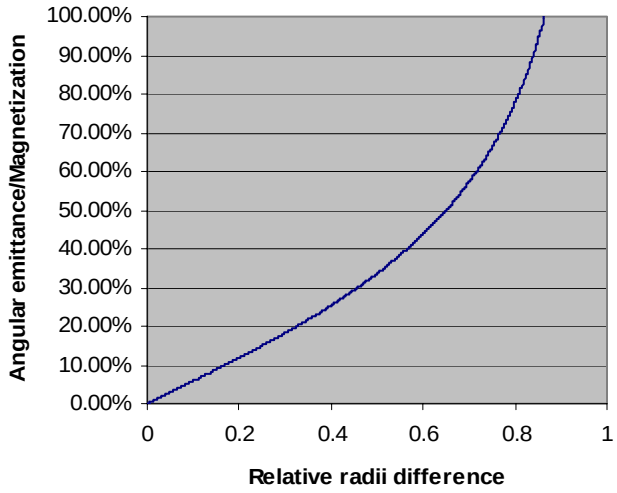

Figure 4.2 The emittance introduced by the relative slice rotation ε_θ as a function of relative radii change Δ_R

$\varepsilon_{\theta N}$ can be a big number if the magnetization $\mathcal{M}$ is large. The only way to reduce $\varepsilon_{\theta N}$ is to reduce the Δ_R of the beam.

4.2. Emittance compensation of a magnetized beam

Lets first study property of a magnetization dominated beam in a linear focusing channel without chromaticity effect. The envelope equation becomes

$$\sigma'' + \sigma' \frac{\gamma'}{\beta^2 \gamma} + K_r \sigma - \left(\frac{\mathcal{M}}{\beta\gamma} \right)^2 \frac{1}{\sigma^3} = 0 \ . \qquad (4.2.1)$$

Because of the Liouvillian nature of the perturbed envelope system, one can prove that the emittance $\varepsilon_M = \sqrt{\varepsilon_{R'}^2 + \varepsilon_\theta^2} = \sqrt{\varepsilon_{MX}^2 + \varepsilon_{MY}^2} = const.$.

One can view this point in the following way. Assuming the initial conditions are the same for all slices, i.e., $\mathcal{M}(\zeta) = const.$, $\sigma_0(\zeta) = \sigma_0 = const.$ and $\sigma_0'(\zeta) = \sigma_0' = const.$ so that $\varepsilon_M(z=0) = 0$, then $\sigma(z,\zeta) = \sigma(z) = const.$ and $\sigma'(z,\zeta) = \sigma'(z) = const.$ therefore $\varepsilon_M(z) = \varepsilon_M(z=0) = 0$. If $\sigma_0(\zeta) \neq const.$ or $\sigma_0'(\zeta) \neq const.$ so that $\varepsilon_M(z=0) \neq 0$, the envelope equation can be expressed as:

$$\sigma'' + \sigma' \frac{\gamma'}{\beta^2\gamma} + K_r\sigma - \left(\frac{\mathcal{M}}{\beta\gamma}\right)^2 \frac{1}{\sigma^3} - \left(\frac{\varepsilon_M(z=0)}{\beta\gamma}\right)^2 \frac{1}{\sigma^3} = 0 \qquad (4.2.2)$$

$\varepsilon_M(z=0)$ can be thought as thermal emittance of the beam and so is a constant. This means that if the beam is magnetization dominated, then there is no ε_M compensation in a linear system.

The existence of magnetization degrades the effect of emittance compensation. The degree of the degradation is determined by the ratio ($R_{M/K}$) between the magnetization term $\left(\frac{\mathcal{M}}{\beta\gamma}\right)^2 \frac{1}{\sigma^3}$ and the space charge term $\frac{K_s(\zeta)}{\beta^3\gamma^3\sigma(\zeta)}$:

$$R_{M/K} = \sqrt{\frac{\beta\gamma}{K_S}} \frac{\mathcal{M}}{\sigma}. \qquad (4.2.3)$$

If $R_{M/K} >> 1$, the emittance compensation vanishes. As long as $R_{M/K}$ is small, the angular motion is depressed, the space charge force and chromaticity convert mostly to radial motion like for the non-magnetized, which allows emittance compensation. For a beam with large $\mathcal{M}$ one can increase the beam size to decrease $R_{M/K}$ so that the beam behaves like a non-magnetized, space charge dominated beam with:

$$\sigma > \sigma_M = \mathcal{M}\sqrt{\beta\gamma / K_S}. \qquad (4.2.4)$$

As an example consider the RHIC e-cooling project where $B_S = 360G$ and $\sigma_S = 0.6cm$ so that $\mathcal{M} = 380\mu m$, $\beta\gamma \approx 10$ before linac, Charge is $Q = 20nC$ and bunch length is $\sigma_z \approx 0.6cm$, so $\sigma_M = \mathcal{M}\sqrt{\beta\gamma / K_S} = \mathcal{M}\sqrt{2\sqrt{2\pi}\beta\gamma I_0 \sigma_z / Qc} \approx 1.1cm$. The beam size should be less or comparable to this value.

One can also see from (4.2.3) that the emittance compensation is only effective in low energy range.

4.3. The chromaticity effect

As long as $R_{M/K}$ is small, the angular motion is depressed and the previous discussion of chromaticity effect for non-magnetized beam is valid, i.e., the beam waist be in front of linac entrance.

In the case of a low gun field the energy spread may be very big due to the strong space charge force and so the chromaticity effect is dominating. Therefore the matching of the chromaticity generated by the linac entrance focusing becomes more important, i.e., the beam waist must be far in front of linac entrance. One can reduce the energy spread by adjusting the initial phase to reduce this effect.

In summary, a magnetized beam degrades the emittance ε_M compensation; the beam size must be comparable to σ_M to have some ε_M compensation; matching the linac entrance chromaticity may dominate the emittance compensation for low gun field case.

CHAPTER 5. SIMULATION OF THE RHIC ELECTRON-COOLER INJECTOR

5.1. The cavities.

With the beam's very high repetition frequency (9.4MHz), the RF gun must work in a continuous mode. A 1½ cell 703.5MHz superconducting RF gun is used to enhance the accelerating efficiency of the gun. The cathode is recessed to have RF focusing near cathode and therefore the peak field on cathode E_c is decreased.

The accelerating peak field on axis E_0 is determined by 2 factors: first, the electron power under E_0 at gun exit should be less than the RF source power (1MW) due to the transmission loss and wake field effect. Second, The peak voltage E_0 should below the superconductor RF cavity quenching limit (E_0 less than 50MV/m on axis) [15]. A ½ cell cavity would require a field above the quenching limit. A 1½ cell cavity with $E_0 = 30MV/m$ provides a beam energy of 4.7MeV. With a charge per bunch of 20nC the beam power is $20nC \times 9.4MHz \times 4.7MeW = 0.88MW$, which is just below the RF source power. A cavity with more cells would make E_0 too small. This is why we choose 1½ cell cavity as the gun cavity. The cavity shape and its field lines are shown in fig.5.1. The field along axis is shown in fig.5.2. The PARMELA code is used for the beam dynamic simulations. The beam energy at gun exit as a function of initial phase is shown in fig.5.3.

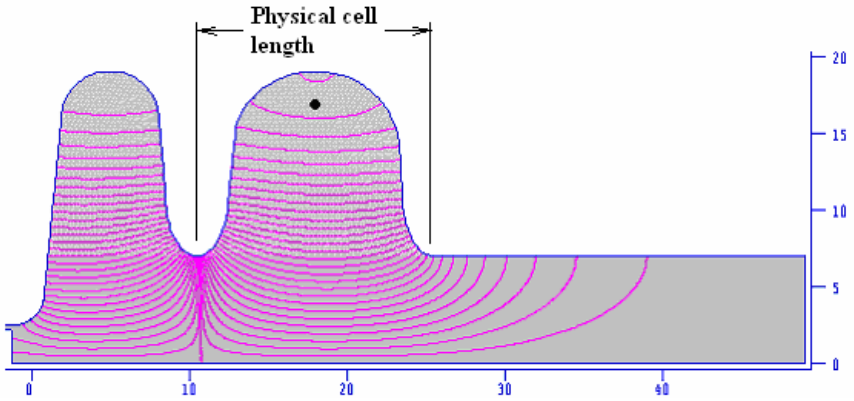

Figure 5.1 1½ cell RF gun cavity, calculated with SUPERFISH.

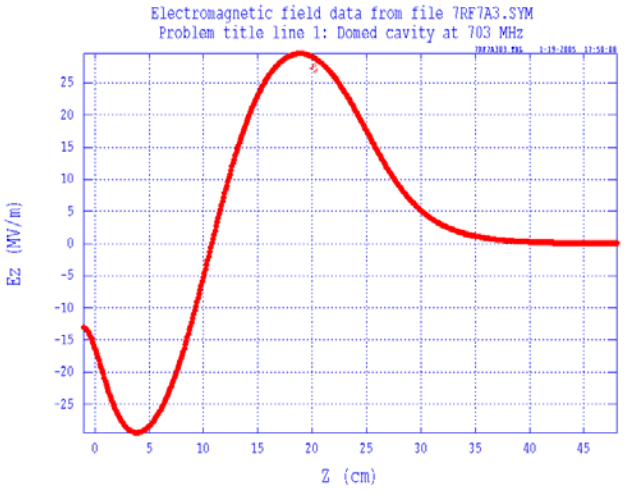

Figure 5.2 Field strength on axis of the RF gun

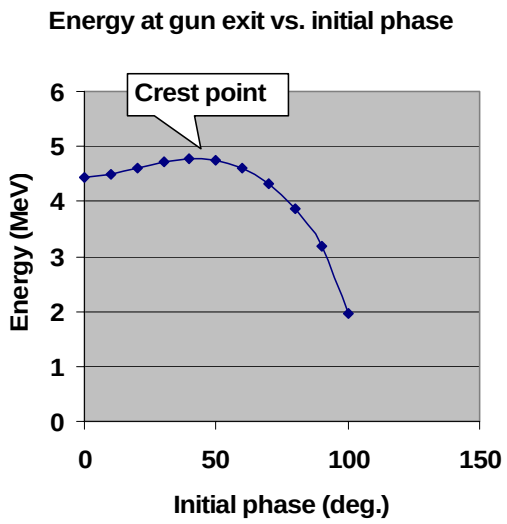

Figure 5.3 Electron energy as a function of initial phase

The initial phase must be before the crest point of the curve to have small energy spread at gun exit. The small energy spread is more important when there are bend magnets in the system.

For use with a Secondary Emission Diamond Cathode (see chapter 6) it is necessary to make the initial phase high enough, but the recess of cathode makes the crest move to smaller values. One can make the cell length of the gun shorter to compensate the cathode recess effect. This is why the full cell length in fig.5.1 is less than $\lambda_{RF} / 2 \approx 21cm$.

The linacs are 5-cell superconducting cavities. The geometry and field distribution are shown in fig.5.4.

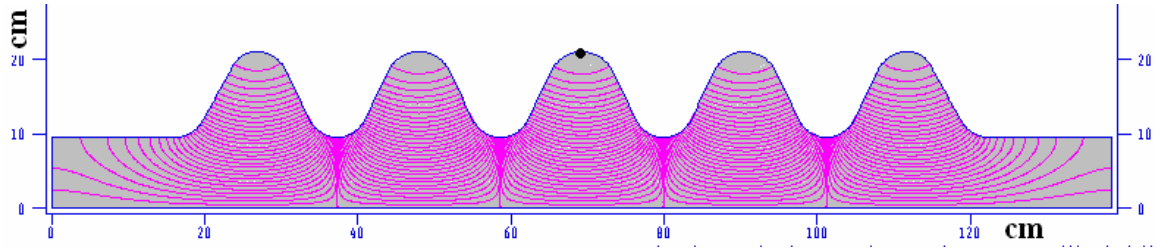

Figure 5.4 Geometry of the 5-cell linac cavity and its field lines

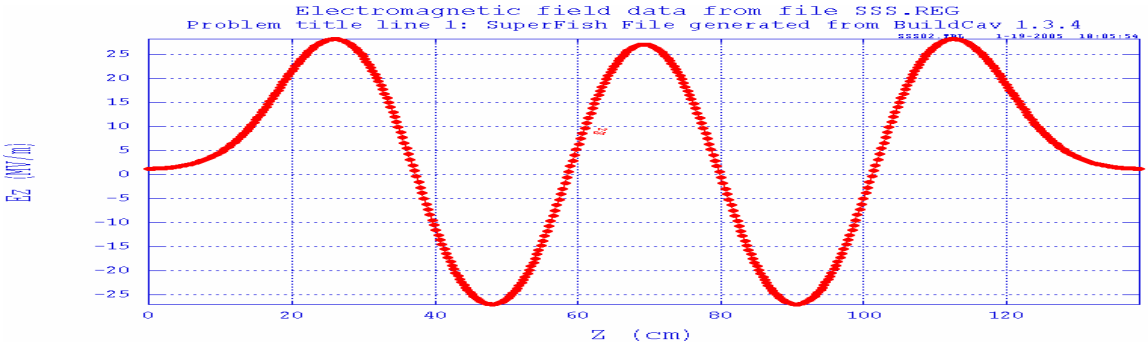

Figure 5.5 Field strength on axis of the 5-cell linac cavity

5.2 Simulation of a non-magnetized beam in a straight line

The beam should have a charge of 20nC per bunch. The distribution is uniform on transverse with spot size on cathode $\sigma_c = 0.6cm$ and Gaussian in longitudinal with $\sigma_L[\text{deg.}] = 4\,\text{deg.}$

Using equation (3.2.15) the spot size on cathode is:

$$\sigma_c = (2/\gamma')\sqrt{I/3I_0\gamma_i} \approx 0.65cm \qquad (5.2.1)$$

where $\gamma' = 30$ is the accelerating gradient in the gun. At the solenoid exit the rms spot size σ_0 is about 0.45cm, the beam energy is about 5 MeV (γ=10) and the bunch length

σ_z is about 0.6cm. From equation (3.2.31) the optimized beam waist position and the beam waist spot size are:

$$Z_W[cm] \approx 40.6 \frac{\sigma_0[cm]\sqrt{\sigma_z[cm]}\gamma^{3/2}}{\sqrt{Q[nC]}} \approx 100cm \qquad (5.2.2a)$$

$$\sigma_W \approx 0.43\sigma_0 \approx 0.2cm \qquad (5.2.2b)$$

The beam size matching condition for the linac is

$$\sigma_c = (2/\gamma')\sqrt{I/3I_0\gamma_i} \approx 0.2cm\,. \qquad (5.2.3)$$

Figure 5.6 shows the envelope as a function of position for the optimized case for this non-magnetized beam where the initial phase is 30degrees. The beam waist position is approximately 100cm after the solenoid with waist size 0.25cm. The linac entrance is located far behind the beam waist and the spot size at linac entrance is 0.3cm.

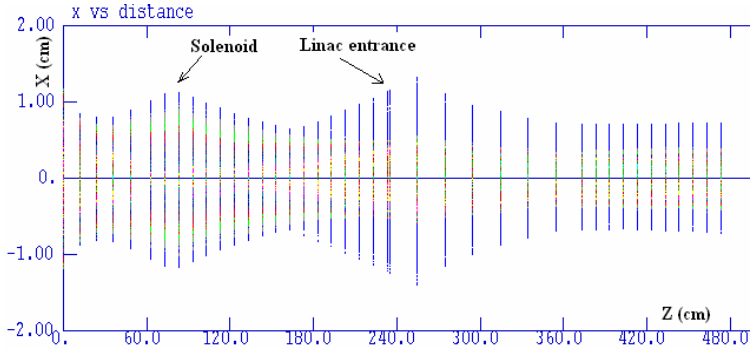

Figure 5.6 Beam envelope vs. z of an optimized non-magnetized beam

This position of linac entrance past the waist and the induced mismatch of linac matching condition are due to the large energy spread of the beam at linac entrance (rms of 1.87% at initial phase of 30deg.).

Fig.5.7 is the emittance as a function of path length. The big reduction of emittance from linac entrance to linac exit indicates the importance of matching of the linac entrance chromaticity effect. The final emittance is 17mm.mr for this case.

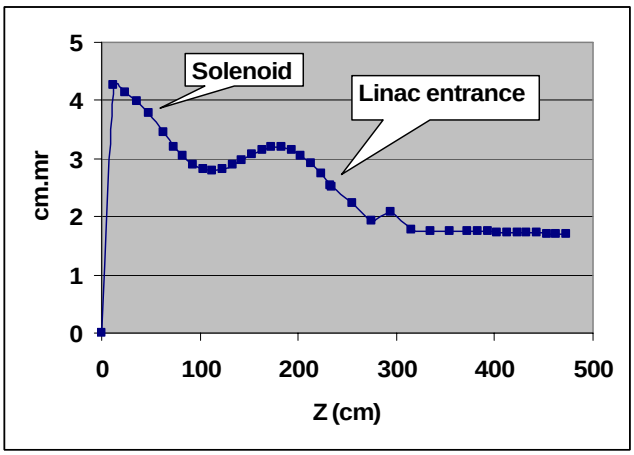

Figure 5.7 Emittance vs. z of the optimized non-magnetized beam

5.3. Magnetized beam in the straight line

Once the beam is strongly magnetized ($B_S \times \sigma_S^2 = 500G \times (10mm)^2$) the beam size at gun exit is much bigger ($\sigma_X = 1.2cm$) and is close to $\sigma_M = 1.1cm$. The beam convergence angle should be small to avoid a small beam size. A larger beam size also increases the distance of the beam waist.

Fig.5.8 shows the beam envelope and emittance as a function of distance for the optimized case of a magnetized beam in a straight transport line.

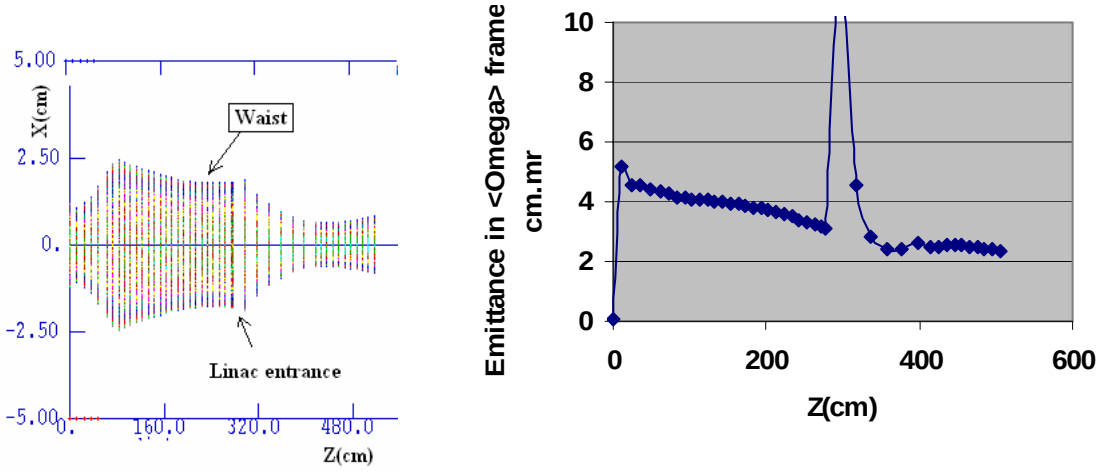

Figure 5.8 Envelope vs. z (left) and ε_M vs. z (right) for an optimized magnetized beam in a straight line. The magnetization $\mathcal{M} = 380mm.mr$. Initial phase=30deg.

One can see that:

1. The beam waist size ($\sigma = 0.91cm$) is much bigger than for a non-magnetized beam (0.25cm).
2. The linac entrance is positioned closer to the waist due to less energy spread (rms. of 1.1%).
3. The ε_M compensation is less efficient (final ε_M is 24mm.mr) compared to the normal non-magnetized beam (ε_x =17mm.mr).
4. Like in the non-magnetized beam case, ε_M has a big decrease from linac entrance to linac exit, which indicates the importance of the chromaticity matching of the linac entrance focusing.

The spikes in the curve are caused by the transient time dependent RF focusing on a bunched beam.

The matching of the linac entrance focusing is more important for large energy spread beam. As an example we show the beam envelope vs. z and ε_M vs. z of the straight transport line with an initial phase of 45deg. (fig.5.9) and an energy spread at linac entrance is 2.91%. The solenoid causes a large emittance increases due to the chromaticity effect. The linac entrance is even further post positioned. The decrease of ε_M from linac entrance to the exit is more pronounced.

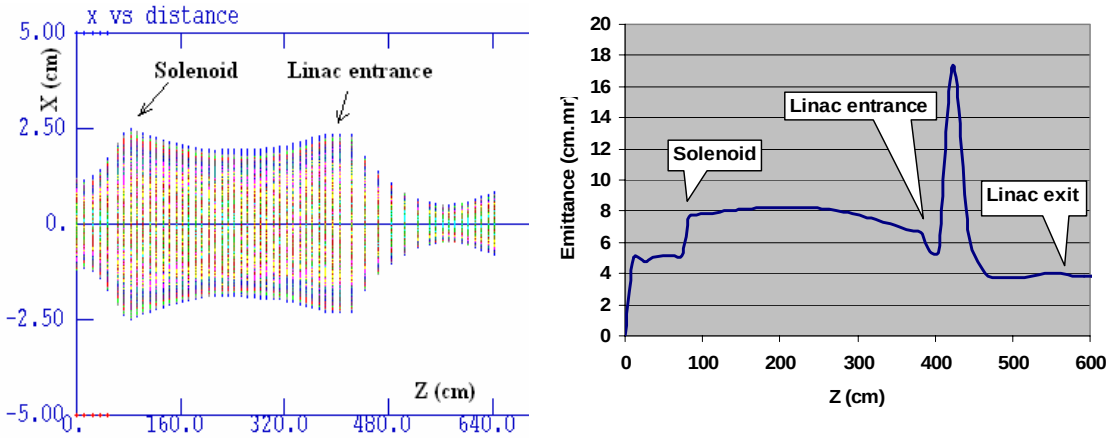

Figure 5.9 Envelope vs. z (left) & ε_M vs. z (right) of the magnetized beam ($\mathcal{M} = 380mm.mr$) with initial phase $\phi_i = 45\,\mathrm{deg}.$. The energy spread at linac entrance is rms 2.91%

5.4. Simulation of RHIC e-cooling injector and the Z-bend system

As shown in fig.5.10, the lower energy beam from gun must merge with recovered higher energy beam. A "Z-bend" system is used for this purpose. This system has the feature that the effect of the linear increase of energy spread during the system is well

compensated [16]. The magnets in the system are the chevron magnets (leading and trailing edge angles are equal to ¼ of bend angle) so that the beam has equal focusing on both x and y direction. In this sense one can approximate the bend magnets as solenoids. The system from cathode to linac exit is shown in fig.5.10.

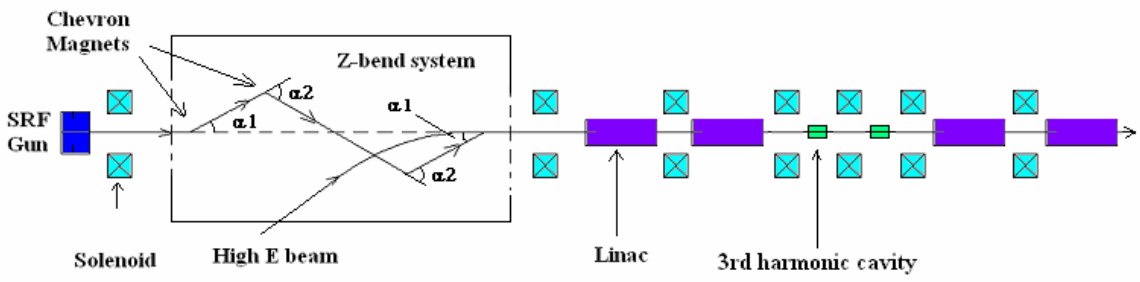

Figure 5.10 RHIC e-cooling injector and the Z-bend system. In principle the z-bend system is symmetric to the center point to have well compensation of the linear energy spread increase effect during the transport

Some parameters for the optimized case are listed in table 5.1:

Table 5.1: Parameters of the optimized case of RHIC magnetized beam cooling

Charge	20nC
Radius (Transverse uniform distribution)	12mm
Magnetization	380mm.mr
Sigma z (Longitudinal Gaussian distribution)	4degrees, 16ps
Maximum field on axis of gun cavity	30MV/m
Initial phase	30deg.
Energy at gun exit	4.7MeV
Energy spread at gun exit	rms 1.87%
Bend angle α_1 ($\alpha_1 = \alpha_2 / 2$)	10degrees

Energy at linac exit	55MeV
Final emittance ε_M	35mm.mr
Final longitudinal emittance	100deg.keV

Fig. 5.11 shows the beam envelope vs. z and fig.5.12 shows the emittance ε_M vs. z for the optimized case of the RHIC e-cooling injector.

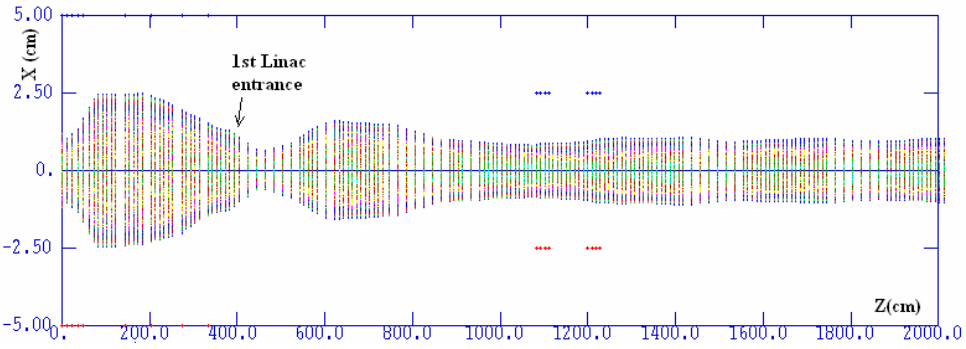

Figure 5.11 Envelope vs. z of RHIC e-cooling system. The strong edge focusing of the chevron magnets makes the beam size much smaller than $\sigma_M \approx 1.1cm$. This is one reason that ε_M is less compensated

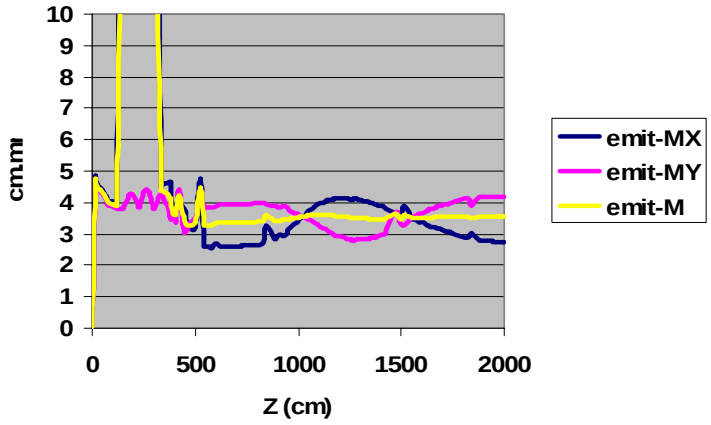

Figure 5.12 ε_M vs. z of RHIC e-cooling injector. The original big spikes at linac entrances and exits are removed from the picture. Because of the asymmetry of the system $\varepsilon_{MX} \neq \varepsilon_{MY}$ after the Z-bend system but the transverse emittance $\varepsilon_M = \sqrt{\left(\varepsilon_{MX}^2 + \varepsilon_{MY}^2\right)/2}$ is a constant and is comparable to the transverse emittance of a non-magnetized beam

One can see that:

1. The ε_M compensation is even less efficient in the "Z-bend" system.
2. After the 1st linac exit (z>5m), ε_{MX} and ε_{MY} oscillate around ε_M due to the strong coupling between x-direction and y-direction motion caused by the strong magnetization. ε_M is almost a constant after the 1st linac exit. The final emittance is about 35mm.mr.

As the charge is very high, the energy spread is very high. The ε_M of the "Z-bend" system is even more sensitive to the energy spread due to the achromatic imperfection. Fig.5.13 (left) shows ε_M as a function of initial phase of a straight transport line and for "Z-bend" system. The energy spreads are shown in fig.5.13 (right).

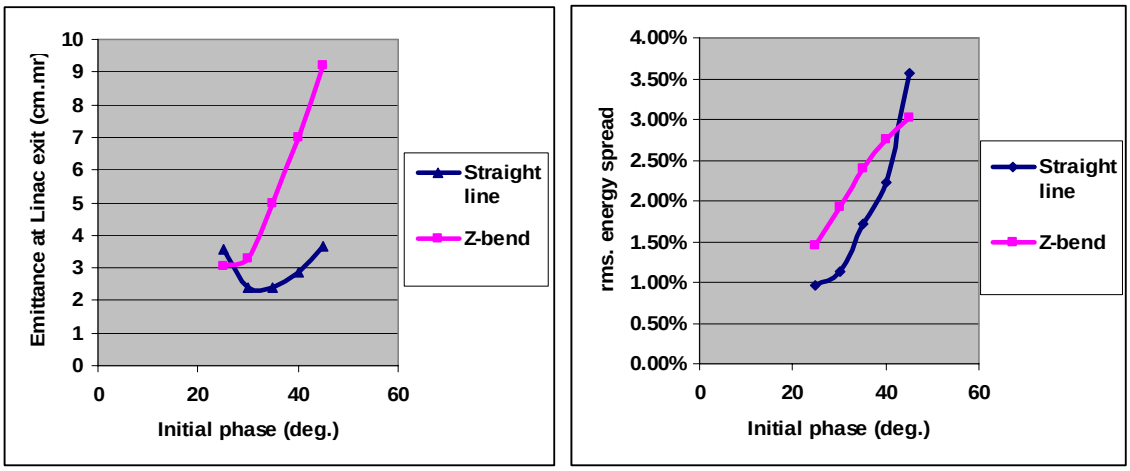

Figure 5.13 ε_M of a straight transport line (blue) & ε_M of a Z-bend transport line (red) as a function of initial phase (left) and their corresponding energy spread (right)

By using the self-consistent distribution (see section 3.1) on the cathode the space charge induced slice emittance is removed and the emittance is expected to be smaller than that of the regular longitudinal Gaussian and transverse uniform distribution bunch. Fig.5.14 is the optimized emittance vs. z curve for the Z-bend system with the ellipsoid distribution bunch on cathode. The final emittance at linac exit is 31.8mm.mr and is very close to that for the regular distribution. This clearly indicates that the emittance is dominated by the chromaticity effect and the time dependent RF effect.

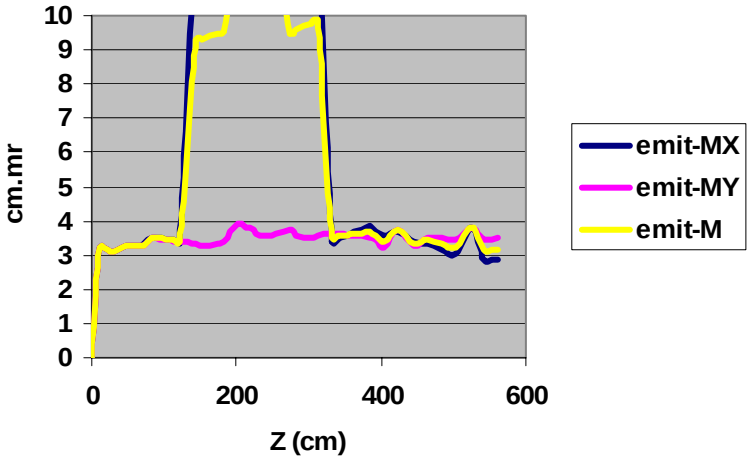

Figure 5.14 ε_M vs. z of an ellipsoid laser distribution on cathode with Z-bend system

5.5. RHIC e-cooling injector longitudinal emittance

Fig.5.15 (left) shows the longitudinal phase space after acceleration through two cavities (before the 3rd harmonic cavity). The longitudinal emittance is dominated by sine curve like of phase dependent accelerating effect in linac. The 3rd harmonic frequency cavities are employed to correct the longitudinal phase space. The cavity geometry is scaled from the fundamental cavity. Its aperture size is 3.3cm in radius and is still much larger than the envelope radius (~1cm) in the cavity. The 3rd harmonic cavity introduces some energy loss (~10%) because the beam is working near the decelerating peak phase. Fig.5.15 (right) shows the longitudinal phase space at injector exit. The longitudinal emittance is reduced from 730deg.keV (before 3rd harmonic cavity) to 100deg.keV (at linac exit). Ideally the longitudinal energy spread after stretching (bunch length L=20cm) would be:

$$dE/E = \frac{100\,\mathrm{deg.}\cdot keV}{(20cm/0.1184cm)\,\mathrm{deg.}\times 54MeV} \approx 1.1\times 10^{-5}$$

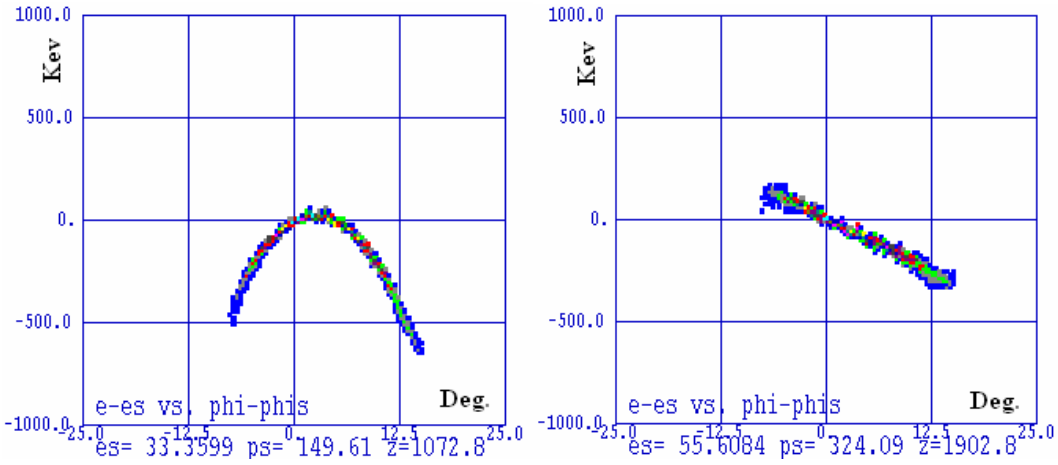

Figure 5.15 Longitudinal phase space before the 3rd harmonic cavity and at injector exit

We conclude that the transverse emittance ε_M for the RHIC e-cooling can be as small as to 35μm and longitudinal emittance can be as small as 100deg.keV. These results completely match the RHIC e-cooling requirements.

CHAPTER 6. STUDY OF SECONDARY EMISSION ENHANCED PHOTOINJECTOR (SEEP)

6.1. Introduction of SEEP

The creation of high average-current, high brightness electron beams is a key technology for a large number of accelerator-based systems, such as ultra-high-power Free-Electron Lasers (FELs), Energy-Recovery Linac (ERL) light sources, electron cooling of hadron accelerators, and many more.

Laser photocathode RF guns have proven to be the ideal device for producing the high brightness electron beams (or low emittance at high bunch charge devices). The high electric field that may be achieved in the RF gun is the key factor in getting a large charge with a small emittance.

Metallic cathodes are popular in RF guns that operate at a very low average current. They have very low Quantum Efficiency (QE~0.1% or smaller) and are usually driven in the near UV. Semi-conducting photocathodes can provide very high QE (~10%) at a longer wavelength (IR to green light), but they are very sensitive to contamination or ion bombardment and thus have short lifetimes. Another problem may be encountered in superconducting guns which are best suited for CW operation, high average current and low emittance beams. The chemicals of the cathode (most common is cesium) may degrade the superconducting gun surface.

The secondary emission enhanced photoinjector is a very promising new approach to the generation of high-current, high-brightness electron beams. Fig.6.1 shows a schematic layout of such a device.

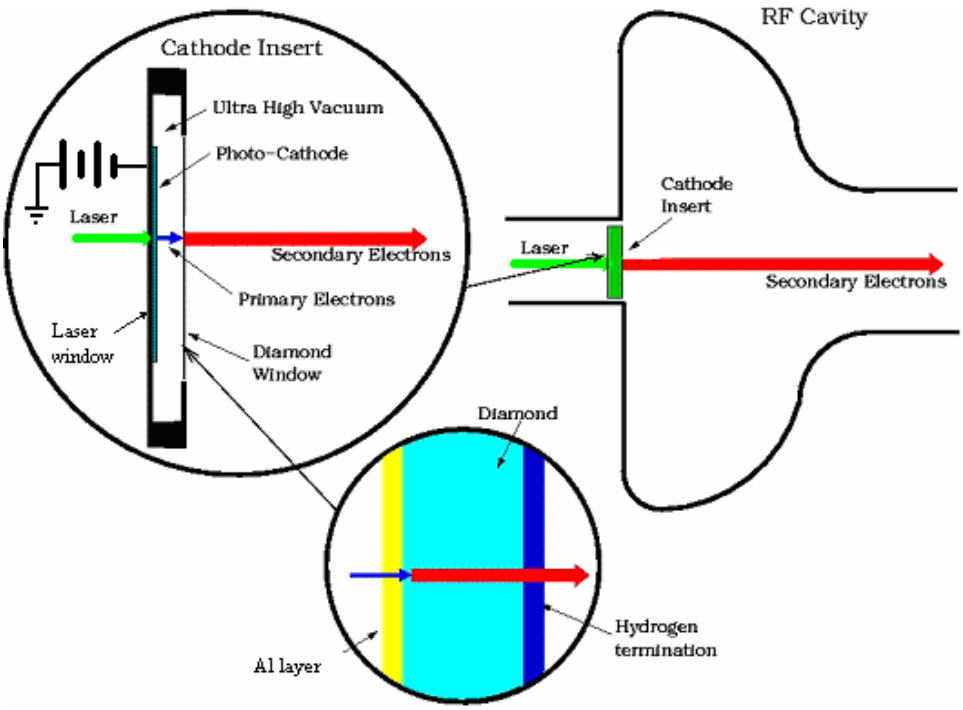

Figure 6.1 Schematic diagram of a secondary emission enhanced photoinjector.

The principle of the photo-multiplying cathode is as follows: The laser light illuminates a high-QE photocathode, such as CsK_2Sb. The primary electrons produced on the photocathode are accelerated to a few thousand electron-volts by a DC field applied between the photocathode and a metal layer on a diamond window. The primary electrons penetrate the thin metal film, which is deposited on the backside (left side) of

the diamond window and produce a large number of secondary electrons in the diamond. The Secondary Electron Yield (SEY) can be much larger than 100. The secondary electrons drift through the diamond under a high RF electric field and emerge into the accelerating proper of the "gun" through a Negative Electron Affinity (NEA) surface of the diamond.

The advantages of the new approach include the following:

1. Reduction of the number of primary electrons by the large SEY, i.e. a very low laser power requirement in the photocathode producing the primaries.
2. Protection of the cathode from possible contamination from the gun, allowing the use of large quantum efficiency but sensitive cathodes.
3. Protection of the gun from possible contamination by the cathode, allowing the use of superconducting gun cavities.
4. Production of high average currents, up to ampere class.
5. Expected long lifetime, due to the reduced current from the photocathode, encapsulated ultra-high vacuum and protection from external contamination.

The heat dissipation problem is the main technical challenge in the application of the diamond cathode. We present a detailed calculation of heat sources and the temperature distribution. Some properties of the secondary electron beam related to beam dynamics are also reported. These results demonstrate the feasibility of this kind of cathode.

Naturally, this cathode will be most suitable for a superconducting RF gun for CW operation, but it has significant advantages also for normal conducting, pulsed RF guns and DC guns. In the following, we will describe the application of this new paradigm to a

superconducting RF gun working at 704MHz which is the RF frequency of electron cooling project for RHIC. Extensions to the other applications are straightforward.

6.2. The diamond and its Negative Electron Affinity (NEA) surface

The crystal structure of Diamond is shown in fig.6.2. The lattice constant is 3.57Å and the atom density is $1.76\times10^{23}/cm^3$ [17]. It has very wide bandgap (5.47V) between the conduction and valence bands at 300K [18]. This makes diamond a good insulator with very high breakdown field (1000MV/m) [19] [26]. Furthermore, it is a material which easily demonstrates Negative Electron Affinity (NEA) [20] [21] [22] [23] [24]. The concept of NEA is schematically shown in fig.6.3.

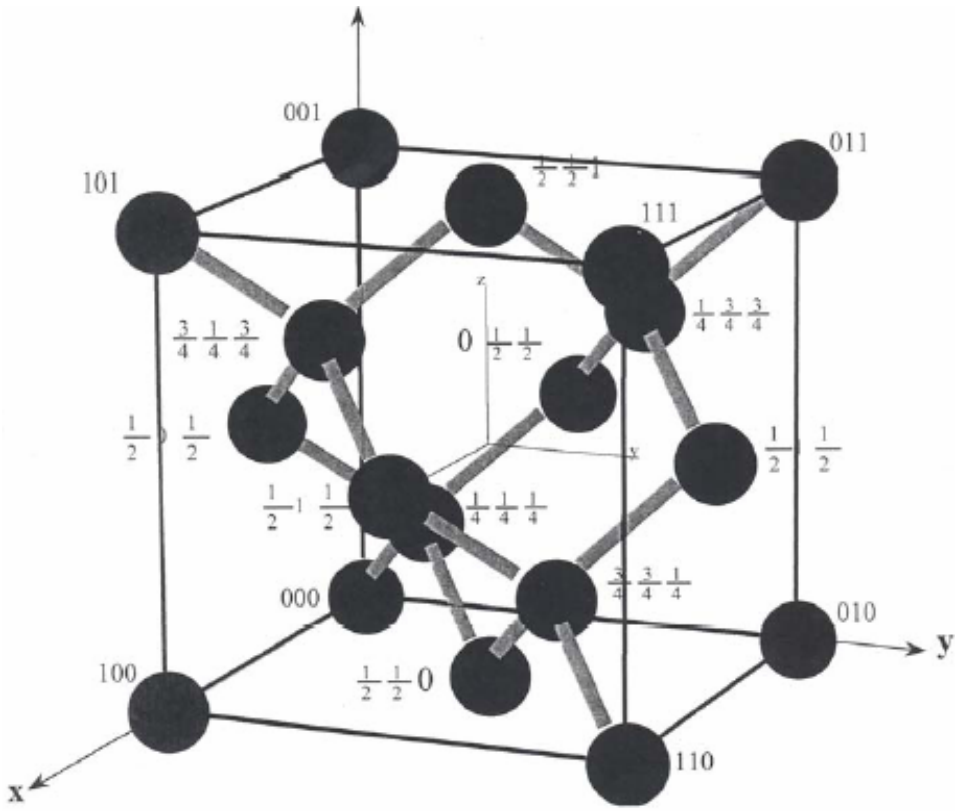

Figure 6.2 Diamond crystal structure

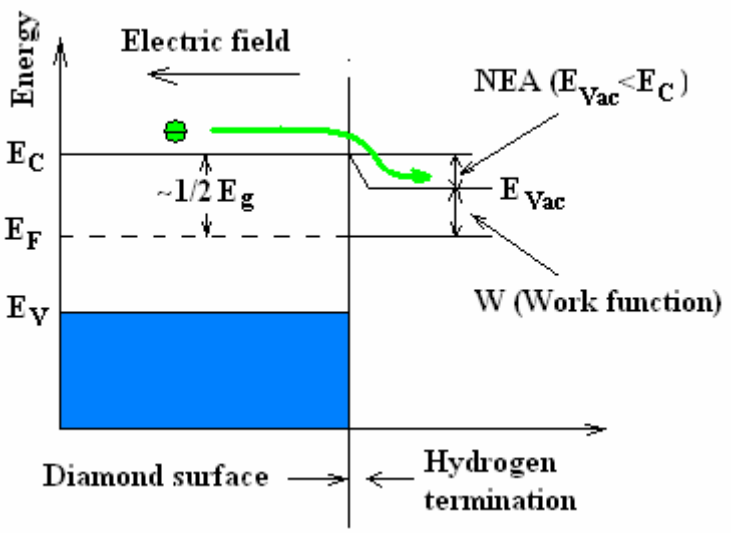

Figure 6.3 The NEA surface

The NEA is defined as the vacuum energy level minus the conduction band minimum energy level.

$$NEA = E_{Vac} - E_C \qquad (6.1.1)$$

The Fermi levels of the diamond and of the termination materials (hydrogen or alkaline elements) are aligned. Since the termination material has a relatively low work function, and then the vacuum level can be lower than the bottom level of the diamond's conduction band. The electrons can escape to vacuum without experiencing any potential barrier. A cesium termination has a higher NEA than Hydrogen because of its lower work function. It is reported [24] [30] that the Cesium termination has $NEA < -1eV$ and Hydrogen termination has $NEA \approx -0.3eV$.

Diamond also has other excellent properties that make it the perfect material for the secondary emission cathode. It is the hardest material. It can be made free standing even for very thin films (~10μm thick). It has the highest thermal conductivity of any solid,

allowing it to handle high power with a thin film (see details in section 6.7). The very high mobility and saturation velocity ($2.7\times10^5 m/s$ [25] [26]) make it applicable for high-frequency RF cavities.

6.3. The metal layer.

The metal layer is used to replenish the diamond for loss of the secondary electrons and provide a return path for the RF current (see section 6.4 & 6.9 for details). One would like to use a material with high electrical conductivity (σ) to reduce the Ohmic losses. One would also like a material with low energy loss, or long range parameter (R_{CSDA}) in the Continuous Slowing Down Approximation (CSDA). The figure of merit is the parameter $\sigma\times R_{CSDA}$ (the higher, the better). Other considerations are ruggedness and good contact with the diamond. Possible material choices are aluminum (Al), Copper, Silver, Gold and platinum. aluminum has the highest $\sigma\times R_{CSDA}$. For the sake of the discussion we will assume the use of aluminum for the metallic layer on the diamond film.

The thickness of the aluminum film is determined by considerations of its the resistance, and primary electron energy loss. The aluminum CSDA range parameter R_{Al} at 10keV of primary electron energy is [27]:

$$R_{Al}(10keV)=3.5\times10^{-4}\left(g/cm^2\right)$$

The average stopping distances L_{STP} is:

$$L_{STP}(10keV)=R_{Al}(10keV)/\rho=1.3\mu m$$

where ρ is the density of aluminum (ρ=2.7g/cm^3). If we assume the aluminum thickness (t_{Al}) to be 800nm, the average primary electron energy after the film would be about

4keV, which is in the acceptable range of the primary electron energy on diamond. Therefore the aluminum thickness is chosen to be about 800nm.

The heat power produced on the aluminum film is carried out by the diamond material, which, as noted, has excellent thermal conductivity (see section 6.7 for details).

6.4. RF penetration of the aluminum film

The skin depth for aluminum at 704MHz is:

$$\delta_{Al} = \sqrt{\frac{2}{\mu\omega\sigma_{Al}}} \approx 3.1\mu m \tag{6.4.1}$$

Although the aluminum thickness $t_{Al} << \delta_{Al}$, the RF penetration of the aluminum film is very poor.

As schematically shown in Fig.6.3, the metal film is located at the center of a cavity of TM010 mode. The RF fields near the axis on the film surface towards the cavity are:

$$E_{z1} = E_0 J_0(kr), \quad H_{\phi 1} = j\frac{E_0}{\eta} J_1(kr) \tag{6.4.2}$$

therefore,

$$\frac{\partial E_{z2}}{\partial r} + \frac{E_r}{d} = -j\omega\mu H_{\phi 2}. \tag{6.4.5}$$

As $E_r = R_s i_r = (1-\alpha) R_s H_{\phi 1}$, one has:

$$\alpha = \frac{1}{1 - j\dfrac{2\omega\mu d}{R_s}} \tag{6.4.6}$$

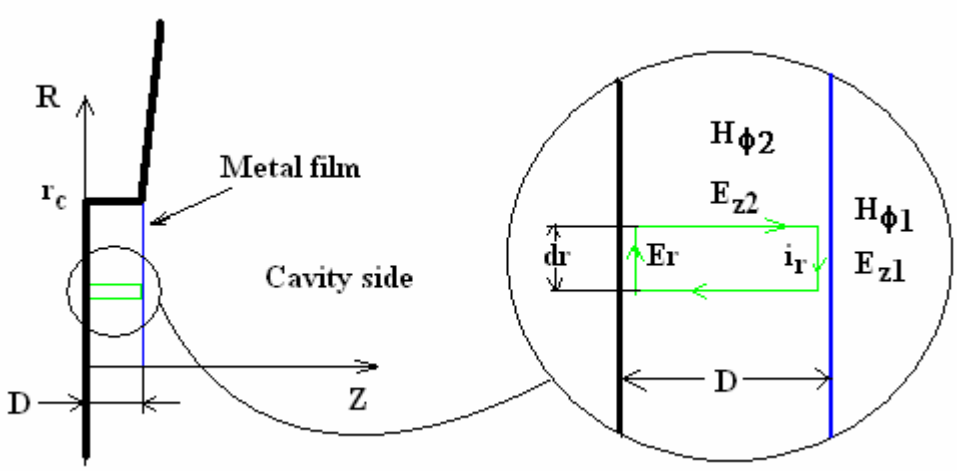

Figure 6.3 Schematic plot of RF penetration through a thin metal film

One can see that the ratio $\frac{2\omega\mu d}{R_s}$ determines the penetration. If *d* approaches zero, then α approaches to 1, meaning complete penetration. It decrease fast when *d* increases. The smaller the surface resistance, the smaller the penetration.

Experiments (see section 7.1 for details) show that even if the metal film thickness is as small as 10nm the penetration is still very poor. So, aluminum film not only carries out the replenishment current but also the large RF shielding current. Therefore RF shielding currents must be included in the thermal load calculations.

6.5. The secondary electron yield (SEY)

SEY is an important parameter designing the system. Higher SEY will need less primary electron current and power. Most of the work on Secondary Electron Emission (SEE) from diamond has been done in the reflection mode where the primary and secondary electrons traverse the same side of the sample with little or no external electric

field. Fig.6.4 shows the measured SEY for this mode [28]. The production of secondary electron-hole pairs inside the diamond is very high and is approximately a linear function of primary electron energy. It is reported that the average energy loss of a primary electron for the generation of one electron–hole pair is about 13eV [29]. The departure of the curve from a straight line at higher primary electron energy in fig.6.4 may caused by the deeper escape distance.

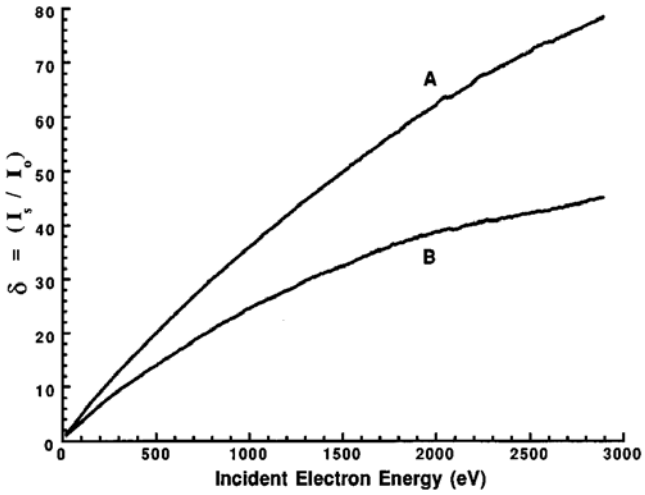

Figure 6.4 SEY measurement for reflection mode. (A) After a saturated atomic-hydrogen exposure. (B) After heating to 900˚C

Due to electron optical calculations and consideration of wake fields, we determined that the reflection mode does not work for RF cavity applications. The preferred option is the transmission mode. The secondary electrons are produced near the aluminum film side and drift through the diamond under a strong RF field. The secondary electron energy in a 10MV/m field is about 0.4eV above the bottom of conduction band V_C (see 6.10.3 for details). The NEA of hydrogenated Chemical Vapor Deposition (CVD) diamond surface is -0.32±0.26eV [24] [30], In addition to the Schottky effect it is

expected that almost all the produced secondary electrons would come out of the diamond. Therefore the expected SEY for our transmission mode is much higher than shown in fig.6.4. In the thermal simulation below we will assume SEY of 300 at 4keV (~1 electron-hole pair per 13eV energy loss) for our application.

6.6. The thickness of diamond window

As stated above, the diamond window plays a role not only in the production of the secondary electrons but also in the heat dissipation.

One would like to use a thicker diamond to improve the thermal conduction of the window. But for our RF application the diamond thickness is limited by the allowed transit time of the secondary electrons through the diamond.

As discussed above, the optimized initial phase for RHIC e-cooling is smaller than 35deg. The RF phase for secondary electrons generated near the backside of the diamond should be at least 5 degrees. The time allowed for secondary electrons to pass through the diamond is less than 30 degrees, i.e., about 120 pico-seconds.

The electron drift velocity in diamond under high external electric field has been experimentally measured [25]. The data shows that when the external field is larger than 2MV/m the electron drift velocity is saturated at $v_D \approx 2.7 \times 10^5 m/s$ and is independent of temperature. This means that the secondary electron bunch drift velocity in diamond is almost constant except when the charge density is very high and the space charge force is comparable to RF field. The optimum diamond thickness for our example is estimated to be:

$t_{Dmd} < 120 ps \times v_D = 32 \mu m$

We will assume the diamond thickness to be 30μm in our thermal calculations.

6.7. Diamond thermal conductivity

The diamond has an outstanding thermal conductivity. The diamond thermal conductivity as a function of Temperature T can be expressed by the Debye model as [31] [32] [43]:

$$k(T) = \frac{k_B}{2\pi^2 v_s}\left(\frac{k_B T}{\hbar}\right)^3 \int_0^{\theta_D/T} \tau(x)\frac{x^4 e^x}{\left(e^x - 1\right)^2} dx \qquad (6.7.1)$$

where k_B and ħ are the Boltzmann and Planck constants, $x = \hbar\omega / k_B T$ and ω is the phonon frequency, $\theta_D \sim 2230K$ is the diamond Debye temperature, $v_S = \left\langle \sqrt{Y/\rho} \right\rangle \approx 1.32 \times 10^4 m/s$ is the averaged phonon velocity, which is independent of the temperature [43] and τ(x) is the total relaxation time for different scattering mechanisms. If we assume that τ(x) is independent of phonon energy ħω then we get our simple form for the kinetic theory:

$$k = \frac{1}{3} C v_s \ell = \frac{1}{3} C v_s^2 \tau \qquad (6.7.2)$$

where C is the specific heat of diamond, l is the mean free path.

There are several types of processes that change the crystal momentum:

1. The crystal boundary scattering (τ_b) which can be expressed as:

$$\tau_b^{-1} = v_s / 1.12d \qquad (6.7.3a)$$

where d is the crystal size (or grain size) of diamond.

2. Umklapp process (τ_u):

$$\tau_u^{-1} = 1.31 T^4 x^2 \exp(-270/T) \qquad (6.7.3b)$$

3. ^{13}C isotopes scattering (τ_{is}):

$$\tau_{is}^{-1} = 0.346x^4T^4 \qquad (6.7.3c)$$

4. Impurity scattering (τ_{im}):

$$\tau_{im}^{-1} = Ix^4T^4 \qquad (6.7.3d)$$

where I is a parameter reflecting the degree of impurities. The total relaxation time can be expressed as:

$$\tau(x)^{-1} = \tau_b^{-1} + \tau_u^{-1} + \tau_{is}^{-1} + \tau_{im}^{-1} \qquad (6.7.4)$$

The larger the crystal size d, the longer the relaxation time τ.

Fig.6.5 shows the thermal conductivity as a function of T using above theory for different crystal sizes d, assuming I=0, and the experiment data for an 18μm diamond film and a 13μm diamond film [43]. When d increases, k increases while its peak shifted towards lower T.

When d=1mm, the peak of thermal conductivity k is about 5000W/mK. It is expected that when d continues increases the peak of k will approach the extreme value of 14000W/mK.

For our 30μm CVD diamond Fig.6.6 shows the grain size and the surface roughness after polishing. The average grain size is about 15μm and surface roughness <<1μm. We adopt 10μm as the grain size. If the diamond film were a single crystal film, the thermal conductivity would be even better. Although the thermal conductivity is much smaller than in a larger size, pure diamond, it is still a very good thermal conductor.

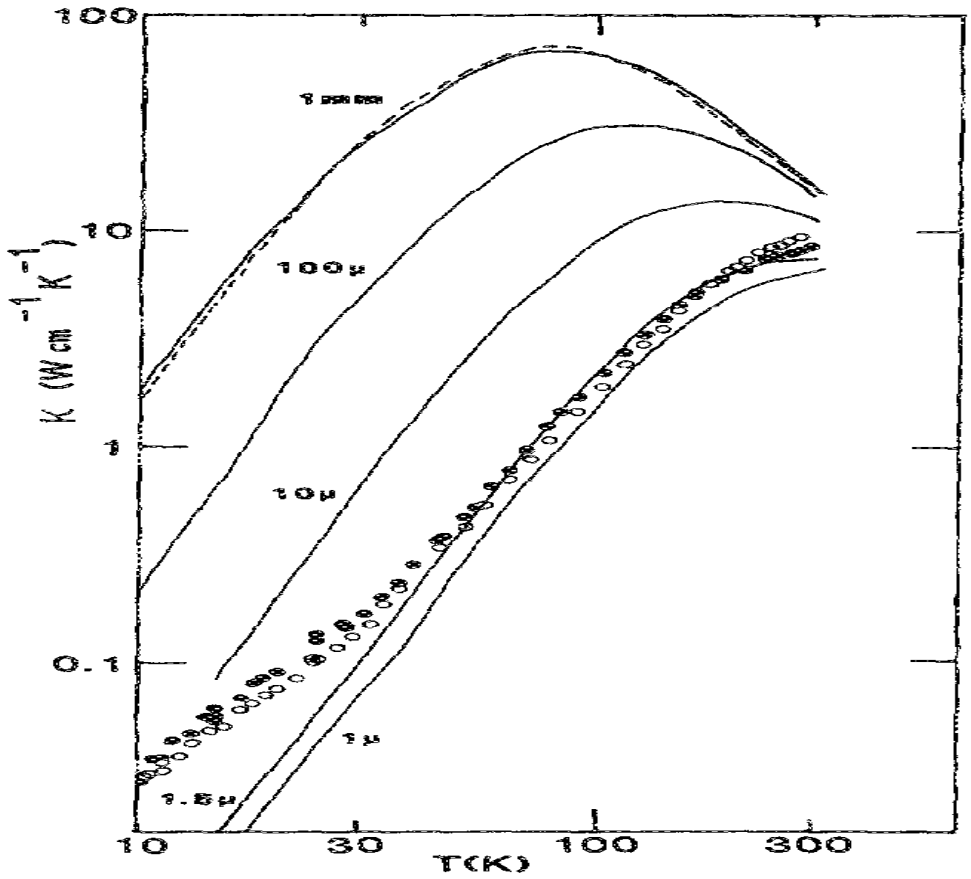

Figure 6.5 Thermal conductivity as a function of temperature for different grain sizes

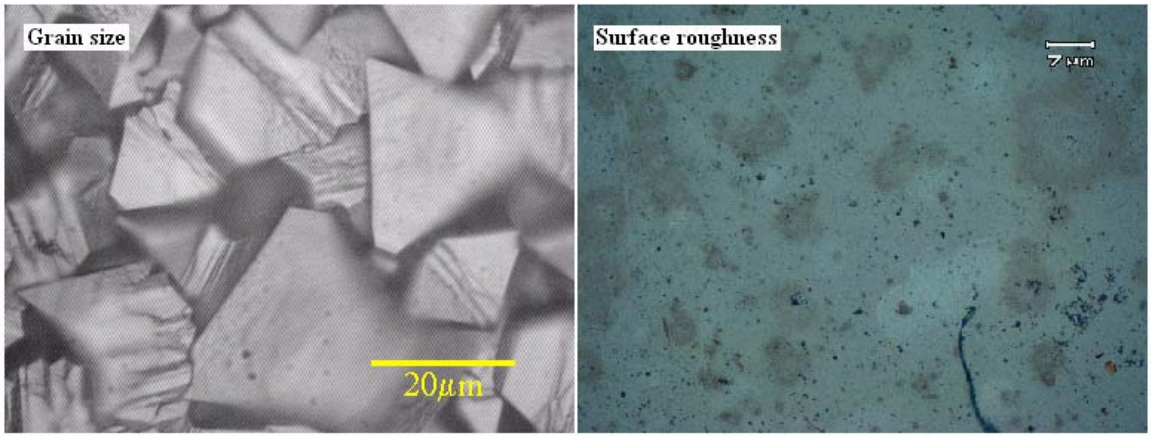

Figure 6.6 Grain size (left) and surface roughness (right) of our 30μm thick diamond sample

6.8. The Effect of Impurities

Diamonds generally have the following impurities: Boron (p-type), Nitrogen (n-type), Hydrogen (n-type), Phosphorus (n-type), Lithium (n-type) and Sodium (n-type). Impurity have 3 main effects: heating of diamond, trapping of charge carriers and field shielding.

6.8.1. Heating

Under a strong RF field free electrons in the diamond conduction band (nitrogen doping) will behave the same way as secondary electrons. They produce not only extra heat but also a dark current. Holes in the valence band (boron doping) will only produce the extra heat.

The number of the activated electrons or holes from the impurities should be well below the number of secondary electrons in diamond. For example, if the secondary electron charge per bunch is 20nC, the number of secondary electrons is:

$$N_e \approx \frac{20\times10^{-9}}{1.6\times10^{-19}} \approx 10^{11} \qquad (6.8.1)$$

The concentration of the activated electrons or holes depends on the impurity type, impurity concentration and temperature.

Hydrogen, phosphorus and other alkali elements impurities form strong chemical bonds with carbon with very few activated electrons.

F or a type-2a diamond the main impurity is Nitrogen. This impurity can be about 1ppm or so ($1ppm = 1.78\times10^{17}/cm^3$). Depending on the impurity concentration, the activation energy can be 1.7eV or more. The number of thermally excited electrons in the conduction band at T=500K in the diamond cathode can be estimated as:

$$N_{eN} \approx 2\left(\frac{m_e^* k_B T}{2\pi\hbar^2}\right)^{3/2} \exp\left(-\frac{1.7eV}{2k_B T}\right)\times 1ppm \times V \approx 10^3 \qquad (6.8.2)$$

where $m_e^* \approx m_e$ is the effective mass of electron and $V \approx \pi r_C^2 L_D \approx 10^{-2} cm^3$ is the volume of the diamond cathode, $r_C = 1cm$ is the cathode radius and $L_D = 30\mu m$ is the diamond thickness. N_{eN} is generally much less than N_e and can be ignored.

The boron doping has an activation energy ranges from ~0.1eV to ~0.37eV depending on the doping concentration. The number of holes under these conditions is estimated as:

$$N_{hB} \approx 2\left(\frac{m_h^* k_B T}{2\pi\hbar^2}\right)^{3/2} \exp\left(-\frac{0.37eV}{2k_B T}\right)\times D_B \times V \approx 10^9 n_B[ppm] \qquad (6.8.3)$$

where n_B is the concentration of the boron doping in ppm. To have $N_{hB} << N_e$, D_B need to be much less than 1ppm which is common for type-2a diamond.

6.8.2. Charge carrier trapping

The charge carrier trapping mechanics is illustrated in fig. 6.7. In general, diamond has the following defects: foreign substitutional atoms, e.g., B, N and P, foreign interstitial atoms, e.g., H and Li, the self-interstitial interstices, vacancies and grain boundaries, which are formed by group of interstices.

The defects generate states with energy levels in the band gap. When charge carriers (electrons or holes) move though the lattice, they can be captured by the defects (fig.6.8). Once the carriers are captured by defects, they can be released by thermal excitation or light. The release time can be much longer than the capture time.

The charge carriers' capture probability depends on the defect density and the defect cross-section (i.e., the inverse capture time). As reported on ref. [33], the two most important deep levels affecting charge carrier lifetime have excitation energies of 1.14eV and 1.23eV. The first has a cross-section= $4\times10^{-13}cm^2$, and for their sample a concentration $\approx 10^{16}/cm^3$ and a capture time of about 20ps, the second a cross-section= $9.5\times10^{-14}cm^2$, a concentration $\approx 10^{16}/cm^3$ and a capture time of about 80ps. The other levels have very small cross-sections, so the capture times are from 200ps to 100ns and are ineffective.

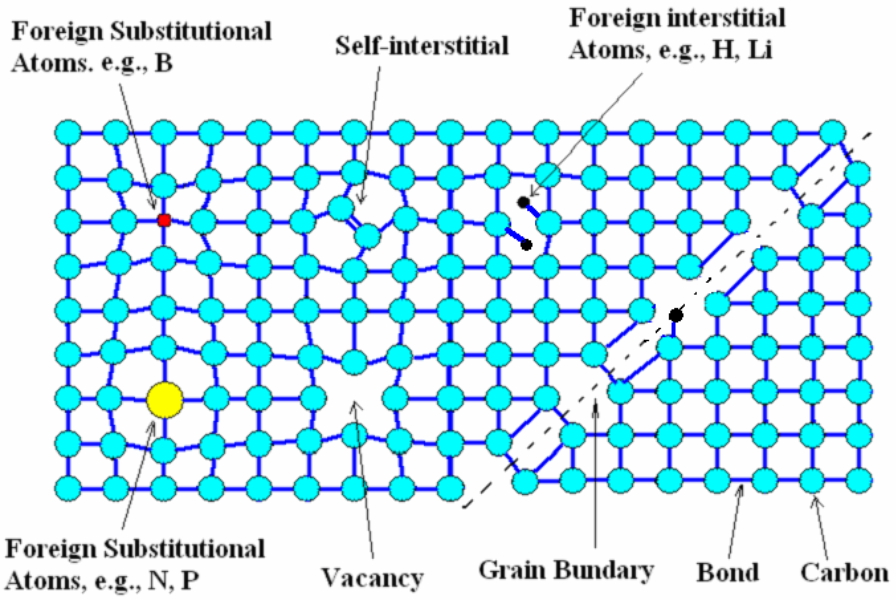

Figure 6.7 Schematic 2-D view of charge carriers traps

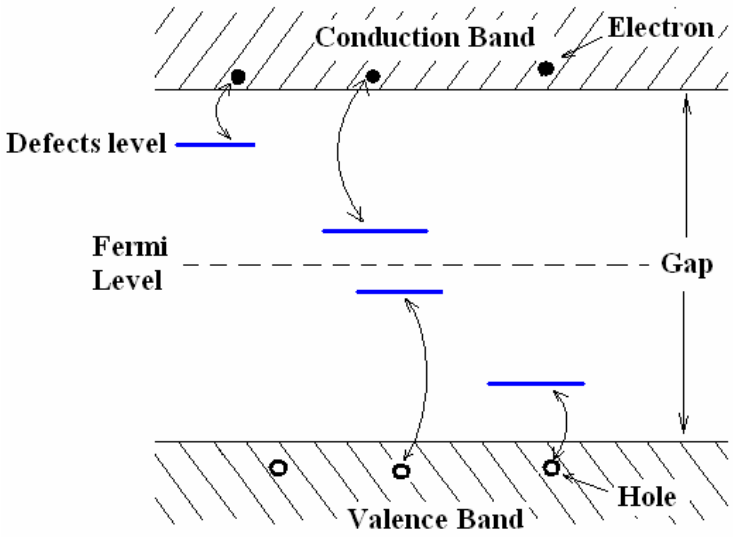

Figure 6.8 Charge carriers capture and release by excitation

Trapping creates space charge and partially compensates the external field (field shielding). It also generates dark currents and heat. The trap concentration in the diamond must be small enough for the diamond amplified cathode application.

There are many ways to reduce the defects in diamond:

1. Using purer methane and hydrogen gas mixtures.
2. Controlling the diamond growth temperature and growth speed, so that the defects in grain are reduced.
3. As the traps are mostly concentrated on grain boundaries [34], one can make a single crystalline diamond or at least very large grain size to reduce the defects. The grain size increases linearly from substrate side (the side where the growth process was started) to growth side. One can grow a thick diamond and then polish both sides, especially the substrate side, to the desired thickness. The larger grain size is also helpful for thermal conductivity.

It is reported that by thinning the samples (increase grain size) the charge carrier distance (ccd) increases more than 100% and reaches more than 400μm [29]. In another report [35] the ccd is estimated even more than 10cm in a high-purity (Nitrogen concentration below $1\times10^{15}/cm^3$) single-crystal diamond. As our diamond thickness is only about 30μm, the trapping will be no problem if we use high quality diamond.

6.9. Diamond temperature

The heating of the diamond cathode-amplifier comes from:

1. The power deposited by the primary electrons.
2. The power deposited by the transport of the secondary electrons through the diamond under the RF field.
3. Resistive heating by the electron replenishment current flowing through the aluminum film.
4. Power dissipation by the RF shielding currents through the aluminum film.
5. The power dissipated by the movement of the impurity induced free electrons in the diamond conduction band (Nitrogen doping) and holes in the valence band (Boron doping) driven by the RF field.

There is also the power from electron replenishment current in the diamond. However, the replenishment distance is very small (~1μm), therefore this effect is negligible.

A FORTRAN code was written to simulate the temperature distribution in diamond including all the factors discussed above. The criterion is that the maximum temperature in diamond cathode be well below 1000˚C to avoid significant Hydrogen desorbtion from the surface [36]. The code includes the correct temperature dependent material properties,

such as thermal conductivity and resistivity. The intermittent nature of the current is accounted for by considering peak and average current effects.

Example 1: electron cooling for RHIC [37]

The electron cooling for RHIC requires a large charge per bunch (~20nC/bunch), but a relatively low repetition frequency (9.4MHz), i.e., low average current. This requires large cathode radius (R~10mm) to reduce space charge force.

Figure 6.9 shows the temperature distribution from the center of the diamond (R=0) to diamond's edge. We assume that the primary electron energy is $E_{\Pr i} = 10keV$, the thickness of the diamond window is $t_{Dmd} = 30\mu m$, the thickness of the aluminum layer is $t_{Al} = 800nm$, the peak RF field on cathode is E_0=15MV/m, and the secondary electron yield is SEY=300. The temperature on the diamond's edge is fixed at $T_{edge} = 80K$ (assuming Liquid Nitrogen (LN) cooling) and the primary electron pulse length is $Pls_{\Pr i} = 10\deg$. The dependence of the temperature on the radius is shown for different cathode radii.

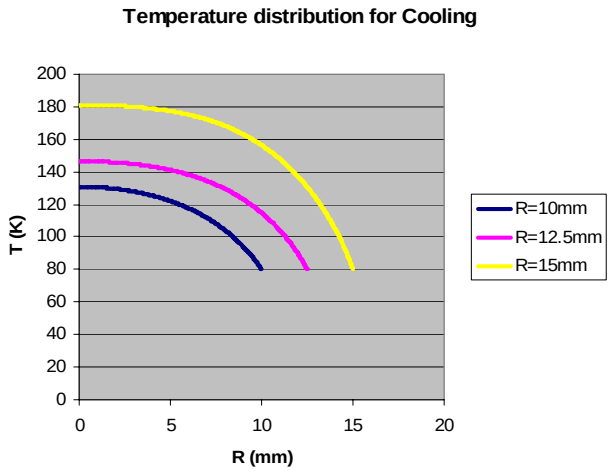

Figure 6.9 T(r) for RHIC e-cooling parameters with $t_{Al} = 800nm$, $T_{edge} = 80K$

The power contributed by the various sources is listed for three diamond sizes in table 6.1:

Table 6.1: Heat powers from various sources in the RHIC e-cooling application

R	10mm	12.5mm	15mm
Primary	6.3 (W)	6.3(W)	6.3(W)
Secondary	7.6(W)	7.6(W)	7.6(W)
RF	7.5 (W)	20.0(W)	48.6(W)
Replenishment	0.042(W)	0.046(W)	0.054(W)
Total	21.4 (W)	33.9(W)	62.5(W)

We see that the total power is dominated by RF heating when R>12mm, and this source increases with cathode size. However, even with a radius of 15 mm the temperature of the cathode center is still below 300 K.

Fig. 6.10 shows the temperature distribution of a R = 12.5 mm cathode for different edge temperatures. In case where T_{edge} is larger than LN temperature due to edge cooling efficiency, for instance, $T_{edge} = 250K$ & $T_{edge} = 400K$.

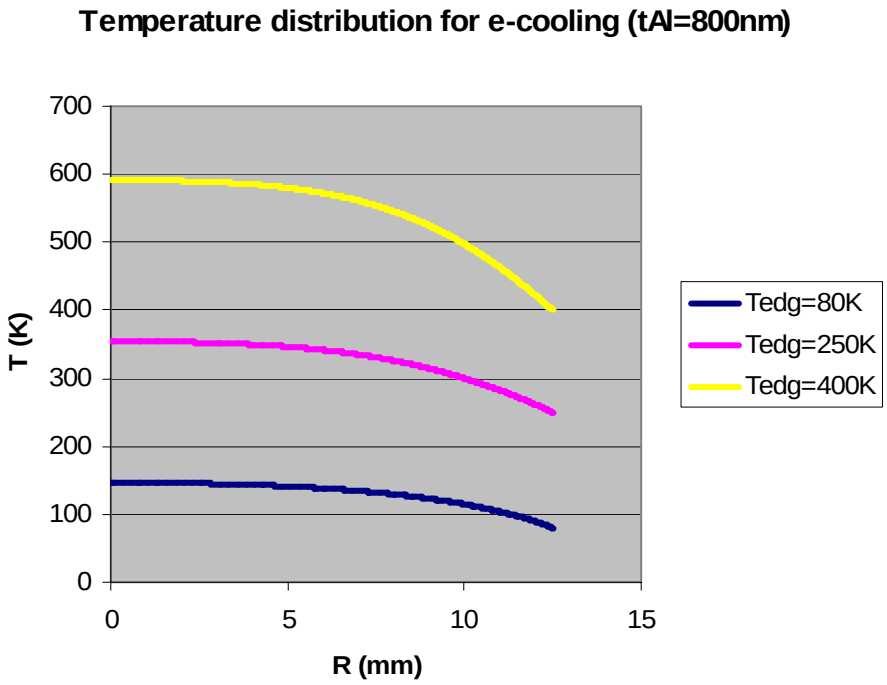

Figure 6.10 T(r) for RHIC e-cooling with R=12.5mm, $T_{edge} = 80K$, 250K & 400K

The corresponding power contributions are listed in table 6.2:

Table 6.2: Heat powers from various sources as a function of the diamond edge temperature in the RHIC e-cooling application

Tedge	80K	140K	200K
Primary	6.3(W)	6.3(W)	6.3(W)
Secondary	7.6(W)	7.6(W)	7.6(W)
RF	20.0(W)	53.4(W)	88.0 (W)
Replenishment	0.046(W)	0.123(W)	0.202(W)
Total	33.9(W)	67.3(W)	102.0(W)

One can see that cooling the edge down to 80 K is not a critical requirement.

Fig.6.11 shows the temperature dependence on the aluminum thickness. One can see that t_{Al} be 800nm is not a critical requirement either.

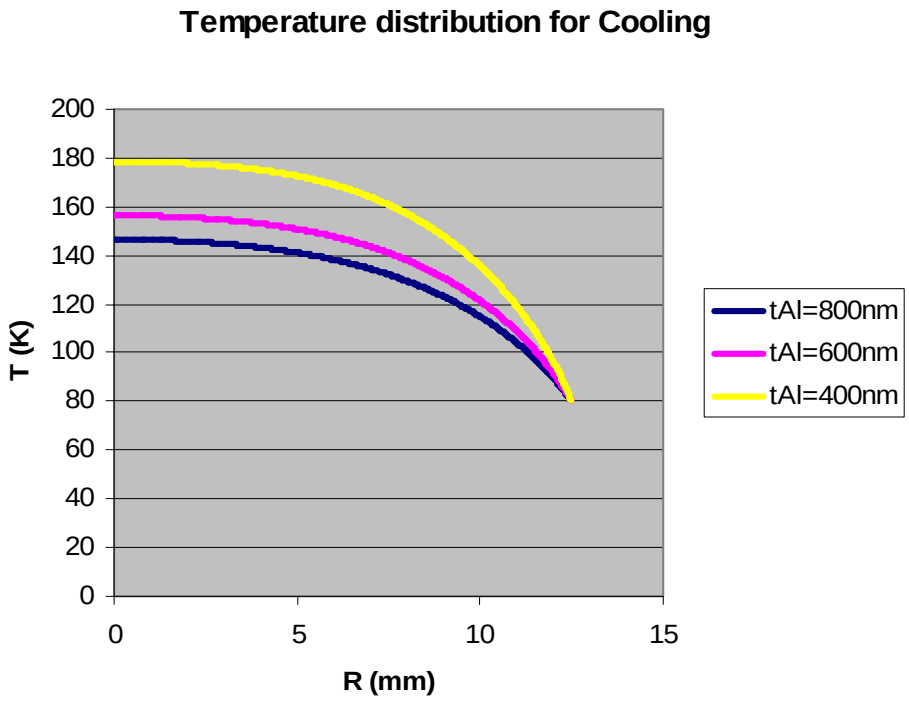

Figure 6.11 T(r) dependence on T_{Al}. The primary electron energies are adjusted according to their t_{Al} to have the same secondary electron production

The temperatures in fig.11 would be a little bit higher if we include the effect of thin film effect [42] on electrical conductivity. We find that the thin film effect on electrical conductivity only affects very thin metal layers (<100nm) and can even for t_{Al}=400nm be neglected.

Fig.6.12 shows the effect of the diamond thickness. One can see that the diamond thickness can be as small as 15μm.

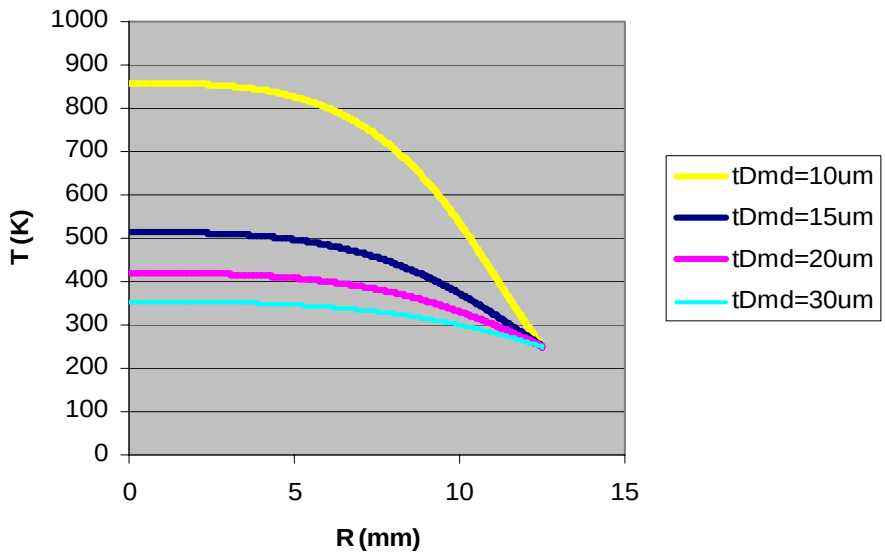

Figure 6.12 T(r) dependence on t_{Dmd} with a grain size of 10μm and Tedge of 250K.

Example 2: Energy Recovery Linac (ERL) project [38] in BNL.

This application requires larger average current (1A) but relatively low charge/bunch (1.42nC/bunch), i.e., higher repetition frequency (703MHz). Therefore one can use a small cathode radius.

Fig.6.13 is the temperature distribution, assuming that E_{Pri}=10keV, t_{Dmd}=30μm, t_{Al}=800nm, E_0=15MV/m, SEY=300, T_{edge}=80K and Pls_{Pri}=10deg.. The curves are for different cathode radii.

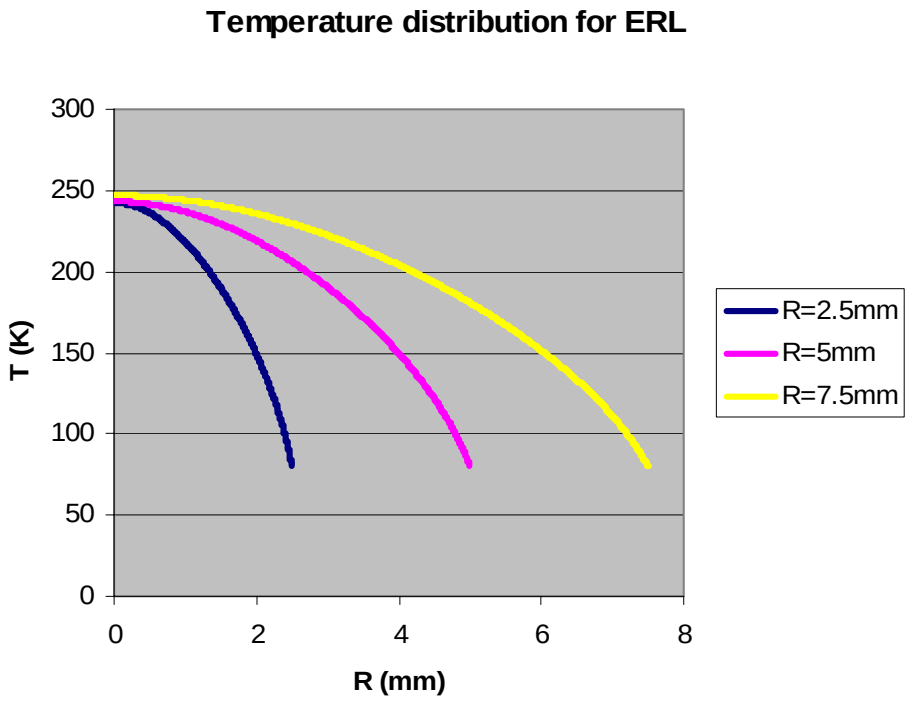

Figure 6.13 T(r) for ERL with R=2.5mm, 5.0mm &7.5mm

The corresponding power contributions are listed on table 6.3:

Table 6.3: Heat powers from various sources in the ERL application

R	2.5mm	5mm	7.5mm
Primary	33.3(W)	33.3(W)	33.3(W)
Secondary	40.2(W)	40.2(W)	40.2(W)
RF	0.046(W)	0.67(W)	3.4(W)
Replenishment	0.025(W)	0.023(W)	0.023(W)
Total	73.6(W)	74.2(W)	76.9 (W)

One can see that the heat power is dominated by primary electron and secondary electron contributions.

One can choose a thinner aluminum film to reduce the primary electron heat power. Fig.6.14 shows the temperature dependence on $t_{Al,}$ using the CSDA model.

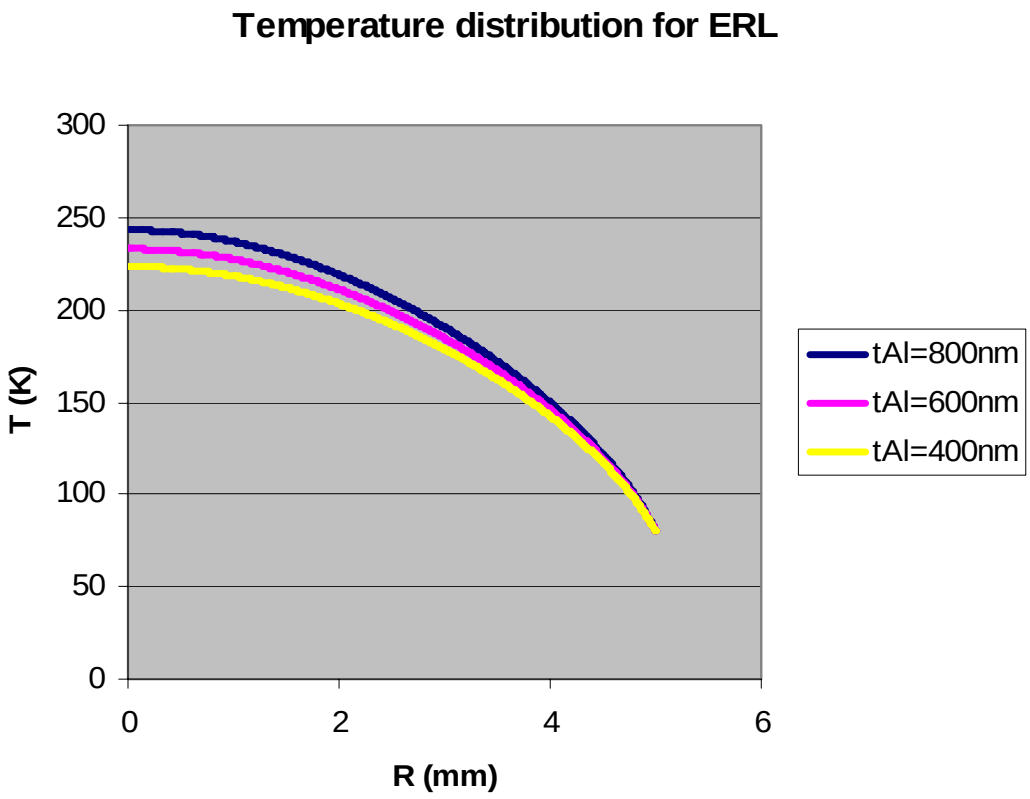

Figure 6.14 T(r) dependence on t_{Al} with R=5mm

The corresponding power contributions are listed in table 6.4:

Table 6.4: Heat powers from various sources as a function of the Al thichness in the ERL application

tAl	800nm	600nm	400nm

Primary	33.3(W)	28.3(W)	23.3(W)
Secondary	40.2(W)	40.2(W)	40.2(W)
RF	0.67(W)	0.87(W)	1.27(W)
Replenishment	0.023(W)	0.030(W)	0.043(W)
Total	74.2(W)	69.4(W)	64.8(W)

The curves show that T(r) is not sensitive to t_{Al}.

From the simulations shown one can see that the diamond cathode can easily handle 100W of heat power without reaching a too high temperature.

6.10. Secondary electron beam quality

6.10.1. Bunch broadening

As mentioned above, the secondary bunch lengthening while drifting in diamond is small because of the saturation of the drifting velocity in a strong field. The bunch lengthening mainly comes from R_{CSDA} straggling. If one assumes the probability distribution of the ranges about the mean R_{CSDA} is a Gaussian distribution, then one obtains the straggling distance of primary electrons in the diamond D_{Strg} due to range straggling as about [39]:

$$D_{Strg}(10keV) \approx 25\% \times R_C(10keV)/\rho_C \approx 0.41\mu m$$

where $R_C(10keV) = 2.82 \times 10^{-4}\left(g/cm^2\right)$[40] is R_{CSDA} of carbon at 10keV electron energy and $\rho_C = 1.7\left(g/cm^3\right)$is the carbon density. Compared to the traditional photocathode, this corresponds to a 2.6 ps straggling of laser. In other wards, the minimum bunch length of the secondary electron is equivalent to a 2.6ps laser pulse. This value can be reduced by lowering the primary electron energy, at a price of reduced amplification.

Since the secondary electrons move slowly inside the diamond the bunch length is much shorter than the primary electron bunch which moves with high speed. For example, assuming E_{Pri}=10keV and $\sigma_P = 2.4mm(40ps)$ then $\sigma_S = 6.4 + 0.4\mu m(43ps)$.

6.10.2. Charge density

If the charge density is too high the space charge field may be comparable to RF field, and will debunch the electrons during their drift through the diamond. The criterion is:

$$E_{SPC} \approx Q / \pi R^2 \varepsilon_0 << E_0 \qquad (6.10.1)$$

where Q is charge per bunch and ε_0 is the free space permeability. For our RHIC cooling example with R=12.5mm one obtains that Q should be much less than 65nC. For the ERL example with R=5mm Q should be much less than 10nC. The examples we've shown well match this criterion.

Note that once the field difference is larger than the drift velocity saturation electric field, the head and the tail of the bunch drift at the same velocity. Thus the diamond as a propagation medium suppresses bunch broadening due to space charge as long as (6.10.1) is observed.

6.10.3. Secondary electron temperature

The equation for the equilibrium electron random energy E_e as a function of the inelastic mean free path (IMFP) λ_i and the lattice temperature T_l and the electric field in the diamond can be written as follows:

$$\left(\frac{d\overline{W}}{dt}\right)_e + \left(\frac{d\overline{W}}{dt}\right)_L = -eE_0 v_D - \frac{\overline{W}(T_e) - \overline{W}(T_L)}{\tau_W} = 0 \qquad (6.10.2)$$

where $W(T_e)$ and $W(T_L)$ are electron thermal energy and lattice thermal energy, respectively. $\tau_W = \lambda_i / v_e$ is the energy relaxation time and $v_e = \sqrt{2\overline{W}(T_e)/m_e}$ is the electron thermal velocity.

For the IMFP we will use the semi-empirical formula of M.P. Seah and W.A. Dench [41]

$$\lambda_i = \left[538E_r^{-2} + 0.41(a_m E_r)^{\frac{1}{2}} \right] a_m \qquad (6.10.3)$$

where a_m is the thickness of a monolayer in nanometers, for diamond a_m= 0.1783 nm. E_r is the electron's energy above the Fermi level. Solving above two equations one obtains the electron thermal energy under $E_0 = 10MV/m$ is $T_e \approx 0.4eV$. The longitudinal temperature due to the surface roughness of the diamond can be estimated as: $T_{Surface} \approx 0.1\mu m \times 10MV/m = 1eV$.

These temperatures are in the same scale as that of a conventional photocathode. Indeed, the dominant effect is the surface roughness, which affects all cathode surfaces equally.

CHAPTER 7. EXPERIMENTS

7.1. The RF penetration of a thin metal film

7.1.1. Purpose

In the original diamond cathode scheme, a thin gold film is coated on the back of the diamond to let the RF field penetrate it. Although the thickness (10 nm in the original design) is much less than the skin depth (about 2000 nm), as theoretically studied before, the penetration is poor. This issue has originally been raised by Prof. YongXiang Zhao. This experiment is intended to verify this inference.

7.1.2. Experimental set up

The test setup is schematically shown in Fig.7.1. The cavity is a 1300MHz aluminum cavity. A few silicon wafers coated with different thickness were prepared, including one without coating and one with coating but has a ring without coating on the edge so that the coated film is isolated from the cavity. Each wafer is mounted on a support. The gap between the wafer and the cavity end plate is adjustable. The RF pickup probe is on the center of the end plate. The material of wafer is silicon with thickness of 250 μm. The coating is copper.

7.1.3. The test results

The pickup probe and a second probe at the equator (RF input) are connected to the two ports of the network analyzer 8753ES for testing the S21 parameter (RF penetration). The results were shown in fig.7.2 and fig.7.3.

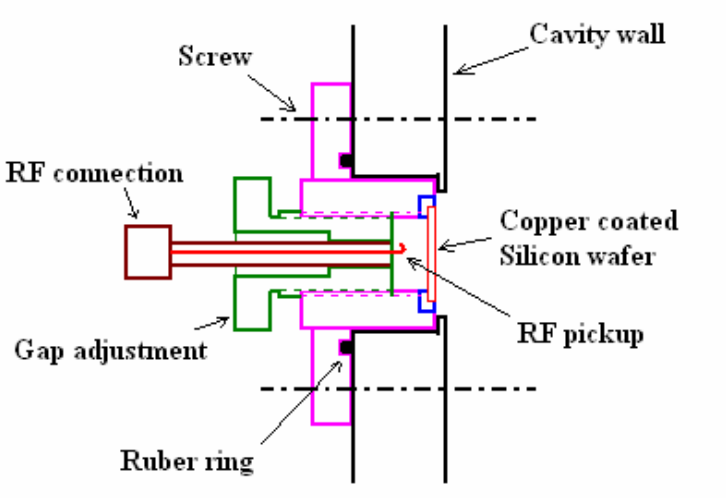

Figure 7.1 Schematic of the test set up. Another probe (not shown) is located at the equator of the cavity. The samples can be easily exchanged

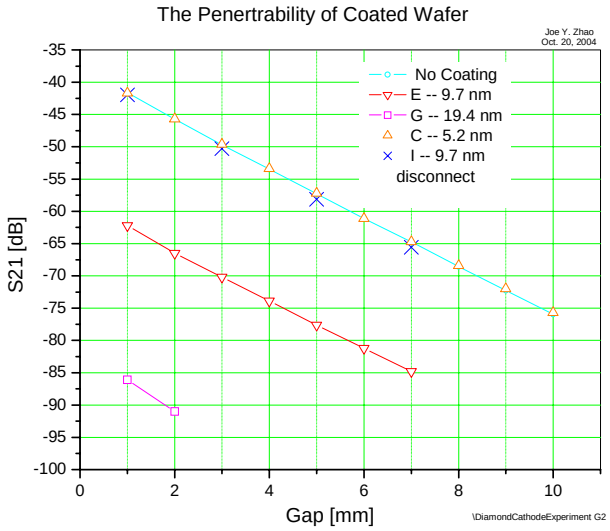

Figure 7.2 Measured field penetrations (S21 of the 2 ports network system) of different samples with various copper coating thickness.

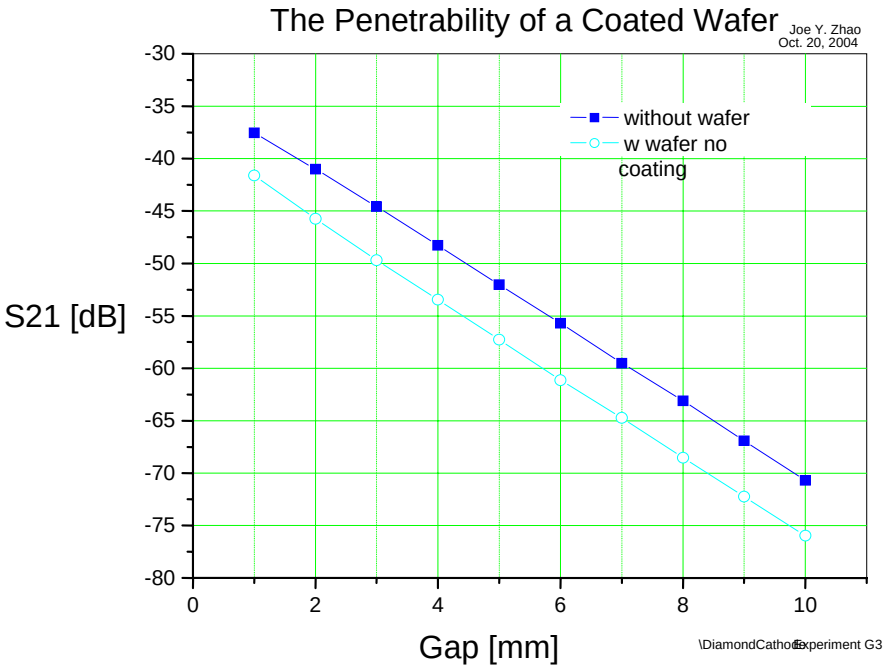

Figure 7.3 The field decay due to the silicon wafer itself

It is clear that the field is significantly decayed due the copper coating. The 9.7 nm coating reduces the field more than 20 dB, the 19.4 nm coating reduces the field more than 40 dB.

The blue crosses shown in Fig.7.2 are the data of the sample with a blank ring on its edge. They are almost the same as the wafer without coating. This indicates that the field is not blocked by this coating. This is as expected since the coating is isolated and there is no current path through it.

The wafer with 5.2 nm coating shows the same effect as the blank wafer. The reason is that the film is too thin to be a continuous film.

Fig.7.3 shows that the wafer itself (without coating) also causes some decay of the field. It is believed that the silicon is not pure.

In conclusion, the RF penetration is very poor (decay >20dB) as we expected even for a very thin metal coating film (10nm copper coating) with 1mm of gap.

7.2. The transmission of electrons and holes in diamond films.

7.2.1. Purpose.

As a first experimental step of the Secondary Emission Diamond Cathode we measured the generation of electron-hole pairs and their transmissions in the diamond under high field.

7.2.2. Experiment set up

The test setup is schematically shown in Fig.7.4. The diamond is coated on both sides with aluminum. The stainless steel (SS) plates, which are isolated from one another by kapton films, are pressed against the aluminum films. They are mounted onto a sample holder and placed in a vacuum system. The electrodes are connected to the SS plates and are led out of the vacuum so that one can apply voltages on the aluminum films and measure the currents. The primary electrons are emitted from a 0~5keV electron gun. The primary electrons strike the front side (right side) of the diamond with current ranging from 0 to 10μA. The minimum spot size of the primary electron beam is less than 1mm in diameter.

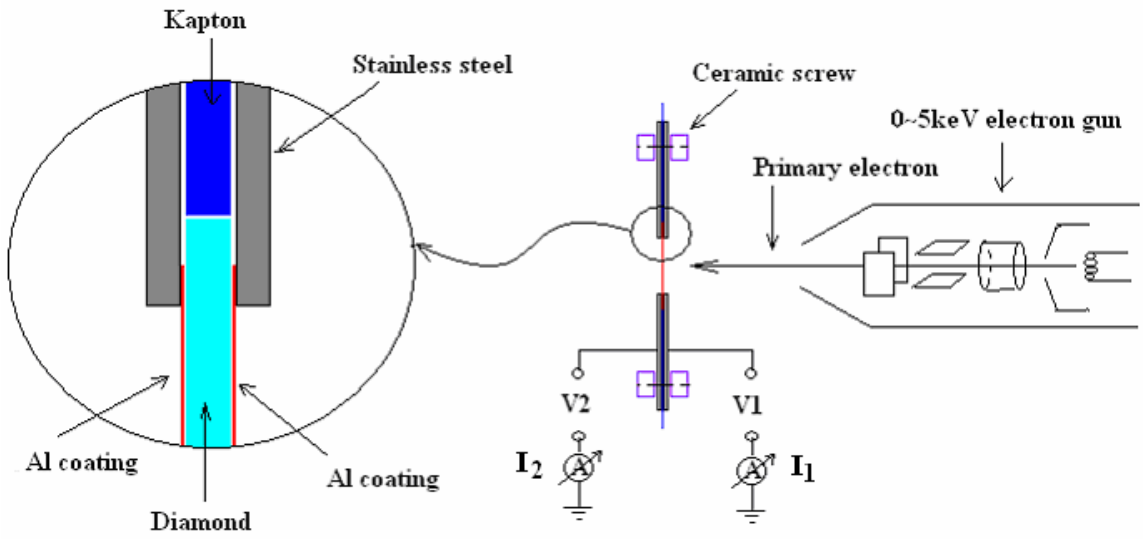

Figure 7.4 Schematic of the electron (or hole) transmission experiment. The front side coating (right side) voltage V1 and the back side coating (left side) voltage V2 range from -5kV to +5kV independently

7.2.3. Main results

- Polycrystalline diamond:

We first measured a Polycrystalline diamond sample with thickness of 200μm and diameter of 6mm provided by Harris International. The aluminum coating on the front side has a diameter of 4mm and a thickness of 20nm, the back side (left side) has a diameter of 4mm and a thickness of 50nm. The diameters of the SS plate holes are 2.5mm, so that the SS plates have good contacts with the coatings.

The primary electron energy ranges from 0eV to 6keV and the current ranges from 0A to 5μA. No electron or hole transmission is measured ($I_2 < 1nA$).

- Single-crystal diamond:

We also measured a supposedly single-crystal diamond sample with the same dimensions as the above sample provided by the Apollo Company. The aluminum coating on the front side has a diameter of 4mm and a thickness of 30nm and the back side has a diameter of 4mm and a thickness of 50nm.

a) The transmitted hole current measurements (V1 is positive while V2 is grounded) are listed in Table 7.1.

Table 7.1: Primary electron gain of the polycrystalline diamond in the transmission mode

E_p (keV)	V1 (kV)	E_{eff} (keV)	I_p (μA)	F (MV/m)	Gain (I_2/I_p)
4	4	8	0.1	20	>200
4	4	8	0.5	20	~30
4	2	6	8.5	10	2~3

E_p is the primary electron energy, E_{eff} is the effective primary electron energy when striking the diamond sample, I_p is the primary current and F is the electric field across the diamond.

Figure 7.5 is the typical transmission current I_2 vs. time T curve of the measurements.

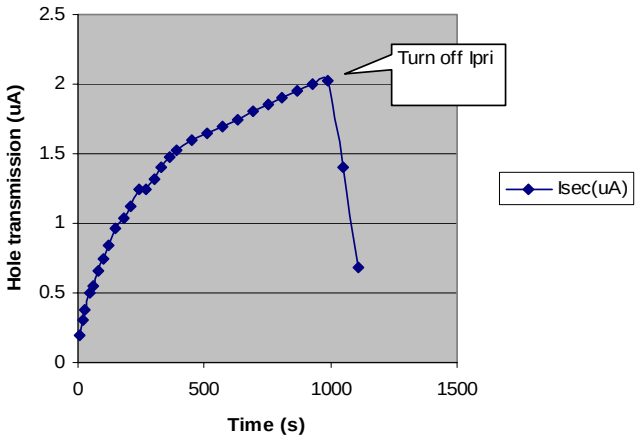

Figure 7.5 Typical transmitted hole current vs. time

The current gain increased with time (of the order of minutes) presumably due to temperature rise in the diamond. Fig. 7.6 shows the hole transmission current vs. sample holder temperature (indirect temperature of the sample).

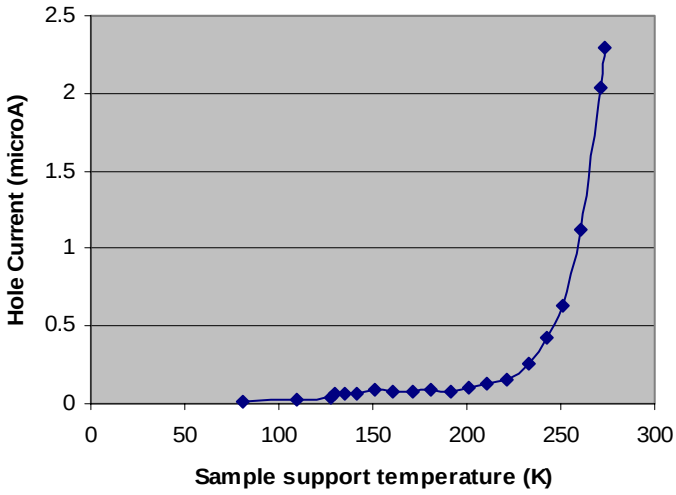

Figure 7.6 Transmitted hole current vs. sample holder temperature

At low temperature (80K) the gain is more than 3 orders of magnitude less than at high T (300K). The reason is presumably that the sample quality is not good enough, i.e., there are too many traps and grain boundaries in the sample.

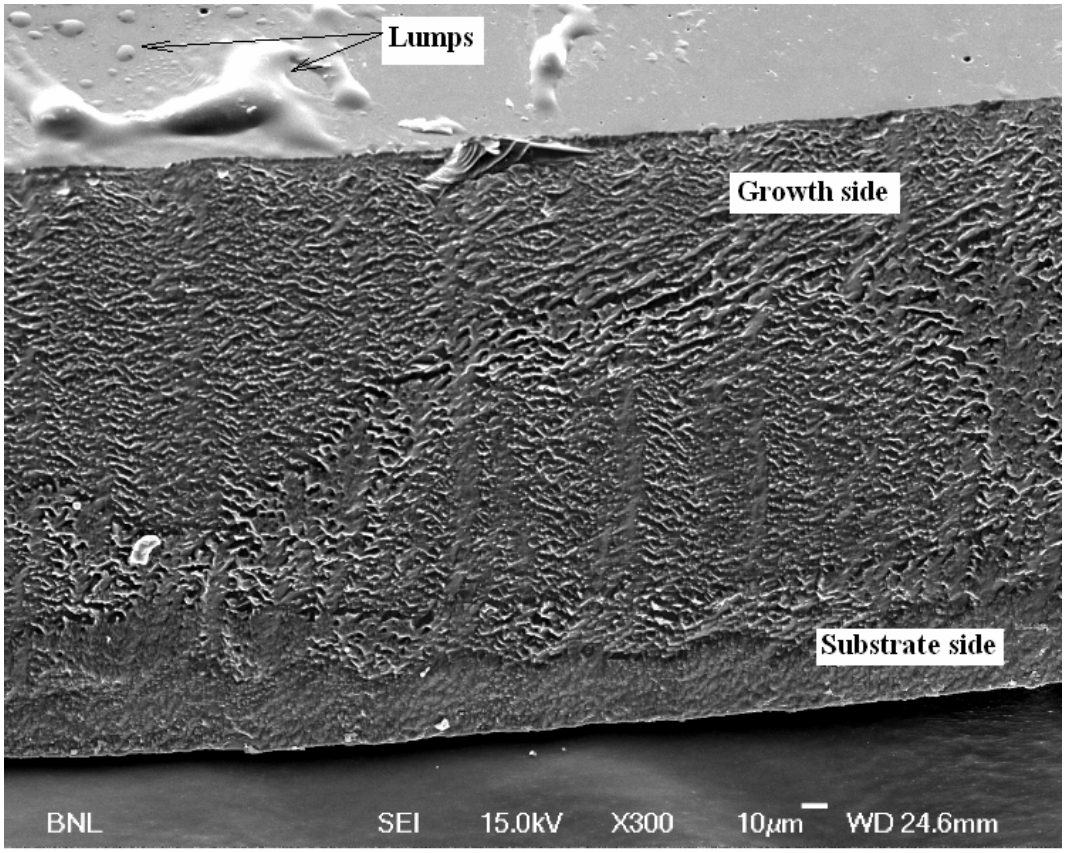

Figure 7.7 SEM picture of the cross-section of the single-crystalline sample

Fig.7.7 is the Scanning Electron Microscope (SEM) picture of the cross-section of the supposedly single-crystal sample. It's clear that the substrate side (bottom) is different from the growth side (top). It seems that the grain size is very small (<1μm) on the substrate side and even on the growth side the grain size is not very big. The small lumps on the surface (~ a few μm) may also indicate small grain size.

The long time equilibrium property of the curve in fig.7.5 may be explained by the temperature dependence of the trap release. It is expected that by using higher quality samples (higher purity and larger grain size) the trap concentration would be greatly reduced therefore the electron and hole transmission property would be greatly improved.

b) Transmitted electron measurements (V1 is +80V biased while V2 is more positive biased).

We got similar electron transmission gain (I_2/I_p~200) under the following conditions: Ep=4keV, V1=80V, Eeff≈4keV, Ip≈5nA and F=20MV/m.

- **Natural diamond**

The natural diamond was purchased from a Russian company. It has a rectangular shape, 3x2.64mm^2 and a thickness of 160 microns. The diamond is a type 2a with a modest nitrogen concentration of about 60 ppm ($1.3x10^{-19}$ /cm^3). No other contaminant atoms were reported although we suspect there may be other contaminants too. The diamond was checked with a microscope and was verified to be of good crystal quality. The diamond was coated on both faces with aluminum 30 nm thick.

Figure 7.8 shows the plots of electron transmission gain through the diamond for primary currents of 10nA, 20nA, 50nA and 100nA at room temperature and four primary energies: 1, 2, 3 and 4 keV. At low field gradient range (gradient<2MV/m), the gain increases as the gradient increases. This is due to the recombination of electron and hole at low gradient. The maximum gain decreases fast as we decreases the primary electron energy. At an electron energy of 1 keV the gain disappears because the low energy electrons are totally absorbed in the aluminum coating. One also notices that the high gain curves do not show the saturated gain property at high field gradient. The slope of the curve at high field gradient increases as the current through the diamond increases. This may possibly due to ionization of impurity atoms, leading to a larger SEY.

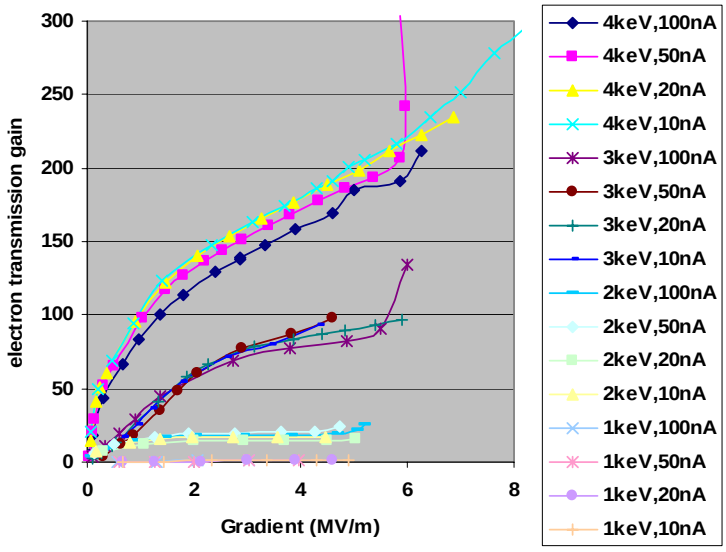

Figure 7.8 Electron transmission through the natural diamond for constant primary current of 20 nA at room temperature and primary energies of 1, 2, 3 and 4 keV

Fig.7.9 shows the plots of electron transmission gain for constant primary current of 100nA at a diamond temperature of 80K.

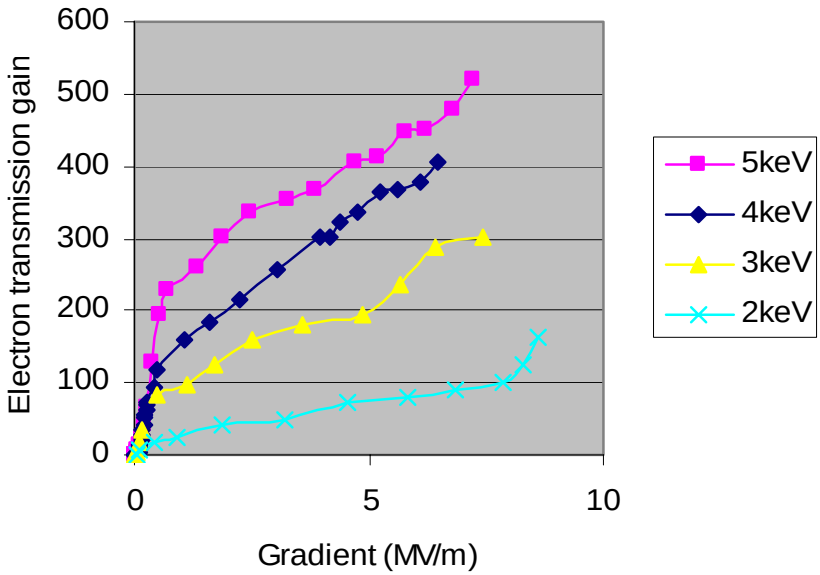

Figure 7.9 Electron transmission through the natural diamond for constant primary current of 100 nA at 80K and primary energies of 2, 3, 4 and 5 keV

First, even at low temperatures we still get very high gain. Second, one observes the clear knee points of each curve. They are plotted in fig.7.10. It appears that these points are the real gain induced by the primary electrons. The threshold point of the curve in fig.7.10 (~2keV) is caused by the primary electron energy loss in the Al coating. The slope of the curve is found out to be about 14eV per generation of electron-hole pair and is consistent to what reported.

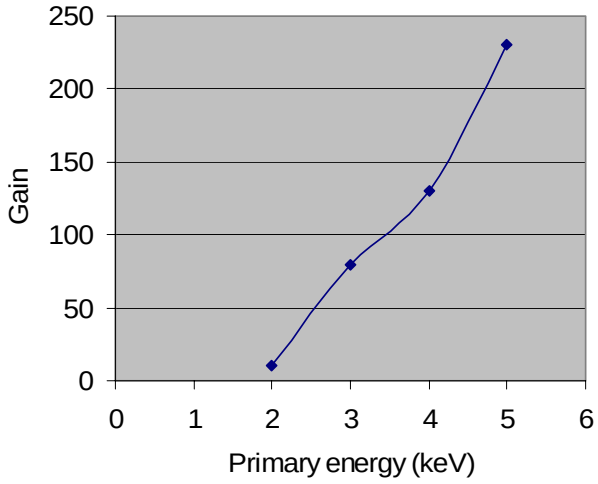

Figure 7.10 Gain of the knee points in fig.7.9 vs. primary electron energy

Similar to the room temperature case, at high current through the diamond, we observe a higher gain than expected just by SEY from the primary electrons. Presumable this is due to that there is extra current induced by the secondary electron when it drifts through the diamond. The main source of the extra current may come from the boron

impurity (the concentration is not reported) at low field gradient (<5MV/m). The reason is that the excitation energy level of carbon (5.5eV) and nitrogen impurity (~1.7eV) is too high to be excited.

We use a simple model to simulate the energy distribution of the drifting secondary electron. Assume the secondary electrons lose their total energy in any inelastic collision and gain energy again under the electric field. The probability P(E) that an electron is stopped by the inelastic collision in a distance ds is:

$$P(E) = ds / \lambda(E) \qquad (7.2.1)$$

where $\lambda(E)$ is the mean free path of the electron which is a function of the energy expressed in (6.10.3). E can also be expressed as:

$$E = G \times ds \qquad (7.2.2)$$

where G is the field gradient through the diamond. From (7.2.1) and (7.2.2) one can numerically find out the energy distribution of the electrons. Fig.7.11 shows the distributions of different field gradients.

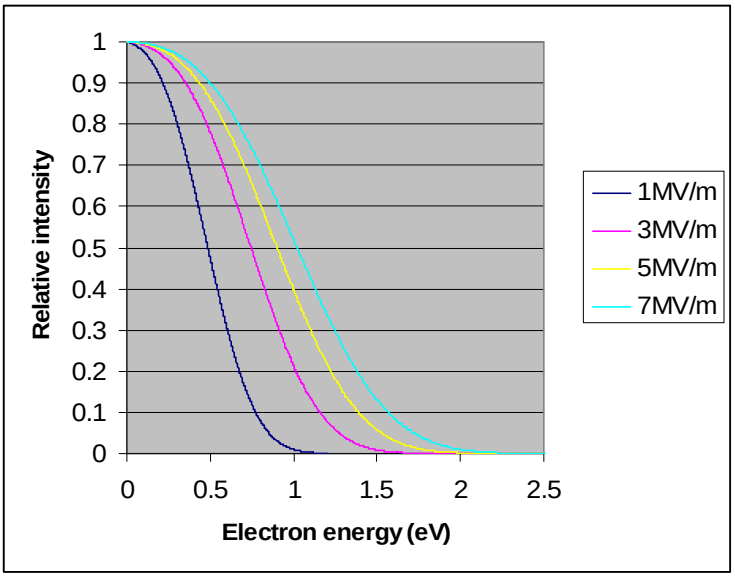

Figure 7.11 Energy distributions of the drifting secondary electron under field gradients of 1, 3, 5 and 7MV/m. Because of the high nitrogen concentration the Fermi level is close to the bottom of the conduction band. The above curves assume that the Fermi level is 0.1V below the bottom of the conduction band.

From the energy point of view it is obviously that unless the gradient is larger than 5MV/m the contributions of the nitrogen ionization and carbon ionization can be ignored. The boron has excitation energy of only 0.1~0.37eV. So, as the field gradient increases, more and more boron atoms are ionized and provide more and more extra current.

One also notices from fig.7.11 that when the gradient is larger than 5MV/m or so, the portion which the energy is higher than 1.7eV becomes noticeable. The sharp increase of the gain at gradient higher than 5MV/m may due to the ionization of the nitrogen.

One can give an estimation of the boron concentration from fig.7.9 under some assumptions. The extra current I_S at gradient of 5MV/m is about the same as the current generated by the primary electron, i.e., one secondary electron ionizes one boron atom. We don't have much information about the boron impurity cross-section. But according to reference [33] one may guess that the cross-section is roughly in the order of $\sigma_B \approx 10^{-13}\,\mathrm{cm}^2$. Therefore the charge density of the boron ionization n_{BI} is:

$$n_{BI} \approx 1/\sigma_B W \approx 10^{15}/\mathrm{cm}^3 \qquad (7.2.3)$$

where $W = 162\mu\mathrm{m}$ is the diamond sample thickness. Even that the boron concentration is as small as $10^{15}/\mathrm{cm}^3 \approx 10^{-2}\,\mathrm{ppm}$, it still can provide considerable extra current.

This boron ionization assumption may also explain the phenomenon that the gain is very sensitive to the sample's temperature. As the temperature increases, not only the

boron energy increases so that the energy needed for ionizing boron decreases, but also the effective boron cross-section may increase. This makes the temperature so sensitive.

There are many other possible impurities in the sample but most of them have high activation energy and their contributions are ignored.

The transmission through the natural diamond was sensitive to the primary beam position and spot size. This led to large variation of the electron transmission between sets of experiments as seen in the room temperature and low temperature measurements.

We also measured the hole transmission by changing the polarity of the field across the diamond. No hole transmission was measured. This is because the Nitrogen impurity is a deep trap for holes while a shallow trap for electron.

- **Pulsed mode NEA surface**

Another experiment was performed by Dr. Triveni Rao and Dr. John Smedley, using a Hydrogenated sample.

The transmission coefficient (emission current / primary current) is small. The low emission was determined to be caused by both the low transmission in diamond and insufficient NEA due to poor hydrogenation. Further studies based on better quality samples and improved hydrogenation are needed.

CHAPTER 8. SUMMARY AND CONCLUSIONS

We have investigated the emittance compensation of a compact RF gun with a solenoid, a drift and a linac system. We conclude that it is desired that the cathode is recessed and the solenoid is close to the cathode to approach the invariant envelope of the gun cavity. The drift space length and beam waist spot size are determined by (3.2.31). The linac field gradient is determined by (3.2.32). In principle the drift length, the solenoid strength, the waist spot size and the linac accelerating gradient can be found out by the beam spot size at the gun exit which is easy to get by simulation.

The effect of chromaticity generally starts at the solenoid and can be ignored in the gun. The energy spread makes the spread of the slice waist positions larger and therefore degrades the emittance compensation. A gun cavity should be designed to have minimum energy spread at gun exit. This can be achieved by making the effective cavity cell length short. The linac gradient required to minimize the chromaticity by the linac entrance focusing (equation 3.3.4) is larger than the gradient required matching the invariant envelope (equation 3.2.32). The applied solution must be a compromise between the two. For a beam with limited energy spread the waist needs to be in front of the linac entrance. A magnetized beam degrades the emittance ε_M compensation; the beam size must be comparable to σ_M (4.2.4) to have some ε_M compensation; matching the linac entrance chromaticity may dominate the emittance compensation for the low gun field case.

For the RHIC electron cooling project, the charge per bunch and the magnetization are very high. With the requirement of merging the low energy beam with the high

energy beam, it is found that the emittance ε_M is dominated by the chromaticity. By recessing the cathode, reducing the full cell length and enlarging the beam size, the energy spread is reduced. In addition, by employing the Z-bend system and 3rd harmonic cavities the transverse emittance ε_M is as small as 35mm.mr, while the longitudinal emittance is as small as 100deg.keV. These results fulfill the RHIC e-cooling requirements.

The mechanism, physical properties and the electron beam qualities of the secondary emission enhanced photoinjector are presented. The calculations show great promise of this kind of cathode. For a 700MHz RF gun with reasonable parameters such as aluminum coating thickness of a few hundred of nm and diamond thickness of about 15μm to 30μm, the cathode can easily handle 100W of heat power with its maximum temperature well below the criterion. The secondary electron beam quality is comparable to the traditional photocathode. The new approach has many advantages:

1. Reduction of the number of primary electrons by the large SEY, i.e. a very low laser power requirement in the photocathode producing the primaries.
2. Protection of the cathode from possible contamination from the gun, allowing the use of large quantum efficiency but sensitive cathodes.
3. Protection of the gun from possible contamination by the cathode, allowing the use of superconducting gun cavities.
4. Production of high average currents, up to ampere class.
5. Expected long lifetime.

In the experiment #1 we verified experimentally that the RF field penetration is poor even for a very thin metal film. This makes it important to have a thick aluminum film to carry the RF current induced power.

In experiment #2 we measured the charge carrier (electron or hole) transmission in diamond samples. The experiment shows that the transmission is strongly dependent on the sample quality: there is no transmission for the polycrystalline diamond sample which is assumed to have many defects, while for the better quality single-crystalline diamond we get amplification of the primary electron that is larger than 200. Nevertheless, the data and the SEM picture show that even the present so-called single-crystal diamond sample there are still many defects. The experiments of the natural diamond provide a lot of information and most of the data are consistent with theory and previous measurements. To have better transmission properties, a single crystal pure diamond is desired. Single crystal requirement seem more important. With better quality diamond, we expect that the electron transmission through diamond will be appropriate for SEEP.

In the future measurements we will measure the electron transmission of the better quality diamond, the electron emission of a hydrogen termination diamond, the pulsed mode and RF test.

REFERENCES:

[1] L. M. Young, "PARMELA," Los Alamos National Laboratory Report, LA-UR-96-1835 (Revised February 27, 2001).

[2] H. Poth, "Electron Cooling: Theory, Experiments, Application", CERN-EP/90-04

[3] G. I. Budker, Ya. S. Derbenev, N. S. Dikansky, V. I. Hudelainen, I. N. Meshkov, V. V. Parkhomchuk, D. V. Pestrikov, B. N. Sukhina, A. N. Skrinsky, IEEE Trans. Nucl. Sci. NS-22 (1975) 2093

[4] N. S. Dikansky, V. I. Kononov, V. I. Kudelainen, I. N. Meshkov, V. V. Parkhomchuk, D. V. Pestrikov, A. N. Skrinsky, B. N. Sukhina, Proceedings of the sixth ALL-Union Meeting on Acceleration of Charged Particles, Dubna, Nauka, Moscow, 1978

[5] V. V. Parkhomchuk, "New insights in the theory of electron cooling", Nucl. Instrum. Methods Phys. Res. A 441, 9-17 (2000)

[6] J. Rosenzweig, L. Serafini, "Transverse particle motion in radio-frequency linear accelerators", Physical Review E, V49, 1599

[7] J. D. Lawson, The Physics of Charged Particle Beams", 2nd ed. (Oxford University Press, New York, 1988).

[8] Luca Serafini, James B. Rosenzweig, "Envelope analysis of intense relativistic quasilaminar beams in rf photoinjectors: A theory of emittance compensation", Physical Review E, V55, 7565

[9] B. E. Carlsten, "New Photoelectric Injector Design for The Los Alamos National Laboratory XUV FEL Accelerator", Nucl. Instrum. Methods Phys. Res. A 285, 313 (1989)

[10] S. G. Anderson, J. B. Rosenzweig, "Nonequilibrium transverse motion and emittance growth in ultrarelativistic space-charge dominated beams", PRST-Accelerators and beams, V3, 094201 (2000)

[11] O. D. Kellogg, "Foundations of Potential Theory", P194, (1967)

[12] Kwang-Je Kim, "RF and Space-Charge Effects in Laser-Driven RF Electron Guns", Nucl. Instrum. Methods Phys. Res. A275, 201-218 (1989)

[13] X.Y. Chang, X.J. Wang, I. Ben-Zvi, "BNL Photo-injector performance optimization", Proceedings of the 2001 Particle Accelerator Conference, Chicago

[14] D.T. Palmer, X.J. Wang, et al., "Emittance studies of the BNL/SLAC/UCLA 1.6 cell photocathode RF gun", PAC'97 Proceedings, Vancouver, B.C., Canada

[15] K.Flöttmann, D, Janssen, V. Volkov, "Emittance compensation in a superconducting RF gun with a magnetic mode", PACS: 41.60.Cr; 41.75.Fr; 42.55.Xi; 82.25.-j

[16] Dmitry Kayran, Vladimir N. Litvinenko, "Novel Method of Emittance Preservation in ERL Merging System in Presence of Strong Space Charge Forces", PAC05 Proceedings, Knoxville, TN, USA

[17] http://www.ioffe.rssi.ru/SVA/NSM/Semicond/Diamond/index.html

[18] Mainwood A 1994 Properties and Growth of Diamond (Emis Data Reviews Ser. 9) ed G Davies (London: INSPEC) p 3

[19] Collins A T 1994 Properties and Growth of Diamond (Emis Data Reviews Ser. 9) ed G Davies (London: INSPEC) p 288

[20] J. E. Yater, A. Shih, and R. Abrams, "Electron transport and emission properties of C(100)", Physical Review B, V56, R4410

[21] J. van der Weide, Z. Zhang, et al., "Negative-electron-affinity effects on the diamond (100) surface", Physical Review B, V50, 5803

[22] J. B. Cui, R. Graupner, J. Ristein, L. Ley, Diamond Relat. Mater. 8 (1999) 748

[23] A. Ahih, J. Yater, P.Pehrsson, J. Butler, C. Hor, and R. Abrams, "Secondary electron emission from diamond surfaces", J. Appl. Phys. 82(4), 1860

[24] Minoru Niigaki, Toru Hirohata, et al., "Extremely High Quantum Photoyield from Cesiated Polycrystalline Diamond Films", Jpn. J. Appl. Phys. Vol. 37 (1998) pp. L1531-L1533

[25] Nebel C E and Stutzmann M 2001 Properties, Growth and Applications of Diamond (Emis Data Reviews Ser. 26) ed M H Nazare and A J Neves (London: INSPEC) p 40

[26] http://www.kobelco.co.jp/p047/products/np0802e/np08022e.htm

[27] National Institute of Standards and Technology, http://physics.nist.gov/PhysRefData/Star/Text /ESTAR.html

[28] A. Shih, J. Yater, P. Pehrsson, J. Butler, C. Hor, and R. Abrams, "Secondary electron emission from diamond surfaces, J. Appl. Phys., Vol. 82, No. 4, 15 August 1997

[29] Alexander Oh, "Particle Detection with CVD Diamond, Recent Developments and Applications", Seminar DESY Zeuthen 20.01.04, http://www-zeuthen.desy.de/~schoene/unter_texte/texte/DiamondsatHEP.pdf

[30] J. E. Yater and A. Shih, "Secondary electron emission characteristics of single-crystal and polycrystalline diamond", J. Appl. Phys., Vol. 87, No. 11, 8103, 1 June 2000

[31] E. Worner*, E. Pleuler, C. Wild, P. Koidl, “Thermal and optical properties of high purity CVD-diamond discs doped with boron and nitrogen”, Diamond and Related Materials 12 (2003) 744–748

[32] Brian D. Thorns, Pehr E. Pehrsson, and James E. Butler, “A vibrational study of the adsorption and desorption of hydrogen on polycrystalllne diamond”, J. Appl. Phys. 75 (3) 1804, 1 February 1994

[33] Mara Bruzzi, David Menichelli, and Silvio Sciortino, “Deep levels and trapping mechanisms in chemical vapor deposited diamond”, J. Appl. Phys., Vol. 91, #9, pp 5765-5774

[34] C E Nebel, “Electronic properties of CVD diamond”, Semicond. Sci. Technol. 18 No 3 (March 2003) S1-S11

[35] Jan Isberg, Johan Hammersberg, et al., “High Carrier Mobility in Single-Crystal Plasma-Deposited Diamond”, Science, Vol. 297 (6 Sep. 2002), pp 1670-1672

[36] Brian D. Thorns, Pehr E. Pehrsson, and James E. Butler, “A vibrational study of the adsorption and desorption of hydrogen on polycrystalllne diamond”, J. Appl. Phys. 75 (3) 1804, 1 February 1994

[37] V. Parkhomchuk, I. Ben-Zvi, “Electron Cooling for RHIC”, C-A/AP/47, April 2001,

[38] Vladimir N. Litvinenko, I. Ben-Zvi, et al., “HIGH CURRENT ENERGY RECOVERY LINAC AT BNL”, Proceedings of the 2004 FEL Conference, 570-573

[39] CHUAN-JONG TUNG, “CSDA Ranges of Electrons in Metals”, CIIINESE JOURNAL OF PHYSICS, VOL. 17, NO. 1, SPRING 1979

[40] National Institute of Standards and Technology, http://physics.nist.gov/PhysRefData/Star/Text /ESTAR.html

[41] M. P. Seah and W. A. Dench, Surf. Interface Anal. 1, pg10 (1979)

[42] S. Liao "Light transmittance and microwave attenuation of a gold-film coating on a plastic substrate", IEEE MTT-23, p.846, 1975

[43] D. T. Morelli et al., "Thermal conductivity of synthetic diamond films", J. Appl. Phys. 64 (6), pp 3063-3066 (1988)